Frontières libres

Paul Vigneaux

École Normale Supérieure de Lyon

Habilitation à diriger des recherches

Discipline : Section CNU 26
Mathématiques appliquées et applications des mathématiques

FRONTIÈRES LIBRES

Contributions à des problèmes viscoplastiques et d'estimation de paramètres.

PAUL VIGNEAUX

Rapporteurs :

Christophe Ancey	Professeur, EPFL, Suisse
Alfredo Bermúdez de Castro	Professeur, Université de Santiago de Compostela, Espagne
Jean-Paul Vila	Professeur, Institut de Mathématiques de Toulouse & INSA

Soutenance publique le 22 juin 2017, devant le jury composé de :

Christophe Ancey	Professeur, EPFL, Suisse
Alfredo Bermúdez de Castro	Professeur, Université de Santiago de Compostela, Espagne
François Bouchut	Directeur de Recherche CNRS, Université Paris-Est
Emmanuel Grenier	Professeur, ENS de Lyon & INRIA
Laure Saint-Raymond	Professeur, ENS de Lyon
Jean-Paul Vila	Professeur, Institut de Mathématiques de Toulouse & INSA

FRONTIÈRES LIBRES

PAUL VIGNEAUX

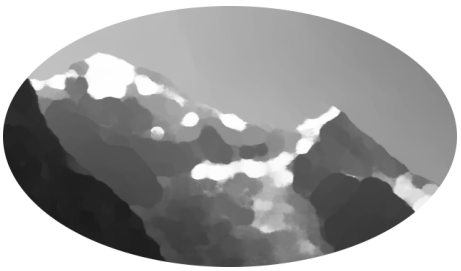

Contributions à des problèmes viscoplastiques et d'estimation de paramètres.
Manuscrit présenté en vue d'une Habilitation à Diriger des Recherches (HDR)

Printemps 2017

COLOPHON

Paul Vigneaux: *Frontières libres,* Contributions à des problèmes viscoplastiques et d'estimation de paramètres. Manuscrit présenté en vue d'une Habilitation à Diriger des Recherches (HDR), © Printemps 2017

This document was typeset using the `classicthesis` LaTeXpackage developed by A. Miede.

Compiled September 25, 2019.

REMERCIEMENTS

J'exprime ma profonde reconnaissance à Christophe Ancey, Alfredo Bermúdez de Castro et Jean-Paul Vila pour avoir consacré un temps précieux à rapporter sur ce mémoire ainsi que pour leurs suggestions de suites à ces travaux. Je suis aussi très reconnaissant à François Bouchut et Laure Saint-Raymond d'avoir accepté de faire partie du jury de cette habilitation.

Les travaux de recherche de la période concernée sont issus de collaborations avec de nombreux collègues qui m'ont beaucoup appris, je les remercie chaleureusement. Didier Bresch est le premier à avoir guidé mes pas dans la région et je lui exprime toute ma gratitude pour les échanges que nous avons toujours eus et ses précieux conseils. Je mesure tous les jours l'immense chance que nous avons à travailler à l'UMPA. Au plus près, je suis extrêmement reconnaissant à Vincent Calvez, Emmanuel Grenier et Denis Serre pour le soutien sans faille qu'ils ont apporté sur tout le spectre des activités que recouvre l'équipe EDP au sein du laboratoire et du département. Ces remerciements s'étendent évidemment à l'ensemble de l'Unité, collègues et amis, dont l'appétit mathématique et les qualités humaines sont exceptionnels. Je n'oublie pas non plus les échanges riches et constants que nous avons avec les membres de l'ICJ depuis toutes ces années (séminaires, MathαLyon, etc): je m'excuse de ne point les citer tou.te.s ici tant la liste serait longue.
Un autre évènement heureux fut la rencontre et le travail au long cours que nous avons accompli avec les collègues d'Andalousie, tout particulièrement Enrique Fernández-Nieto et Gladys Narbona-Reina. Je pense ne pas avoir les mots pour traduire complètement ici toute l'admiration que j'ai pour eux et ce que j'ai appris là-bas sur les mathématiques et sur bien d'autres sujets.
Concernant la partie modélisation en Biologie et Médecine, je remercie par ordre chronologique Julien Olivier et Hossein Khonsari, Violaine Louvet, François Ducray, Marc Lavielle, Céline Helbert et Adeline Samson pour les travaux réalisés ensemble. J'espère que nous pourrons continuer ces intéractions dans le futur.

L'aventure de six ans au sein d'*Images des Mathématiques* a été un épisode marquant et un formidable moyen de découvrir la communauté. Bien sûr, j'ai pu bénéficier de – et été conquis par, comme toute personne ayant eu la chance de pouvoir l'écouter – la sapience et les talents de conteur d'Etienne Ghys au quotidien. Mais, j'ai aussi souvent été touché et appris énormément de choses sur le monde math-

ématique grâce aux incalculables échanges épistolaires ou viva voce avec les membres du comité de rédaction et les auteurs. Je m'excuse une nouvelle fois de ne pas tou.te.s les mentionner tant ils sont nombreux.

Dans la *vraie vie*, nous avons la fortune d'être épaulés par des personnes de grande valeur. Je souhaite remercier ici : Magalie, Virginia, Sandy et Catherine pour l'ENS ; Sylvie et son équipe de choc pour INRIA. Les collègues proches connaissent mon penchant prononcé pour les références bibliographiques antédiluviennes, parfois exotiques : malgré la numérisation, ces quêtes peuvent être ardues et elles n'aboutissent souvent que grâce au talent des documentalistes. Je profite de l'occasion pour remercier plus particulièrement Chantal Bon Saint Côme et Cyril Mauvillain de la Bibliothèque de Recherche Mathématiques et Informatique de Bordeaux puis Gilles Lastra de Natias de la Bibliothèque de l'ENS de Lyon. Je ne saurais oublier non plus toute l'équipe du PSMN pour son support HPC au mésocentre hébergé dans nos murs. Dernière salve mais non des moindres, je rends aussi grâces aux acteurs du réseau Mathrice qui est un formidable outil pour la communauté mathématique française et dont l'importance va croissant.

J'aimerais finir en exprimant ma profonde gratitude pour l'accueil extraordinaire que m'ont réservé les familles bretonnes de Lyon et andalouses de Séville. Elles se reconnaîtront !

Lyon, Juin 2017

CONTENTS

LIST OF FIGURES

ACRONYMS

AL Augmented Lagrangian

BM Bermúdez-Moreno

MRI Magnetic resonance imaging

SWB Shallow Water Bingham

1 INTRODUCTION

In this document, I give an overview of some research activities performed since my PhD in 2007, where I focused on the numerical analysis and simulation of bifluid flows (via Level Set methods) and applications to microfluidics. Present memoir covers the period 2007 - 2017 corresponding to the arrival in the Rhône-Alpes region, first in Chambéry for one year, under the guidance of Didier Bresch who notably initiate me to viscoplastic materials. Then at UMPA in Lyon and particularly in the INRIA NUMED team headed by Emmanuel Grenier.
As we shall see, presented works are essentially different from what was done during the PhD, however it appears that (unintentionally) a common link is the presence of moving interfaces (and interactions with other fields; that was intentional), leading to the title of this document.

The presentation is divided into two parts: the first one deals with numerical analysis and simulation for *viscoplastic materials* while the second part is concerned by blending PDEs and Statistics for parameters estimation in *medicine*.

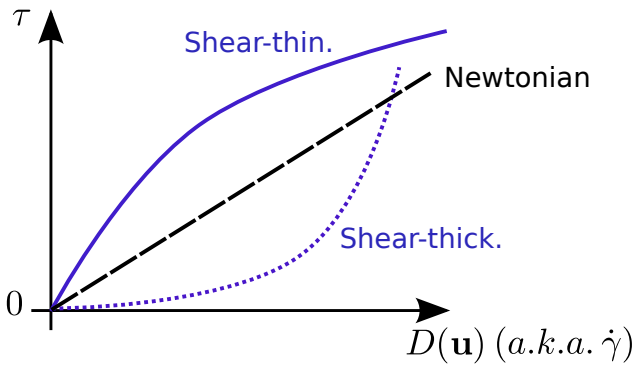

Figure 1.1: Various constitutive (power) laws, in 1D: Newtonian (dashed black line), shear thinning (blue curve) and shear thickening (dotted blue curve). In Rheology, one denotes usually $D(\mathbf{u})$ as $\dot{\gamma}$.

Viscoplastic materials can be either fluid or rigid depending on the exerted stress. As such, they can not be described by a Newtonian constitutive law like the Navier-Stokes equations. In this latter case, the (deviatoric) stress tensor τ is linked to the rate of strain $D(\mathbf{u})$ linearly as

$$\tau = 2\eta D(\mathbf{u}) \tag{1.1}$$

where η is the viscosity. For complex (non-Newtonian) fluids studied in Rheology, the constitutive law is nonlinear. This nonlinearity can take on the most varied forms: for shear thinning (paint) or shear thickening (wet sand) materials, the "viscosity" depends on $D(\mathbf{u})$ itself, leading to so called "power laws" (see below for a more precise definition of the power). To fix the ideas, we represent some of these "generalized" Newtonian laws in Figure 1.1, in the 1D framework. For some materials where the past history of the flow needs to be taken into account, the stress tensor τ can not be expressed via a simple explicit relation like (1.1) but there is an evolution PDE to link τ and $D(\mathbf{u})$. This is typically the case for viscoelastic materials (like honey). We refer the reader to [Osw09] for a longer overview on Rheology.
For viscoplastic materials, the nonlinearity comes from the fact that the rigid or fluid behaviour is associated to a so called yield stress (τ_y) under which $D(\mathbf{u}) = 0$ and τ is undefined. The simplest viscoplastic law is named after E. C. Bingham and reads:

$$\tau = 2\eta D(\mathbf{u}) + \tau_y \frac{D(\mathbf{u})}{|D(\mathbf{u})|} \Leftrightarrow D(\mathbf{u}) \neq 0, \tag{1.2}$$

$$|\tau| \leqslant \tau_y \Leftrightarrow D(\mathbf{u}) = 0, \tag{1.3}$$

which is represented in Figure 1.2. One can generalize Bingham by combining with the power non-linearity leading to another very well - known (and used) relation, the Herschel-Bulkley law ($\wp > 0$):

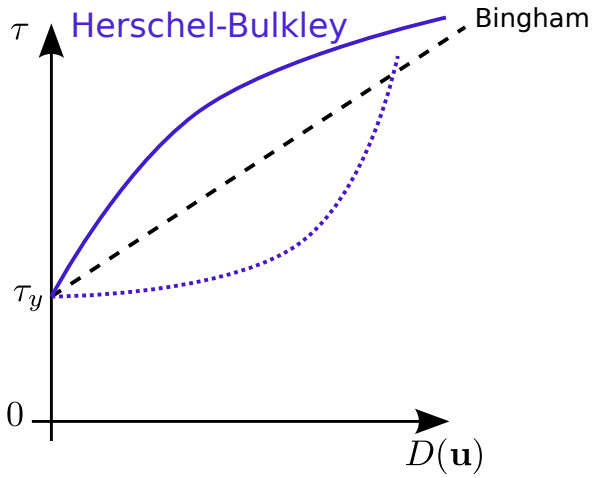

Figure 1.2: Various viscoplastic laws, in 1D. Bingham (dashed black line). Herschel-Bulkley: shear thinning ($0 < \wp < 1$, blue curve) and shear thickening ($\wp > 1$, dotted blue curve).

$$\tau = \nu \frac{D(\mathbf{u})}{|D(\mathbf{u})|^{1-\wp}} + \tau_y \frac{D(\mathbf{u})}{|D(\mathbf{u})|} \Leftrightarrow D(\mathbf{u}) \neq 0, \tag{1.4}$$

$$|\tau| \leqslant \tau_y \Leftrightarrow D(\mathbf{u}) = 0, \tag{1.5}$$

where ν is the "plastic viscosity" which is usually expressed in terms of the "consistency".

In the past years, I worked on various aspects of the numerical analysis and the simulation of viscoplastic flows. Both on tensorial form of (1.2)-(1.3) (or (1.4)-(1.5)) or on reduced integrated versions of these formulations. The reason for the latter is that we wanted to simulate this kind of rheology in a shallow water context for geophysical applications (we thus need to reduce computation times by using 2D equations instead of 3D ones). For the full versions, we perform extremely refined 2D parallel simulations with Augmented Lagrangian methods in "complex" geometries, like cross geometries which lead to non-trivial "plug" zones (where $D(\mathbf{u}) = 0$). These simulations compare very well with physical experiments of Guillaume Chambon and colleagues (IRSTEA). This was done in collaboration with Arthur Marly which I am advising in 2015-2018.

For integrated versions of the equations, it is a long term research

Figure 1.3: A feature wanted for numerical schemes: new material arrives from the top left but the deposit at the very bottom (near the red zones and arrows) is stationary. This is possible due to viscoplastic behaviour. From here around 0:40.

cycle which comes to an end in this memoir. These works where initiated with D. Bresch and Enrique D. Fernandez-Nieto while we were all three in Chambéry. We then continued the numerical analysis aspects with Andalusian colleagues G. Narbona-Reina and J.M. Gallardo. To be very concrete, we refer the reader to the following movie (2 minutes; you can cut the sound of your device while watching...). This is a typical example of a dense snow avalanche (by opposition to powder snow avalanche) and it appears that viscoplastic models can be useful in this case[1]. Of course, *we are very far from being able to build models and simulate precisely such avalanches*. However, as mathematicians, we were happy to design 2D finite volumes numerical schemes which are able to capture accurately one of the striking features of

1 For powder snow avalanches, completely different models were used, e. g. more like bifluid (mixture) Navier-Stokes à la Kazhikhov–Smagulov [KS77], see [EHS05; DAB11].

this movie, for a prototype of such viscoplastic flows: namely the fact that there exists a stationary shape of the free surface which is absolutely not trivial compared to the Newtonian case (flat surface). This is highlighted in Figure 1.3.

The 2D results for this problem are original and presented in Chapter 3 of this manuscript. They were submitted in March 2017. They close one cycle but open another which will be more centered on the comparison with physical experiments.

The second part focuses on the work done in the INRIA NUMED (for Numerical Medicine) team in collaboration with Emmanuel Grenier and Violaine Louvet. We work jointly with Medical Doctors (essentially in the Lyon area) to develop mathematical models and test them against real available clinical data. To do so, we focus on PDEs (in view of being able to capture temporal but also spatial effects when this is mandatory) and Bayesian methods, due to the fact that we have essentially data for a whole group of individuals (it is very rare that a study focuses only on one patient). Of course blending PDEs and Bayesian methods – to estimate the parameters of the models, given the observed data – leads to very expensive computational costs. Consequently, as many other colleagues in the field, we work on the modification of current methods to decrease these costs. This leads us to collaborate with experts in Statistics like Marc Lavielle and Adeline Samson (for SAEM methods) or in Kriging like Céline Helbert.

Publications covering the period of the HDR are given on page 5. Articles not described in this manuscript are: [Kho+13; FV14].

For ease of browsing, please find the direct links (mostly on HAL) of the updated postprints of the published articles described more in depth in the present manuscript:

Viscoplastic fluids:

- [Bre+10]: Shallow water Bingham (SWB), initial HAL link
- [Aca+12]: Shallow water Herschel-Bulkley HAL link
- [FGV14]: SWB with wet/dry fronts in 1D HAL link
- [MV17]: Classic Bingham in 2D: expansion-contraction HAL link

PDEs and Statistics:

- [GLV14]: SAEM with Off-line Metamodel (fixed) HAL link
- [Gre+18]: Evolving Metamodel inside the SAEM HAL link

[Aca+12] C. Acary-Robert, E.D. Fernández-Nieto, G. Narbona-Reina, and P. Vigneaux. "A Well-balanced Finite Volume-Augmented Lagrangian Method for an Integrated Herschel-Bulkley Model." In: *Journal of Scientific Computing* 53.3 (2012), pp. 608–641 (cit. on pp. 4, 14, 21, 22, 25).

[Bre+10] D. Bresch, E. D. Fernandez-Nieto, I. R. Ionescu, and P. Vigneaux. "Augmented Lagrangian Method and Compressible Visco-plastic Flows: Applications to Shallow Dense Avalanches." In: *New Directions in Mathematical Fluid Mechanics*. Ed. by G. P. Galdi et al. Advances in Mathematical Fluid Mechanics. Birkhauser Basel, 2010, pp. 57–89. ISBN: 978-3-0346-0152-8 (cit. on pp. 4, 11, 14, 15, 20, 21, 32).

[FGV14] Enrique D. Fernández-Nieto, José M. Gallardo, and Paul Vigneaux. "Efficient numerical schemes for viscoplastic avalanches. Part 1: The 1D case." In: *Journal of Computational Physics* 264 (May 2014), pp. 55–90 (cit. on pp. 4, 21–23, 29, 31, 32, 36, 38, 39, 41–43, 48–50, 66).

[FV14] Enrique D. Fernandez-Nieto and Paul Vigneaux. "Some Remarks on Avalanches Modelling: An Introduction to Shallow Flows Models." In: *Advances in Numerical Simulation in Physics and Engineering - Lecture Notes of the XV 'Jacques-Louis Lions' Spanish-French School*. Ed. by Carlos Parés, Carlos Vazquez Cendon, and Frederic Coquel. SEMA SIMAI Springer Series. June 2014, pp. 51–106 (cit. on p. 4).

[Gre+18] E. Grenier, C. Helbert, V. Louvet, A. Samson, and P. Vigneaux. "Population parametrization of costly black box models using iterations between SAEM algorithm and kriging." In: *Computational and Applied Mathematics* 37.1 (2018). Accepted March, 24, 2016, pp. 161–173. DOI: 10.1007/s40314-016-0337-5 (cit. on pp. 4, 99, 100, 102, 112).

[GLV14] Emmanuel Grenier, Violaine Louvet, and Paul Vigneaux. "Parameter estimation in non-linear mixed effects models with SAEM algorithm: extension from ODE to PDE." In: *ESAIM: Mathematical Modelling and Numerical Analysis* 48.5 (July 2014), pp. 1303–1329 (cit. on pp. 4, 99–102, 106, 108).

[Kho+13] Roman H. Khonsari et al. "A mathematical model for mechanotransduction at the early steps of suture formation." In: *Proceedings of the Royal Society of London. Series B* 280.1759 (May 2013), p. 20122670 (cit. on p. 4).

[MV17] Arthur Marly and Paul Vigneaux. "Augmented Lagrangian simulations study of yield-stress fluid flows in expansion-contraction and comparisons with physical experiments." In: *Journal of Non-Newtonian Fluid Mechanics* 239 (Jan. 2017), pp. 35–52 (cit. on pp. 4, 83, 84, 88, 89).

Part I

VISCOPLASTIC FLOWS

Variational inequalities. Duality methods: augmented Lagrangian and Bermúdez-Moreno, Well - Balanced Finite Volumes: wet/dry fronts and avalanche stationnary states on DEM topography. Rheologies: Bingham and Herschel-Bulkley

2

ON SOME ASPECTS OF YIELD STRESS FLUIDS

2.1 MODELS

We deal here with materials which have the ability to be either in a rigid or a deforming state, depending on the stress which is acting on them. In "daily life", the more common experience of such materials is perhaps the toothpaste or the *mayonnaise*: if one does not squeeze sufficiently the tube, these pastes will not flow out. Of course this dual solid/liquid behaviour is actually encountered in many other situations: industrial flows such as oil extraction and transport, food processing, civil engineering; geophysical flows such as landslides, debris flows or dense snow avalanches, etc. The study of such materials, which names evolved progressively through time (from *Bingham plastic* or *Bingham solid* to *Yield stress fluid* via *Viscoplastic fluid* or *Bingham fluid*; see [Cou16]), has a long history.

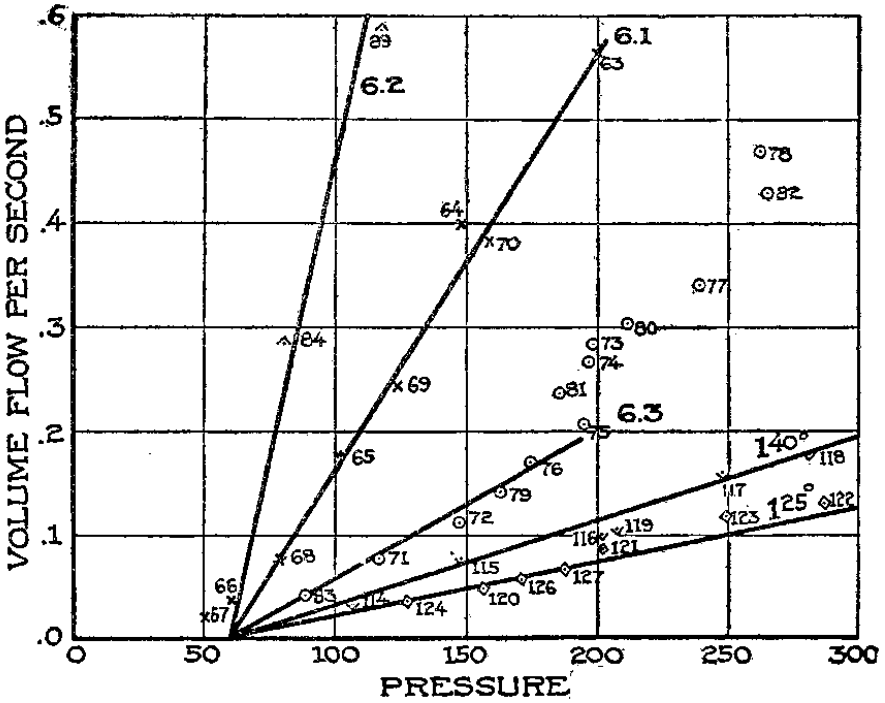

Figure 2.1: From the 1916 Bingham's article. Flow rate as a function of the pressure for a clay suspension in various capillaries (see [Bin16]).

To the best of our knowledge, early works introducing the notion of *rigidity of liquids* together with the ability to flow at an increasing speed as the stress increases are due to Schwedoff in 1889-1900

[Sch89; Sch90; Schoo]. In an apparently independent study, Bingham also published in 1916 a scalar constitutive law (see Fig. 2.1) involving this rigid/fluid behaviour [Bin16; Bin22]. Actually, Bingham's law is a degenerate version of the equation of state proposed by Schwedoff. It should be noted that in [Bin16], Bingham not only formalised a phenomenological observation of yield stress fluids but also proposed theories for several physical aspects of these flows, which are still relevant and at the heart of current researches in physics and rheology: we refer again to [Cou16] for a detailed review.

Dimensional form of the equations

In modern terms (and tensor form which can be traced back to Hohenemser and Prager [HP32], see also Oldroyd [Old47]), the Bingham law relates the deviatoric part of the stress tensor $\boldsymbol{\tau}$ and the rate of deformation tensor $D(\mathbf{u})$ as

$$\boldsymbol{\tau} = 2\eta D(\mathbf{u}) + \tau_y \frac{D(\mathbf{u})}{|D(\mathbf{u})|} \Leftrightarrow D(\mathbf{u}) \neq 0, \tag{2.1}$$

$$|\boldsymbol{\tau}| \leqslant \tau_y \Leftrightarrow D(\mathbf{u}) = 0, \tag{2.2}$$

where η is the kinematic viscosity and τ_y is the so called *yield stress*. Note that if $\tau_y = 0$, the Bingham law degenerates to the classical Stokes equation ($\boldsymbol{\tau} = 2\eta D(\mathbf{u})$) for *Newtonian* fluids. Norms of tensors will be defined in the following but the mathematical interest of (2.1)-(2.2) lies in the non-linearity of the threshold τ_y: the deviatoric stress is multivalued when $D(\mathbf{u}) = 0$. A way to handle such a law is to reformulate it as a variational inequality as we will soon see.

Let us remark that there are various viscoplastic constitutive laws: Casson model and the Herschel-Bulkley law, among others (see [BDY83] for a very complete review and historical references). The latter being one of the favorite laws when it comes to take into account shear-thinning or shear-thickening effects (*power law* effects). It has been successful in many practical rheological tests [Cou16].

Our starting point is the full incompressible Navier-Stokes-Bingham equations posed in a 3D domain, which can be evolving in time, meaning that we want to take into account moving free surfaces. Note that this will be useful for ease of presentation but we have also made some extensions to the Herschel-Bulkley case (as it will be mentioned later).

In dimensional variables, we thus consider the following 3D equations, posed in a domain $\mathcal{D}(t)$:

$$\rho\left(\partial_t \mathbf{u} + (\mathbf{u}.\nabla)\mathbf{u}\right) - \operatorname{div} \boldsymbol{\tau} + \nabla p = \rho f, \tag{2.3}$$

$$\operatorname{div} \mathbf{u} = 0, \tag{2.4}$$

where ρ is the density, $\mathbf{u}$, the velocity, p, the pressure, $\mathbf{f}$ is the body force density and $\boldsymbol{\tau}$ is defined by (2.1)-(2.2). The norm of a tensor $\boldsymbol{\sigma} = \left(\sigma_{i,j}\right)_{i,j}$ is defined as

$$|\boldsymbol{\sigma}|^2 := \sum_{i,j=1}^{3} \sigma_{i,j}^2. \tag{2.5}$$

We introduce the notations for the normal and tangential decomposition of velocity and stress: we denote by $\mathbf{n}$ the outward unit normal to $\mathcal{D}(t)$ and

$$\mathbf{u} := u_n \mathbf{n} + \mathbf{u}_t \text{ where } u_n := \mathbf{u} \cdot \mathbf{n}, \tag{2.6}$$

$$\boldsymbol{\tau}\mathbf{n} := \tau_n \mathbf{n} + \boldsymbol{\tau}_t \text{ where } \tau_n := \boldsymbol{\tau}\mathbf{n} \cdot \mathbf{n}. \tag{2.7}$$

We assume that some (lower) parts of $\mathcal{D}(t)$, say $\Gamma_b(t)$, are bounded by a given solid bottom on which non-penetration and friction with a coefficient α (Navier boundary condition) occur, i. e.

$$\boldsymbol{\tau}_t = -\alpha \mathbf{u}_t \text{ and } \mathbf{u} \cdot \mathbf{n} = 0 \text{ on } \Gamma_b(t). \tag{2.8}$$

The (unknown upper) free surface of $\mathcal{D}(t)$ is denoted $\Gamma_s(t)$ and is subject to a no-stress condition:

$$\boldsymbol{\tau}\mathbf{n} = 0 \text{ on } \Gamma_s(t). \tag{2.9}$$

We thus assume that $\partial\mathcal{D}(t) = \Gamma_b(t) \cup \Gamma_s(t)$ and that the material is advected by the flow, i. e.

$$\partial_t 1_{\mathcal{D}(t)} + \mathbf{u} \cdot \nabla 1_{\mathcal{D}(t)} = 0, \tag{2.10}$$

where $1_{\mathcal{D}(t)}$ is the characteristic function of the domain $\mathcal{D}(t)$.
The problem is finally closed by imposing some initial conditions on $\mathcal{D}$, $\mathbf{u}$ and ρ.

Before going on, let us recall the dimensionless form of the above problem. Several scalings are possible but let us follow our approach from [Bre+10]. Let L_c and V_c be the characteristic length and velocity, respectively. The characteristic time is then deduced from $T_c = L_c/V_c$. We denote dimensionless variables with tildes:

$$(x, y, z) = L_c(\tilde{x}, \tilde{y}, \tilde{z}) \text{ and } \mathbf{u} = V_c \tilde{\mathbf{u}}. \tag{2.11}$$

In the same way, we define the following characteristic variables for the density (ρ_c), yield stress ($\tau_{y,c}$), viscosity (η_c), body force (f_c), friction coefficient (a_c), pressure ($p_c = \rho_c L_c f_c$), deviatoric stress ($\tau_c = \rho_c V_c^2$). We obtain the following *dimensionless equations* (dropping the tildes for simplicity):

$$\rho\left(\partial_t \mathbf{u} + (\mathbf{u}.\nabla)\mathbf{u}\right) - \operatorname{div} \boldsymbol{\tau} + \frac{1}{Fr^2}\nabla p = \frac{1}{Fr^2}\rho f, \tag{2.12}$$

$$\boldsymbol{\tau} = \frac{2}{Re}\eta D(\mathbf{u}) + B\tau_y \frac{D(\mathbf{u})}{|D(\mathbf{u})|} \Leftrightarrow D(\mathbf{u}) \neq 0, \tag{2.13}$$

$$|\boldsymbol{\tau}| \leqslant B\tau_y \Leftrightarrow D(\mathbf{u}) = 0, \tag{2.14}$$

$$\boldsymbol{\tau}_t = -A\alpha \mathbf{u}_t \tag{2.15}$$

where the dimensionless numbers are

$$Re = \frac{\rho_c V_c L_c}{\eta_c}, \quad Fr^2 = \frac{V_c^2}{L_c f_c}, \quad B = \frac{\tau_{y,c}}{\rho_c V_c^2}, \quad A = \frac{a_c}{\rho_c V_c}. \tag{2.16}$$

The two first are the famous Reynolds and Froude numbers. The classical Bingham number is

$$Bi = \frac{\tau_c L_c}{\eta_c V_c}, \quad \text{so that} \quad B = \frac{Bi}{Re}. \tag{2.17}$$

Note that we do not rewrite here the other equations from (2.3)-(2.10) which remain unchanged in dimensionless variables.

2.2 VARIATIONAL INEQUALITIES

In the series of works presented for this HDR, we adopt the "variational inequality way" to tackle the threshold of viscoplastic constitutive laws.
When it comes to solve the Bingham law there is a wide variety of methods but one can roughly aggregate them into two types: variational approaches and regularization methods. In a sort of paradox, the former where developed well before (1950-1980) the latter (1980) but remained quite unused before 2000. Several facts may be responsible for this situation: (i) Variational resolution was seemingly more difficult to implement than regularization counterparts (where standard Navier-Stokes codes can be straightforwardly adapted to plug the Bingham law). Consequently, in terms of real applications, variational approaches did not quite enter the engineering fields (ii) There was a strong debate between Rheologists, during the '80 and the '90, on the physical relevance of the Bingham law itself, arguing that the threshold does not occur and that the constitutive law needs to be regularized from the start (which was used as an additional argument to implement regularized codes). This debate is now essentially behind and the threshold concept has proved to be relevant in many physical situations (see the very recent review [Cou16] by P. Coussot, one of the renown experts in the field). The mathematical question is then how can we solve as accurately as possible models like the Bingham law ? What is nowadays clear is that when it comes to capture numerically the interface between rigid ($|D(\mathbf{u})| = 0$) and fluid zones ($|D(\mathbf{u})| \neq 0$), regularization methods should not be used since they may lead to wrong yield surfaces (see [FN05] for a review). An illustration of such inconsistency is given by Burgos et al. [BAE99] where a simulated yield surface has the inverse convexity of the true expected analytic yield surface. On the other hand for such tasks, variational approaches, in particular linked with duality methods, are now mature and have proved to be as the most accurate (cf. another very

recent review [SW17]).
The history of variational yield stress fluids can be traced back to the works of Il'iushin [Ili40], Prager [Pra52], Mosolov and Miasnikov [MM65] and Duvaut and Lions [DL76]. Efficient numerical techniques where designed following the works of Glowinski, Lions and Trémolières [GLT76] and coworkers, including the so called Augmented Lagrangian (AL) methods which are used in the present corpus (we also compare with another duality method due to Bermúdez and Moreno [BM81]). We refer to the article [SW17] and the book [GW11] for numerous applications of such methods in the simulation of viscoplastic flows.

Following Duvaut and Lions [DL76], using the space

$$\mathcal{V}(t) = \left\{ \boldsymbol{\Phi} \in H^1(\mathcal{D}(t))^3 \ / \ \boldsymbol{\Phi} \cdot \mathbf{n} = 0 \ \text{ on } \ \Gamma_b(t) \right\}, \tag{2.18}$$

(2.4), (2.12)-(2.15) can be reformulated as the following variational inequality: $\forall t \in (0,T)$, find $\mathbf{u}(t,\cdot) \in \mathcal{V}(t)$, $p(t,\cdot) \in L^2(\mathcal{D}(t))$ s.t.

$$\begin{aligned}
&\forall \boldsymbol{\Phi} \in \mathcal{V}(t),\ \forall q \in L^2(\mathcal{D}(t)),\\
&\int_{\mathcal{D}(t)} \rho\left(\partial_t \mathbf{u} + (\mathbf{u}\cdot\nabla)\mathbf{u}\right)\cdot(\boldsymbol{\Phi}-\mathbf{u}) + \int_{\mathcal{D}(t)} \frac{2}{Re}\eta D(\mathbf{u}) : (D(\boldsymbol{\Phi}) - D(\mathbf{u}))\\
&- \int_{\mathcal{D}(t)} \frac{1}{Fr^2} p(\operatorname{div}\boldsymbol{\Phi} - \operatorname{div}\mathbf{u}) + \int_{\mathcal{D}(t)} B\tau_y\left(|D(\boldsymbol{\Phi})| - |D(\mathbf{u})|\right)\\
&+ \int_{\Gamma_b(t)} A\alpha\,\mathbf{u}_t\cdot(\boldsymbol{\Phi}_t - \mathbf{u}_t) \geqslant \frac{1}{Fr^2}\int_{\mathcal{D}(t)} \rho\mathbf{f}\cdot(\boldsymbol{\Phi}-\mathbf{u}), \qquad (2.19)\\
&\int_{\mathcal{D}(t)} q \operatorname{div}\mathbf{u} = 0. \qquad (2.20)
\end{aligned}$$

Let us emphasize that even the resolution of the 2D stationary Stokes-Bingham degenerating from (2.1)-(2.4) has still interesting open problems related to the study of the localization of the rigid and fluid zones. In particular, the transitions between them, which are called the *pseudo-plugs* zones (in the sense of e. g. [PFM09]), is worth of interest in the case of "complex" geometries (like cross pipes) which highlight the richness of the tensorial Bingham law. This will be the subject of a subsequent chapter which is linked to the PhD thesis of Arthur Marly who I am advising since September 2015.

See page 83

Of course, the numerical resolution of the above Navier-Stokes-Bingham equations with free-surface can be implemented with cutting-edge methods. A quite "direct" strategy would be to decouple the computation of the velocity and the motion of the domain. For both tasks, one can implement his/her favorite numerical methods. This is a work of its own and not trivial at all, see e. g. [Nik+11]. However, the resulting computation times for such a 3D free surface problem with a *non-Newtonian* constitutive law is prohibitive in practice. Simulations can be done but they take so long to complete that they

Reminding that one must solve a modified (Navier-) Stokes problem where typically, instead of having only one linear system (LS) per time step, several additional LS are needed to "fix-point the rheology".

are not doable for many applications. This is the case in geophysics where $\mathcal{D}(t)$ can be very large and long physical times need to be computed to study the stopping dynamics of the material (depending on the value of τ_y). Reduced models are thus highly needed.

As a consequence, many efforts where devoted to the derivation of shallow water equations for Bingham flows (and more generally for non-Newtonian flows), when one can assume that the vertical height of the flow is much smaller than its horizontal length. In the next section, we recall our approach from [Bre+10] where variational inequalities are used.

2.3 A FORMAL SHALLOW-WATER-BINGHAM ASYMPTOTICS

The field concerned with the derivation of asymptotic models for thin films of non-Newtonian materials is extremely active. One can distinguish two families of approaches: lubrication theories and shallow water models. *In the former*, fluid velocity and pressure are expressed with the local fluid height and its derivatives. The model is thus centered on one evolution PDE for the local fluid height. Initially, lubrication models were derived for small slopes and thin flows. They can however be extended for steep slopes, see e. g. Balmforth *et al.* [Bal+06]. *When the flows are thicker*, shallow water models are considered: a system of two evolution PDEs is obtained by averaging the mass and momentum conservation equations across the stream depth. The model is then expressed in terms of the local fluid height and the local *depth-averaged velocity*. For recent developments and reviews on this subject, in the context of non-Newtonian fluids, we refer the reader to the articles [Anc07; BW04; Luc+09; FNV10; NV13; BMV16; BB16] and references therein.

The works presented in this memoir are based on a prototypical shallow water Bingham model obtained *via* the variational framework and assuming a special form of the test functions. This idea was introduced in our paper [Bre+10] and was used subsequently to some extensions in our work [Aca+12] (extension to the Herschel-Bulkley law) and in Ionescu *et al.* [Ion13; IL16] (together with limit load analysis), among others. We note that this model remains modest with respect to a fine physical description, since it assumes in particular that the velocity profile is constant along the vertical direction (i. e. in the direction of averaging). However, from the mathematical viewpoint, it has the interest of being an integrated model with a full variational inequality feature keeping trace of the structure, though (naturally) modified by averaging, close to the associated standard 2D Bingham equations. This means that we keep the mathematical richness of the

2D tensorial Bingham law which can still be useful in 2D shallow water viscoplastic applications. Note in addition that this model degenerates also smoothly to other known viscous shallow water models when $\tau_y = 0$, as we will see in the following.

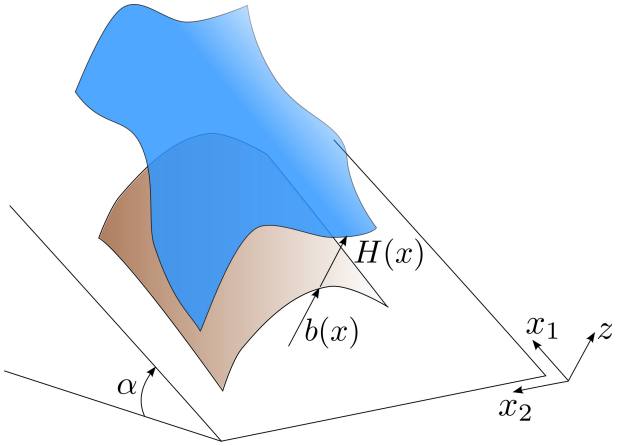

Figure 2.2: Domain in 2D.

We now introduce this typical model. We refer to [Bre+10] for the full derivation. Let $\Omega \subset \mathbb{R}^2$ be a given domain for the space variable x. The $\mathbb{R}^2$ plane generated by Ω is supposed to be sloping at an angle α from the horizontal plane (see Fig. 2.2). We denote by $z \in \mathbb{R}$ the variable in the orthogonal direction to Ω. The general bottom which bounds the fluid by below is defined by $b(x), x \in \Omega$. The fluid domain $\mathcal{D}(t)$ is then defined as

$$\mathcal{D}(t) = \{(x, z) \in \Omega \times \mathbb{R} \,/\, b(x) < z < b(x) + H(t, x)\}, \tag{2.21}$$

where H is the time-dependent height of the fluid. As usual for shallow water type models, we denote by $V = V(t, x) \in \mathbb{R}^2$ the vector of the average of the velocity (orthogonal to the z-axis) along the depth of the fluid (i.e. from $z = b(x)$ to $z = b(x) + H(t, x)$).

We assume a shallow water asymptotics where $1 \gg \varepsilon$ is the ratio between a characteristic height of the fluid and a characteristic horizontal length (typically $\sqrt{|\Omega|}$). We further assume

$$Re = B = Fr = \mathcal{O}(1), \qquad \varepsilon \ll 1. \tag{2.22}$$

In brief, the relations (2.10)-(2.19)-(2.20) are rewritten in terms of H, averaged in the z direction and an asymptotic expansion in terms of ε is performed. The key point in this formal derivation is that we choose test functions consistent with the derived (averaged) horizontal velocity, namely 3D test functions for the velocity of the type (decomposing in horizontal and vertical components) $\mathbf{\Phi} = (\Psi, \theta), \quad \Psi \in$

$\mathbb{R}^2, \theta \in \mathbb{R}$, independent on z and such that $\theta = -z\,\mathrm{div}_x\Psi$. When the density is constant (let us assume now $\rho = 1$ for simplicity), we obtain (at order ε^0) the following 2D Shallow Water Bingham model (going back to dimensional variables): find $H \in L^2([0,T], L^\infty(\Omega))$, $V \in L^2([0,T]; \mathcal{V}(t))$ with $\partial_t V \in L^2([0,T]; L^2(\Omega)^2)$, such that

$$\partial_t H + \mathrm{div}_x(HV) = 0, \tag{2.23}$$

$$\begin{aligned}
&\forall \Psi \in \mathcal{V}(t), \quad \int_\Omega H\Big(\partial_t V + (V\cdot\nabla_x)V\Big)\cdot(\Psi - V)dx + \int_\Omega aV\cdot(\Psi - V)dx \\
&+ \int_\Omega 2\eta H D(V) : D(\Psi - V)dx + \int_\Omega 2\eta H \mathrm{div}_x V(\mathrm{div}_x\Psi - \mathrm{div}_x V)dx \\
&+ \int_\Omega \tau_y H\Big(\sqrt{|D(\Psi)|^2 + (\mathrm{div}_x\Psi)^2} - \sqrt{|D(V)|^2 + (\mathrm{div}_x V)^2}\Big)dx \\
&\geqslant \int_\Omega H(f_\Omega + f_z\,\nabla_x b)\cdot(\Psi - V)dx - \int_\Omega \frac{H^2}{2} f_z(\mathrm{div}_x\Psi - \mathrm{div}_x V)dx
\end{aligned} \tag{2.24}$$

We redefine $\mathcal{V}(t)$ for the sequel of this chapter.

where

$$\mathcal{V}(t) = \big\{\Psi \in H^1(\Omega(t))^2 \;/\; \Psi = 0 \text{ on } \partial\Omega(t)\big\} := H_0^1(\Omega)^2, \tag{2.25}$$

$$\nabla_x U := \left(\frac{\partial U_i}{\partial x_j}\right)_{i,j}, \quad i = 1,2,\ j = 1,2, \tag{2.26}$$

$$\mathrm{div}_x U := \frac{\partial U_1}{\partial x_1} + \frac{\partial U_2}{\partial x_2}, \tag{2.27}$$

$$D(U) := \frac{\big[\nabla_x U + (\nabla_x U)^t\big]}{2}, \forall\, U(t,\cdot) := (U_1, U_2) \in \mathcal{V}(t) \tag{2.28}$$

and the body force $\mathbf{f} = (f_\Omega, f_z) \in \mathbb{R}^2 \times \mathbb{R}$ in the $\Omega \times z$ frame of reference, is assumed to be constant (typically taken as the gravity).

In the aforementioned asymptotic expansion, the slope is supposed to be small ($\alpha \ll 1$) and the norm of the gradient of $b(x)$ is small ($|\nabla_x b| \ll 1$). But it is worth noting that this model is also valid for a slope $\alpha = 0$ (horizontal bottom), which is not generally the case for other models proposed in the literature (see for example [Bal+00], [FNV10]). Another interesting feature of the model is that in the case of a plane horizontal slope ($\alpha = 0$) and with a vanishing yield stress ($\tau_y = 0$), we recover a viscous shallow water system which has the same structure as the one derived by Gerbeau and Perthame in [GP01] (note that the hypothesis of friction at the bottom, instead of a no-slip condition is a key point in this degeneracy to [GP01]). The *shallow water* formulation (2.24) is in weak form. It can be rewritten in the strong form to have the expression of the associated (*integrated*) Bingham constitutive law. Namely, the corresponding formulation is

$$H\left(\partial_t V + (V\cdot\nabla_x)V\right) + aV - \mathrm{div}_x\sigma = H(f_\Omega + f_z\,\nabla_x b) - \nabla_x\left(\frac{H^2}{2} f_z\right), \tag{2.29}$$

I being the identity matrix in 2D.

where

$$\begin{cases} \sigma = 2\eta\,(D(V) + \mathrm{tr}(D(V))I) + \tau_y \dfrac{D(V) + \mathrm{tr}(D(V))I}{\sqrt{|D(V)|^2 + |\mathrm{div}_x V|^2}} & \text{if } |D(V)| \neq 0 \\ |\sigma| \leqslant \tau_y & \text{if } |D(V)| = 0, \end{cases} \tag{2.30}$$

the second invariant $|\sigma|$ of a tensor σ being defined here as

$$|\sigma|^2 := \sum_{i,j=1}^{2} \sigma_{ij}^2. \tag{2.31}$$

Note that in the following, the body force will be the influence of gravity, denoted by g. To write this force, we must decide what is the orientation of the plane generated by Ω; by convention we will say that if (x_1, x_2, z) is the frame of reference (cf. Figure 2.2), then the tilted axis (with respect to the horizontal) is x_1, i.e.

$$f_\Omega = (-g \sin\alpha\,,\, 0), \quad f_z = -g\cos\alpha. \tag{2.32}$$

Model (2.23)-(2.24) originated a program of research – part of this HDR – concerned with the numerical resolution of such formulations, *blending well-balanced finite volumes and duality methods*. The 1D framework is the object of the next section, while the 2D extension is described in the next chapter.

2.4 NUMERICAL SCHEMES AND A FOCUS ON THE 1D FRAMEWORK

In the context of well-balanced finite volume discretization, we will see that the construction of the scheme for (2.23)-(2.24) involves specific features associated to the viscoplastic threshold. Let us detail this point.

First, for the discretization in time, we consider a first order forward Euler scheme since we focus here on the difficulties associated with the space discretization. We get from (2.23)-(2.24): superscripts n are for the evaluation at time $t = t^n = n\Delta t$

$$\frac{H^{n+1} - H^n}{\Delta t} + \mathrm{div}_x(H^n V^n) = 0, \tag{2.33}$$

and $\forall \Psi$,

$$\begin{aligned}
&\int_\Omega H^n\left(\frac{V^{n+1}-V^n}{\Delta t}+(V^n\cdot\nabla_x)V^n\right)\cdot(\Psi-V^{n+1})dx\\
&+\int_\Omega \alpha V^{n+1}\cdot(\Psi-V^{n+1})dx+\int_\Omega 2\eta H^n D(V^{n+1}):D(\Psi-V^{n+1})dx\\
&+\int_\Omega 2\eta H^n \mathrm{div}_x V^{n+1}(\mathrm{div}_x\Psi-\mathrm{div}_x V^{n+1})dx\\
&+\int_\Omega \tau_y H^n\left(\sqrt{|D(\Psi)|^2+(\mathrm{div}_x\Psi)^2}-\sqrt{|D(V^{n+1})|^2+(\mathrm{div}_x V^{n+1})^2}\right)dx\\
&\geqslant \int_\Omega H^n(f_\Omega+f_z\nabla_x b)\cdot(\Psi-V^{n+1})dx-\int_\Omega\frac{(H^n)^2}{2}f_z(\mathrm{div}_x\Psi-\mathrm{div}_x V^{n+1})dx. \quad (2.34)
\end{aligned}$$

We will see why "somehow" is needed here.

Doing so, we see that problems on the height and on the velocity are (somehow) decoupled. At each time step, supposing that we know (H^n, V^n), we need to solve both problems for (H^{n+1}, V^{n+1}). In the following, we thus concentrate first on the resolution of the variational inequality (2.34).

To solve for V^{n+1}, in the beginning of our works, we actually directly follow the ideas of Glowinski, Lions and Trémolières [GLT76], and coworkers on augmented Lagrangian methods, see also [FG83; GW11].
Let us begin by considering the 1D case in space and the description of the augmented Lagrangian method. The 1D version of (2.34) reads ($\Omega = [0, L] \subset \mathbb{R}$):

$$\begin{aligned}
&\int_0^L H^n\left(\frac{V^{n+1}-V^n}{\Delta t}+\frac{1}{2}\partial_x((V^n)^2)\right)(\Psi-V^{n+1})dx\\
&+\int_0^L \alpha V^{n+1}(\Psi-V^{n+1})dx+\int_0^L \tau_y\sqrt{2}H^n\left(|\partial_x\Psi|-|\partial_x V^{n+1}|\right)dx\\
&+\int_0^L 4\eta H^n\partial_x(V^{n+1})\partial_x(\Psi-V^{n+1})dx\geqslant\int_0^L H^n\left(f_\Omega+f_z\,\partial_x b\right)(\Psi-V^{n+1})dx\\
&-\int_0^L\frac{(H^n)^2}{2}f_z(\partial_x\Psi-\partial_x V^{n+1})dx,\quad\forall\Psi. \quad (2.35)
\end{aligned}$$

The variational inequality is equivalent to the minimization problem:

$$\mathcal{J}^n(V^{n+1}) \quad = \quad \min_{V\in\mathcal{V}}\mathcal{J}^n(V), \quad (2.36)$$

where $\mathcal{J}^n(V) = F^n(B(V)) + G^n(V)$, with $\mathcal{V} = H^1_0([0, L])$, $\mathcal{H} = L^2([0, L])$,

$$B:\mathcal{V}\to\mathcal{H},\ B(V)=\partial_x V,\qquad F^n:\mathcal{H}\to\mathbb{R},\ F^n(\lambda)=\int_0^L\tau_y\sqrt{2}H^n|\lambda|dx,$$

and $G^n : \mathcal{V} \to \mathbb{R}$,

$$\begin{aligned}
G^n(V) \quad = \quad &\int_0^L H^n\left(\frac{V^2/2-V^nV}{\Delta t}+\frac{1}{2}\partial_x((V^n)^2)V\right)dx+\int_0^L\alpha\frac{V^2}{2}dx\\
&+\int_0^L 4\eta H^n\frac{1}{2}(\partial_x V)^2dx-\int_0^L(f_\Omega+f_z\,\partial_x b)\,H^nV+\int_0^L f_z\frac{(H^n)^2}{2}\partial_x V dx.
\end{aligned}$$

As $\mathcal{J}^n(V)$ is a non-differentiable function, we consider the Lagrangian

$$\mathcal{L}^n : \mathcal{V} \times \mathcal{H} \times \mathcal{H} \to \mathbb{R},$$

$$\mathcal{L}^n(V, q, \mu) = F^n(q) + G^n(V) + \int_0^L H^n \mu(B(V) - q)dx,$$

and the Augmented Lagrangian function, for a given positive value $r \in \mathbb{R}$:

$$\mathcal{L}_r^n(V, q, \mu) = \mathcal{L}^n(V, q, \mu) + \frac{r}{2}\int_0^L H^n(B(V) - q)^2 dx. \tag{2.37}$$

Then, we search for the saddle point of $\mathcal{L}_r^n(V, q, \mu)$ over $\mathcal{V} \times \mathcal{H} \times \mathcal{H}$. Indeed, if we denote by (V^*, q^*, μ^*) this saddle point, then V^* is the solution of the minimization problem (2.36) (*cf.* [FG83]). To do so, we consider the algorithm proposed in [FG83], based on Uzawa's algorithm, to approximate the saddle point of (2.37).

Augmented Lagrangian algorithm

- **Initialization**: Suppose that V^n, H^n and μ^n are known. For $k = 0$, we set $V^k = V^n$ and $\mu^k = \mu^n$. Initialize r.
- **Iterate**:
  - Find $q^{k+1} \in \mathcal{H}$ solution of

    $$\mathcal{L}_r^n(V^k, q^{k+1}, \mu^k) \leqslant \mathcal{L}_r^n(V^k, \underline{q}, \mu^k), \quad \forall \underline{q} \in \mathcal{H}.$$

    In other words, $q^{k+1} \in \mathcal{H}$ is the solution of following minimization problem:

    $$\min_{\underline{q} \in \mathcal{H}} \left(\frac{H^n r}{2} \underline{q}^2 + H^n \tau_y \sqrt{2}\, |\underline{q}| - H^n(\mu^k + rB(V^k))\underline{q} \right). \tag{2.38}$$

    The solution of this problem is (denoting the sign function as "sgn"):

$$q^{k+1} = \begin{cases} 0 & \text{if } |\mu^k + rB(V^k)| < \tau_y, \\ \frac{1}{r}\left((\mu^k + rB(V^k)) - \tau_y \sqrt{2}\, \operatorname{sgn}(\mu^k + rB(V^k)) \right) & \text{otherwise.} \end{cases} \tag{2.39}$$

  - Find $V^{k+1} \in \mathcal{V}$ solution of

    $$\mathcal{L}_r^n(V^{k+1}, q^{k+1}, \mu^k) \leqslant \mathcal{L}_r^n(V, q^{k+1}, \mu^k), \quad \forall V \in \mathcal{V}.$$

    Thus, V^{k+1} is the solution of a minimization problem, which can be characterized by differentiating $\mathcal{L}_r^n(V, q, \mu)$ with respect to V. From (2.37), we deduce that V^{k+1} is the solution of the following linear problem (whose resolution is detailed later in this chapter):

pages 23-26

$$H^n\left(\frac{V^{k+1}-V^n}{\Delta t}\right)+\alpha V^{k+1}-\partial_x\left(4\eta H^n\partial_x(V^{k+1})\right)$$
$$-\partial_x\left(rH^n\partial_x(V^{k+1})\right)=(f_\Omega+f_z\,\partial_x b)\,H^n$$
$$+\partial_x\left(f_z\frac{(H^n)^2}{2}\right)-\frac{H^n}{2}\partial_x((V^n)^2)+\partial_x(H^n(\mu^k-rq^{k+1})). \tag{2.40}$$

- Update the Lagrange multiplier via

$$\mu^{k+1}=\mu^k+r(\partial_x V^{k+1}-q^{k+1}). \tag{2.41}$$

- Check convergence (see below) and update: $V^k=V^{k+1}$, $\mu^k=\mu^{k+1}$, $k\mapsto k+1$ and go to the next iteration...

- ... **until** convergence is reached:

$$\frac{\|\mu^{k+1}-\mu^k\|}{\|\mu^k\|}\leqslant \text{tol}. \tag{2.42}$$

At convergence, we get the value of V^{n+1} by setting $V^{n+1}=V^{k+1}$ (let's say $\text{tol}=10^{-5}$). It is shown in [FG83] that this algorithm converges to the saddle point of (2.37).

Of note, we did not describe the discretization in space yet. As we said previously, we want to adopt a finite volume approach. Consequently, it is worth realizing that the underlying global problem coupling (2.33) and (2.35) involves the following system (we use a slight change of notation which will be useful in the following: H^{n+1} is denoted as H^{k+1}; in spite of this choice, note again that H^{k+1} is not involved in the Augmented Lagrangian algorithm and, so, does not change in this loop):

$$(P)^{n,k}\begin{cases}\frac{H^{k+1}-H^n}{\Delta t}+\partial_x(H^nV^n)=0,\\[2ex] H^n\left(\frac{V^{k+1}-V^n}{\Delta t}\right)+\alpha V^{k+1}-\partial_x\left(4\eta H^n\partial_x(V^{k+1})\right)-\partial_x\left(rH^n\partial_x(V^{k+1})\right)\\ =(f_\Omega+f_z\,\partial_x b)\,H^n+\partial_x\left(\frac{(H^n)^2f_z}{2}\right)-\frac{H^n}{2}\partial_x((V^n)^2)+\partial_x(H^n(\mu^k-rq^{k+1})).\end{cases} \tag{2.43}$$

As a consequence, even if there is a decoupling of both problems in terms of the time discretization and the Augmented Lagrangian algorithm, it appears that to obtain a global well-balanced scheme, *there must be a coupling* between the mass and momentum equations *induced by the source terms* (involving topography *and the Lagrange multiplier*). Indeed, we showed in [Bre+10] that if the well-balancing is done taking into account only the traditional source terms (topography) but not the duality terms, then the computed solutions do not reach the stationary state, i. e. the fluid does not rigidify even if it

For shallow water type systems with source terms, this has been extensively studied in the literature, see e. g. [BV94; Bou04] and references therein.

should. Evidently, such schemes can not be used in the context of viscoplastic flows where one wants to compute the *arrested* state of the free surface. This leads us to the development of specific schemes (described a bit later in the text) for such problems.

After these descriptions, we can now draw more clearly the *global picture of our contributions* in this field:

- on the one hand, we need to design well-balanced schemes which take into account supplementary terms associated to the duality method;
- on the other hand, we can work on the duality method itself or adopting variants to study ways of optimizing the number of iterations (for the aforementioned augmented Lagrangian, it is related to the choice of r, see below) in the duality loop and save computation time: this was the motivation to also study the Bermúdez-Moreno methods;
- these developments were done progressively on generalizations of the initial Bingham model [Bre+10]: going from
  - Bingham to Herschel-Bulkley [Aca+12],
  - plane (inclined) slope to general topography [FGV14],
  - full wet domains to the presence of moving wet/dry fronts [FGV14],
  - 1D to 2D in space, as described in Chapter 3.

In the following of this chapter, we give a synthesis of the remaining published results, namely in 1D. As such we will not give all the precise notations and definitions and refer to the corresponding articles for all the details.

In [Aca+12], we consider the extension to *power* viscoplastic laws, which means that (2.1)-(2.2) is transformed into the Herschel-Bulkley law

$$\boldsymbol{\tau} = \nu \frac{D(\mathbf{u})}{|D(\mathbf{u})|^{1-\wp}} + \tau_y \frac{D(\mathbf{u})}{|D(\mathbf{u})|} \Leftrightarrow D(\mathbf{u}) \neq 0, \tag{2.44}$$

$$|\boldsymbol{\tau}| \leqslant \tau_y \Leftrightarrow D(\mathbf{u}) = 0, \tag{2.45}$$

Note that for ease of presentation the "viscous" coefficient ν is voluntarily unprecise.

where $\wp$ is the power of the law (if $\wp = 1$, we recover the Bingham law while if $\wp \in [0, 1]$ (resp. $\wp > 1$) the fluid is shear-thinning (resp. shear-thickening)). In Rheology, the "viscous" coefficient ν is usually expressed in terms of the so called consistency. Since this kind of law adds evidently a supplementary non-linearity in the problem, we need to adapt what was done in [Bre+10]. The article [Aca+12] presents the derivation of the corresponding Shallow Herschel-Bulkley

model and a modified augmented Lagrangian method to approximate solutions. In brief, we obtain an algorithm very close to page 19, where the power non-linearity is treated within the problem on q. Instead of being explicit in q^{k+1}, (2.39) becomes:

$$\left(2^{\frac{\wp+3}{2}}\nu|q^{k+1}|^{\wp-1}+r\right)q^{k+1}=(\mu^k+rB(V^k))\left(1-\frac{\tau_y\sqrt{2}}{|\mu^k+rB(V^k)|}\right)_+. \tag{2.46}$$

The subscript "+" in the last term stands for the positive part ($\lambda_+ := \max(0,\lambda)$). This non-linear problem on q^{k+1} is solved numerically with a fixed point-like method.
In addition, we design specific numerical tests to cover the different rheological regimes exhibited by the Herschel-Bulkley law (which are not contained in the Bingham model), namely regimes at "low or high shear rate" ($D(u)$) where a fluid with power $\wp_1$ is "more or less viscous" than a fluid of power $(1>)\wp_2>\wp_1$. This allows to show the ability of the numerical method to capture the rheological richness of Herschel-Bulkley. We refer to [Aca+12] for details.
Of note it is in this article that we also introduce the notion of numerical cost of the coupled well-balanced finite volume / duality method in terms of the viscosity matrix of the numerical flux approximation. We will describe this in a moment (page 25).

Our work moves several steps forward in [FGV14].
Concerning the duality method, we made a detailed study of the numerical cost. Recall that it is well known that in AL methods, the optimal values of the parameters are not easy to determine in the general case (see for instance [Del+06; CG16] for some particular cases). These parameters ((r,ρ)[1] in Glowinski's nomenclature) influence the speed of convergence of the iterative process towards the saddle-point, solution of the problem. As a consequence, a study of some sort of optimality for such parameters is of real interest when it comes to improve the computational efficiency. This is where the study of the Bermúdez-Moreno (BM) method [BM81] enters the scene. This method, which is built upon some properties of the Yosida regularization of maximal monotone operators, has been used for a wide range of applications (see [GPC05] and the references therein). In order to apply the method, the Yosida regularization of the subdifferential associated to the non-differentiable operator appearing in the formulation of the considered model needs to be determined. As for the AL, the performance of the algorithm strongly depends on the choice of two constant parameters. Fortunately, several ways to overcome this problem have been proposed in [PMC01; PCM02; GPC05]. In [FGV14], we adapt the guidelines of [PCM02] and determine, in

1 r has the same meaning as in the current manuscript where we put actually $\rho = r$

a theoretical way, an optimal choice of parameters in the sense that they provide the highest rate of convergence for the BM algorithm. For the AL, we perform some numerical studies of the optimal choice of parameters and we then compare both methods on various problems to give insight on their respective behaviours. To our best knowledge this was the first time that BM was applied to such kind of models and that such a systematic comparative study of the behaviour of the number of iterations in duality methods was done for several very different viscoplastic flows. It should also be noted that we made a careful study of the convergence of dual multipliers for which we derive analytic expressions allowing to study the order of convergence with respect to the space discretization. For sake of conciseness, we do not present here the derivation of the BM method* but it should be noted that the obtained algorithm – though via different means – has a structure which is very close to the one of the AL and it is equally easy to implement.

*but its global form is given on page 27 and its derivation is given in the 2D case in Chapter 3

The other important point of [FGV14] is that both for the AL and BM methods which are embodied in a common general framework, we design a well-balanced scheme which takes into account wet/dry fronts on general bottoms, for such viscoplastic free surface flows. Again, this was the first time that dry area treatment was proposed for flows with plastic behaviour. This is crucial when it comes to study real applications where there are always a flow with wet/dry front and a rigorous treatment is needed to compare qualitatively numerical simulations and physical experiments. In addition, we also design a specific *extension of the computation of the optimal duality parameter of the BM method in the case of wet/dry fronts* which is shown to be very efficient in practice.
In 1D, one of the conclusions of [FGV14] is that we designed schemes for shallow water Bingham avalanches where the BM method is nearly as fast and accurate as the AL (and nicely, the higher τ_y, the faster, which are actually the cases with more computation difficulties in terms of viscoplasticity), while giving an automatic a priori estimation of the optimal dual parameters.

The next five pages enter a bit more into the schemes' details.

To be complete, we now need to outline the details of *well-balancing design* of these schemes. The space domain $[0, L]$ is divided in computing cells $I_i = [x_{i-1/2}, x_{i+1/2}]$. For simplicity, we suppose that these cells have a constant size Δx. Let us define $x_{i+\frac{1}{2}} = (i + 1/2)\Delta x$ and $x_i = i\Delta x$, the center of the cell I_i. We define W^{k+1} (thanks to the aforementioned cosmetic harmonization of the notation) as the following vector of the unknowns,

$$W^{k+1}(x) = \left[H^{k+1}(x), V^{k+1}(x)\right].$$

For both AL and BM, we have a two equations problem like $(P)^{n,k}$ (2.43) which can be rewritten under the common system form:

$$D(W^n)\left(\frac{W^{k+1}-W^n}{\Delta t}+\partial_x F(W^n)\right)-\partial_x((4\eta H^n+\delta^n)\underline{\mathcal{I}}\,\partial_x W^{k+1})$$

$$=-\beta\underline{\mathcal{I}}W^{k+1}+S(W^n)\partial_x\overline{\sigma}^k, \tag{2.47}$$

where

$$D(W^n)=\begin{pmatrix}1&0\\0&H^n\end{pmatrix},\quad F(W^n)=\begin{pmatrix}H^n V^n\\ \frac{(V^n)^2}{2}-f_z H^n\end{pmatrix},\quad \underline{\mathcal{I}}=\begin{pmatrix}0&0\\0&1\end{pmatrix},$$

$$S(W^n)=\begin{pmatrix}0&0\\H^n&1\end{pmatrix},\quad \overline{\sigma}^k=\begin{pmatrix}f_\Omega x+f_z b\\ \zeta^k\end{pmatrix}.$$

The definition for δ^n and ζ^k depends on the duality method.
An important point is that discrete variables have different locations on the space mesh depending on their nature associated to the duality method. This is quite classical in numerical analysis but it proves crucial in the present context. We denote by W_i^{k+1} the approximation of the cell average of the exact solution provided by the numerical scheme:

$$W_i^{k+1}\cong\frac{1}{\Delta x}\int_{x_{i-1/2}}^{x_{i+1/2}}W^{k+1}(x)\,dx. \tag{2.48}$$

As said, duality variables (like μ in the AL) are approximated at the center of the dual mesh, namely $\zeta^k_{i+1/2}$ is the approximation of $\zeta^k(x_{i+1/2})$.

System (2.47) is then classically discretized as:

$$D(W_i^n)\left(\frac{W_i^{k+1}-W_i^n}{\Delta t}+\frac{\phi(W_i^n,W_{i+1}^n,\{\zeta^k_{j+1/2}\}_{j=i-1}^{j=i+1})-\phi(W_{i-1}^n,W_i^n,\{\zeta^k_{j+1/2}\}_{j=i-2}^{j=i})}{\Delta x}\right)$$

$$-\frac{1}{\Delta x^2}\left((4\eta H^n_{i+1/2}+\delta^n_{i+1/2})\underline{\mathcal{I}}\,(W_{i+1}^{k+1}-W_i^{k+1})-(4\eta H^n_{i-1/2}+\delta^n_{i-1/2})\underline{\mathcal{I}}\,(W_i^{k+1}-W_{i-1}^{k+1})\right)$$

$$=-\beta\underline{\mathcal{I}}W_i^{k+1}+S(W_i^n)\frac{\overline{\sigma}^k_{i+1/2}-\overline{\sigma}^{n,k}_{i-1/2}}{\Delta x}. \tag{2.49}$$

The key point is to design $\phi(W_i^n,W_{i+1}^n,\{\zeta^k_{j+1/2}\}_{j=i-1}^{j=i+1})$, the numerical flux function, approximation of $F(W^n)$ at $x_{i+1/2}$. Following [Cha+07], in order to obtain a well-balanced finite volume method, the numerical flux ϕ must depend on the definition of the source terms. Namely, we consider the following class of numerical flux functions:

$$\phi(W_i^n,W_{i+1}^n,\{\zeta^k_{j+1/2}\}_{j=i-1}^{j=i+1})=\frac{F(W_i^n)+F(W_{i+1}^n)}{2}$$
$$-\frac{1}{2}Q^n_{i+1/2}(W_{i+1}^n-W_i^n+\mathcal{G}^n(\{\zeta^k_{j+1/2}\}_{j=i-1}^{j=i+1})) \tag{2.50}$$

where $Q^n_{i+1/2}$ is the numerical viscosity matrix which particularizes the numerical solver and $\mathcal{G}(\{\zeta^k_{j+1/2}\}_{j=i-1}^{j=i+1})$ is a term *designed to obtain a well-balanced* finite volume method.
The numerical viscosity matrix can be defined in terms of the eigenvalues of the Roe matrix associated to the flux $F(W)$. Let us denote by $\mathcal{A}^n_{i+1/2}$ the Roe matrix verifying,

$$F(W^n_{i+1}) - F(W^n_i) = \mathcal{A}^n_{i+1/2}(W^n_{i+1} - W^n_i).$$

This matrix can be diagonalized and its eigenvalues are

$$\Lambda^n_{1,i+1/2} = \tilde{V}^n_{i+1/2} - \sqrt{-f_z H^n_{i+1/2}}, \quad \Lambda^n_{2,i+1/2} = \tilde{V}^n_{i+1/2} + \sqrt{-f_z H^n_{i+1/2}},$$

where $\tilde{V}^n_{i+1/2} = (\sqrt{H^n_i}V^n_i + \sqrt{H^n_{i+1}}V^n_{i+1})/(\sqrt{H^n_i} + \sqrt{H^n_{i+1}})$.
In present works, we consider Rusanov's method, defined by $Q^n_{i+1/2} = \alpha_{0,i+1/2} I$ with $\alpha_{0,i+1/2} = \max(|\Lambda^n_{1,i+1/2}|, |\Lambda^n_{2,i+1/2}|)$. As discussed in [Aca+12], using a diagonal viscosity matrix allows us to design an algorithm where at a first step we compute the flux associated to the velocity, at a second step we perform a fixed point algorithm, and finally we compute the flux associated to the height evolution. As a consequence, in the fixed point process of the duality method it is not necessary to recompute the numerical fluxes at each step. See [Aca+12][2] for more details on this discussion.

For $\mathcal{G}$, we propose the following definition:

$$\mathcal{G}^n(\{\zeta^k_{j+1/2}\}_{j=i-1}^{j=i+1}) = \frac{1}{f_z}\begin{pmatrix} f_\Omega\,\Delta x + f_z\,(b_{i+1} - b_i) + \frac{\Delta(\zeta + \delta^n\,\partial_x V)^k_{i+1/2}}{H_{i+1/2}} \\ 0 \end{pmatrix}, \tag{2.51}$$

where $\Delta(\zeta + \delta^n\,\partial_x V)^k_{i+1/2}/\Delta x$ is an approximation of $\partial_x(\zeta + \delta\,\partial_x V)^k$ at $x_{i+1/2}$.
The construction of $\Delta(\zeta + \delta^n\,\partial_x V)^k_{i+1/2}$ is based on a convex combination, by using a flux limiter function, of a second order approximation and a first order one:

$$\Delta(\zeta + \delta^n\,\partial_x V)^k_{i+1/2} = \mathcal{D}(d_l, d_c, d_r, s_{-1}, s_0, s_1, s_2), \tag{2.52}$$

with

$$d_l = \zeta^k_{i-1/2} + \delta^n_{i-1/2}\frac{V^k_i - V^k_{i-1}}{\Delta x}, \quad d_c = \zeta^k_{i+1/2} + \delta^n_{i+1/2}\frac{V^k_{i+1} - V^k_i}{\Delta x},$$

$$d_r = \zeta^k_{i+3/2} + \delta^n_{i+3/2}\frac{V^k_{i+2} - V^k_{i+1}}{\Delta x}, \quad s_j = H^n_{i+j} + b_{i+j}, \quad j = -1, 0, 1, 2.$$

The function $\mathcal{D}/\Delta x$ is defined by a combination of a second order approximation of $\partial_x(\zeta + \delta^n\,\partial_x V)$ at $x = x_{i+1/2}$ with a first order

2 Precisely on pages 19 and 21 of this link.

one, by means of a flux limiter function. We propose the following definition:

$$\mathcal{D}(d_l, d_c, d_r, s_{-1}, s_0, s_1, s_2) = \chi \frac{d_r - d_l}{2} + (1-\chi)\overline{\Delta d}_1,$$

with

$$\overline{\Delta d}_1 = \begin{cases} d_c - d_l & \text{if } s_0 < s_1, \\ d_r - d_c & \text{if } s_0 > s_1, \\ (d_r - d_l)/2 & \text{if } s_0 = s_1. \end{cases}$$

Remark that one of the difficulties of the 2D problem is the definition of $\mathcal{D}(d_l, d_c, d_r, s_{-1}, s_0, s_1, s_2)$ allowing to recover the second order well-balanced properties. These will be treated in the next chapter.

The term $\chi = \chi(\nu(s_{-1}, s_0, s_1, s_2))$ is a flux limiter function with $\nu(s_{-1}, s_0, s_1, s_2) \in [0, 1]$. We propose to define

$$\nu = \max(0, \min(1, \tilde{\nu})), \qquad \tilde{\nu} = \begin{cases} \frac{3(s_0 - s_{-1})}{s_2 - s_{-1}}, & \text{if } s_1 > s_0, \\ \frac{3(s_2 - s_1)}{s_2 - s_{-1}}, & \text{if } s_1 < s_0, \\ 1 & \text{if } s_1 = s_0 \text{ or } s_2 = s_{-1}, \end{cases}$$

and the following definition of the flux limiter function:

$$\chi(\nu) = 1 - (1 - \nu^{1/4})^4.$$

The definition of this limiter is driven by the fact that we want to put a stronger weight of the second order approximation ($\frac{d_r - d_l}{2}$) compared to the first order one ($\overline{\Delta d}_1$). This comes from the general idea which consists in using, when possible, second order approximation and activating the first order one, in critical situations.

The description of the global discretization schemes is thus essentially complete, in the case *without* wet/dry fronts. Indeed to get the spatial discretization of problem of the type $(P)^{n,k}$ (2.43) we just distribute the first and second components of (2.49) to the equation on H and the problem on V, respectively.
To give an idea of the global coupled scheme obtained using this distribution, we can write the Bermúdez-Moreno version (instead of the AL; this allows to show the very similar structure compared to the Augmented Lagrangian on page 19): here $\zeta = \theta$ which is the duality variable of the BM, equivalent of μ in the AL.

Global numerical scheme for (2.33)-(2.35) – Bermúdez-Moreno method

- **Initialization** at time $t = 0$ for $n = 0$: V^n, H^n, θ^n are given by the initial conditions.
- **Time loop**: For $n = 0, ..., n_{max}$.
  - **Resolution of the problem on V^{k+1}**
    $\{V_i^n\}_i$, $\{H_i^n\}_i$ and $\{\theta_{i+1/2}^n\}_i$ are known.
    Compute quantities which are invariant in the following loop:
    Bermúdez-Moreno loop:

    [Step 0] Initialize for $k = 0$: for all i, $V_i^k = V_i^n$ and $\theta_{i+1/2}^k = \theta_{i+1/2}^n$.

    [Step 1] Update $\{V_i^{k+1}\}_i$ by solving the linear system defined by the second component of (2.49).

    [Step 2] Compute the auxiliary variable $\{\xi_{i+1/2}^{k+1}\}_i$:

$$\xi_{i+1/2}^{k+1} = \frac{V_{i+1}^k - V_i^k}{\Delta x} + \lambda \theta_{i+1/2}^k. \tag{2.53}$$

    [Step 3] Update $\{\theta_{i+1/2}^{k+1}\}_i$ via

$$\theta_{i+1/2}^{k+1} = \begin{cases} \frac{-\omega\, \xi_{i+1/2}^{k+1} + \tau_y \sqrt{2} H_{i+1/2}^n}{1 - \lambda\, \omega} & \text{if } \xi_{i+1/2}^{k+1} > \lambda \tau_y \sqrt{2} H_{i+1/2}^n, \\ \frac{\xi_{i+1/2}^{k+1}}{\lambda} & \text{if } \xi_{i+1/2}^{k+1} \in [-\lambda \tau_y \sqrt{2} H_{i+1/2}^n, \lambda\, \tau_y \sqrt{2} H_{i+1/2}^n], \\ \frac{-\omega\, \xi_{i+1/2}^{k+1} - \tau_y \sqrt{2} H_{i+1/2}^n}{1 - \lambda\, \omega} & \text{if } \xi_{i+1/2}^{k+1} < -\lambda \tau_y \sqrt{2} H_{i+1/2}^n. \end{cases} \tag{2.54}$$

    [Step 4] Set: for all i, $V_i^k = V_i^{k+1}$, $\theta_{i+1/2}^k = \theta_{i+1/2}^{k+1}$ and return to Step 1.

    [Step 5] At convergence, set $V_i^{n+1} = V_i^{k+1}$ and $\theta_{i+1/2}^{n+1} = \theta_{i+1/2}^{k+1}$ $\forall i$.
  - **Resolution of the problem on H^{k+1}**
    Compute $H^{n+1} = H^{k+1}$ with the finite volume method defined by the first component of (2.49), defined in terms of *the most recent multiplier* $\{\theta_{i+1/2}^{n+1}\}_i$.

Wet/dry fronts corrections.

The previous description need to be adapted *in the presence of wet/dry fronts*. We will now describe this adaptation inspired by the work [CGP06] and here extended to the situation where the material can be fluid or plastic.

From the numerical point of view, we said that H_i is null when $H_i < H_\varepsilon$. For the numerical tests we set $H_\varepsilon = 5 \cdot 10^{-3}$.

In some of the cases described below, we impose no numerical diffusion in the discretization of the equation in H and a local equilibrium of the pressure term. In practice this corresponds to set the following definitions of $\Delta(\zeta + \delta^n \partial_x V)^k_{i+1/2}$ and $\overline{\sigma}^k_{i+1/2}$:

- If $H_{i-1} \leqslant H_\varepsilon$, $H_i \leqslant H_\varepsilon$, $H_{i+1} \leqslant H_\varepsilon$ or $H_{i+2} \leqslant H_\varepsilon$ and the material is rigid enough in the following sense:
  - for the AL algorithm, if $\left|\mu^n_{i+1/2} + r\frac{v_{i+1}-v_i}{\Delta x}\right| < \tau_y\sqrt{2}$;
  - for the BM algorithm, if $\left|\theta^n_{i+1/2} + \frac{1}{\lambda^n_{i+1/2}}\frac{v_{i+1}-v_i}{\Delta x}\right| < H^n_{i+1/2}\tau_y\sqrt{2}$;

  then we set the following definitions of $\Delta(\zeta + \delta^n \partial_x V)^k_{i+1/2}$ and $\overline{\sigma}^k_{i+1/2}$:

$$\Delta(\zeta + \delta^n \partial_x V)^k_{i+1/2} = -f_z H^n_{i+1/2}(b_{i+1} - b_i - H_i + \tfrac{f_\Omega}{f_z}\Delta x),$$
$$\overline{\sigma}^k_{i+1/2} = \begin{pmatrix} f_\Omega\, x_i + f_z b_i + \frac{1}{2} f_z H_i \\ \\ \zeta^k_{i-1/2} \end{pmatrix}. \tag{2.55}$$

- If $H_i \leqslant H_\varepsilon$ or $H_{i+1} \leqslant H_\varepsilon$ and if
  - for the AL algorithm, if $\left|\mu^n_{i+1/2} + r\frac{v_{i+1}-v_i}{\Delta x}\right| \geqslant \tau_y\sqrt{2}$;
  - for the BM algorithm, if $\left|\theta^n_{i+1/2} + \frac{1}{\lambda^n_{i+1/2}}\frac{v_{i+1}-v_i}{\Delta x}\right| \geqslant H^n_{i+1/2}\tau_y\sqrt{2}$;

  we proceed as follows. Let us suppose that $H_i > H_\varepsilon$ and $H_{i+1} \leqslant H_\varepsilon$. Then, if

$$b_i + H_i < b_{i+1} \tag{2.56}$$

  we set the definition (2.55). Moreover, if $V_{i+1} < 0$, then we set $V_{i+1} = 0$ in the computation of the numerical flux for the evolution of the height of the material. If $H_i \leqslant H_\varepsilon$, $H_{i+1} > H_\varepsilon$, then we apply the same treatment symmetrically.

Let us remark that in this approach, we test whether the material is fluid or rigid. For example, let us consider the case $\tau_y = 0$, i.e. the fluid regime. In this case, it is important to check the relative position of the free surface at $x = x_i$ and $x = x_{i+1}$, which coincides with the wet/dry numerical treatment proposed in [CGP06] for the shallow

water equations. On the contrary, when the material is rigid enough, it is not important to check the relative position of the free surface. Because in this case, the rigidity naturally implies that the solution is at rest independently of the relative position of the free surface.

A short illustration to finish.

Among the numerous simulations done in [FGV14] and to which the reader is referred, we just give below one illustration of the performance of these schemes. Namely, it is an academic 1D avalanche (dam break problem) over an Ω plane with angle $\alpha = 30^o$ and a bottom b with two "obstacles" (see Figure 2.3). The mesh has 200 cells on a domain with $L = 10$.

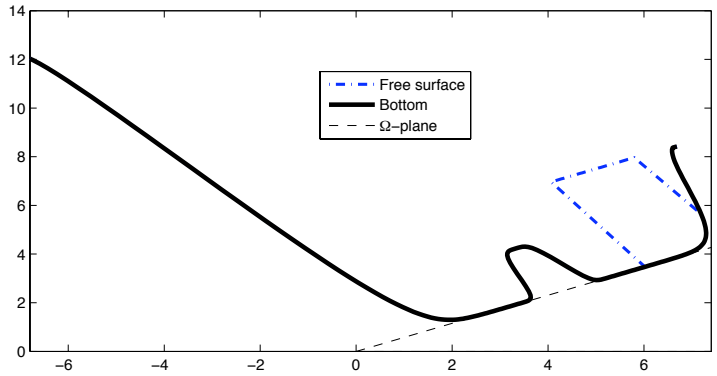

Figure 2.3: Academic avalanche: bottom and initial condition for H.

There are two difficulties in this test related to the wet/dry fronts. First, in the evolution of the avalanche, the obstacle in the middle of the domain splits the avalanche in two parts. Second, the part of the avalanche arriving at the far left of the domain goes up on a high bed which limits its movement. This leads to a back and forth motion that eventually ends to a stationary state when all the material becomes rigid. This back and forth motion goes faster to stationary state when τ_y increases. But the associated free surface has a more complex shape, which is also due to the complex non-linear interaction of the material when it passes over the obstacle inducing the splitting of the material in the two basins.
Some snapshots of this evolution are given in Figure 2.4: stationary state is computed with a good accuracy with a velocity smaller than 16×10^{-10} at $t = 24$, given the non trivial shape of the free surface on this slope.
For the right column representing V, we can remark zones with evidence of rigidity: we can distinguish clearly some zones with constant velocity, that is, zones where the material moves as a block.

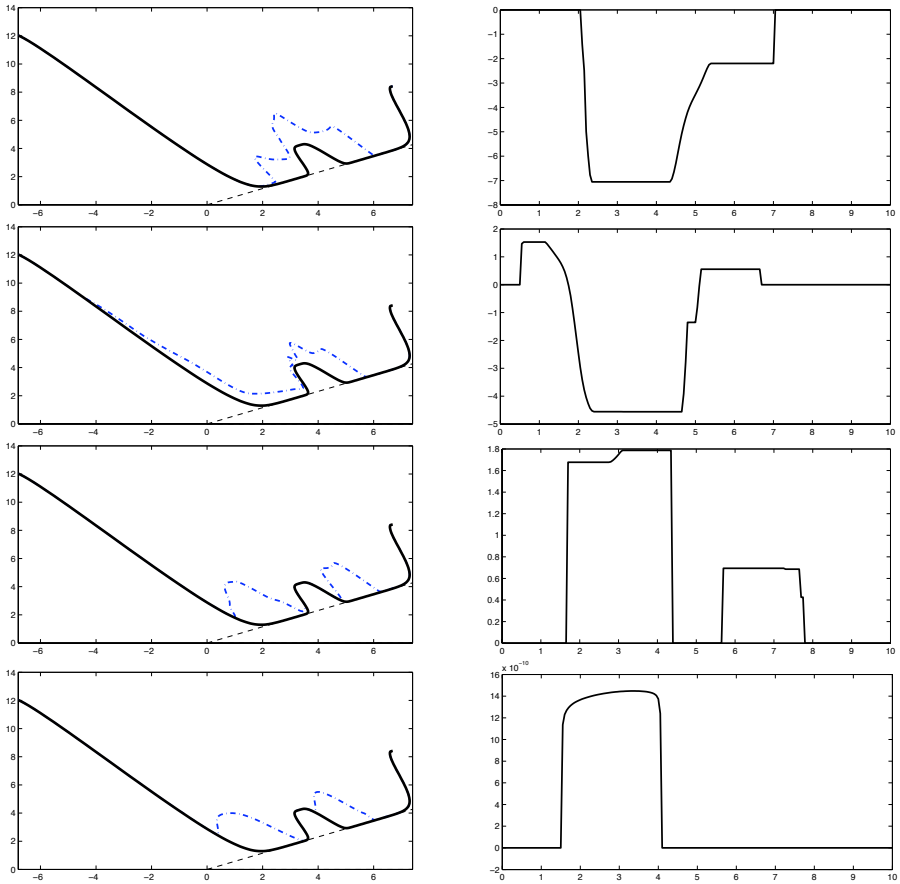

Figure 2.4: Academic avalanche with $\tau_y = 8$: from top to bottom, time evolution at $t = 1, 1.5, 2$ and 24. Left: H. Right: V.

In the next chapter, we describe the extension of the present schemes to the 2D framework.

3

NUMERICAL SCHEMES FOR 2D VISCOPLASTIC AVALANCHES

This chapter is the object of a submitted article [1], with E. D. Fernandez-Nieto and J.M. Gallardo, which is the natural follow-up of [FGV14].

Submitted, March 2017

3.1 INTRODUCTION

We deal here with the most general framework for the simulation of viscoplastic (Bingham) avalanches with wet/dry fronts on general 2D bottoms, thanks to a shallow water model discretized with a finite volume method. This approach has several motivations: (i) finite volume methods are used in nearly 40% of the discretizations of geophysical avalanches (40% of the rest being done with finite difference methods) as mentioned in the review [YA16], (ii) we use the variational inequality framework with duality methods which have proved to be the most accurate for the computation of viscoplastic flows, see [SW17], (iii) enrichment of geophysical shallow models towards viscoplastic behaviour is increasingly in use to take into account the material ability to rigidify [Anco7; YA16; SW17], (iv) the prototypical shallow viscoplastic model covered in this paper is well adapted to (wet) dense snow avalanches (by opposition to powder snow avalanches) which are occurring more and more frequently with the global warming of the atmosphere (see [AB15]).
In the present work, we extend in 2D the 1D schemes developed in [FGV14]. We make a careful study of the ability of the schemes to compute the stationary states of an avalanche. This is done thanks to a coupling between the finite volume method used for the discretization in space and the duality method used to solve the non-Newtonian character of the material. This leads to an extended notion of viscoplastic well-balancing. In this case, we say that the method is well-balanced if it preserves exactly two kinds of stationary solutions: (i) material at rest independently of the rigidity of the material and (ii) rigid enough material with free surface parallel to a reference plane. Let us remark that the latter is more relevant for viscoplastic materials, nevertheless it is necessary to preserves also the first one, material at rest, in order to be consistent with a numerical method for a Newtonian fluid when τ_y tends to zero. We study also the numerical cost and (when possible) the *a priori* estimation of the optimal intrinsic

1 At the time of writing of this HDR. It is now accepted in *Journal of Computational Physics* (Sept. 25, 2017). Efficient numerical schemes for viscoplastic avalanches. Part 2: the 2D case [FGV18].

parameter of two duality methods: the augmented Lagrangian (AL) and the Bermúdez-Moreno (BM) methods. Note that the schemes proposed here can be extended straightforwardly to power viscoplastic laws (such as Herschel-Bulkley). Several computational tests illustrate the performances of the schemes. First, we consider a 2D Couette geometry for which we propose a generalized analytic solution with two non-zero boundary conditions on the velocity (usual solutions assume that one of the boundary is fixed). This can be a benchmark for testing classic 2D Bingham codes. Second, we study the well-balanced property for rigid materials by considering a complex random bottom on a 30° slope reference plane: the free surface is parallel to the reference plane and has complex wet/dry fronts. Third, we build a numerically demanding 2D academic dam break test on a complex topography where the final stationary solution exhibits strong gradients of the free surface at the wet/dry front. Finally, we show the ability of the schemes to compute the final stationary state of an avalanche on a real topography (given by the ASTER Digital Elevation Model): we used historical data of (frequent) avalanches at the Taconnaz path in the Mont-Blanc, one of the longest site in Europe with a path close to 7km. This test involves a large computation domain and long physical times with a rich dynamics of the progressive stopping of the avalanche.

In section 3.2, we recall the model under consideration. In section 3.3, we derive the 2D versions of the augmented-Lagrangian and the Bermúdez-Moreno methods. For the latter, we give a theoretical a priori estimation of duality parameter which leads to smallest computational time of the duality resolution. This is associated to the computation of the velocity field. We then detail (section 3.4) the construction and properties of the 2D well-balanced finite volume method for the space discretization. Numerical illustrations are finally presented in section 3.5.

3.2 MODELS

The model problem for viscoplastic shallow flows is naturally the one presented in the first part of this work [FGV14]. We refer to [Bre+10] for more details. The geometry is as shown on Figure 3.1. We consider a fluid domain of height H over a general bottom b. More precisely, let $\Omega \subset \mathbb{R}^2$ be a given domain for the space variable $\mathbf{x}$. The $\mathbb{R}^2$ plane generated by Ω is supposed to be sloping at an angle α from the horizontal plane. We denote by $z \in \mathbb{R}$ the variable in the orthogonal direction to Ω. The bottom which bounds the fluid by below is defined by $b(\mathbf{x}), \mathbf{x} \in \Omega$. We denote by $\mathcal{D}(t)$ the fluid domain defined as

$$\mathcal{D}(t) = \{(\mathbf{x}, z) \in \Omega \times \mathbb{R} \,/\, b(\mathbf{x}) < z < b(\mathbf{x}) + H(t, \mathbf{x})\}, \tag{3.1}$$

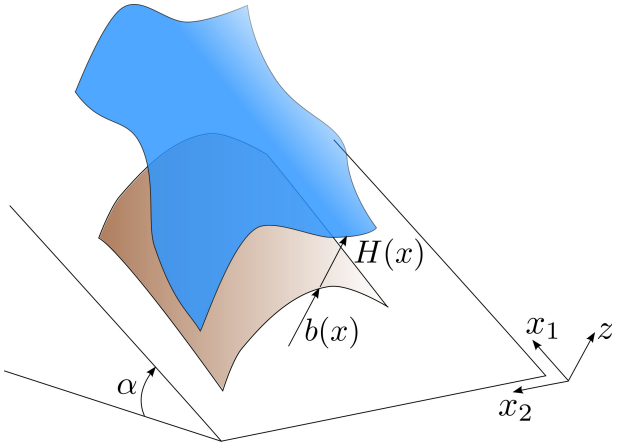

Figure 3.1: Sketch of the 2D domain and convention for the *local* coordinates. $\mathbf{x} = (x_1, x_2)$

where H is the time-dependent height of the fluid.

As usual for shallow water type models, we denote by $V = V(t, \mathbf{x}) \in \mathbb{R}^2$ the vector of the average of the velocity (orthogonal to the z-axis) along the depth of the fluid (i.e. from $z = b(\mathbf{x})$ to $z = b(\mathbf{x}) + H(t, \mathbf{x})$). We take into account the fact that there may be friction on the bottom through a coefficient β. The fluid undergoes a body force denoted as $(f_\Omega, f_z) \in \mathbb{R}^2 \times \mathbb{R}$ in the $\Omega \times z$ frame of reference. Note that f_Ω and f_z are both assumed to be constant.
Since we are considering a Bingham constitutive law, the material is characterized by a viscosity η and a yield stress τ_y. The latter is associated to the plastic behaviour of the material and this leads (cf. [DL76]) to a variational inequality for the momentum conservation relation (see equation 3.4). On the contrary, the conservation of mass is rather classic for this type of integrated model (see equation 3.3). Given the space

$$\mathcal{V}(t) = \{\Psi \in H^1(\Omega)^2 \ / \ \Psi = 0 \text{ on } \partial\Omega\} := H^1_0(\Omega)^2 \tag{3.2}$$

and some initial conditions at $t = 0$, the problem is to find $H \in L^2([0,T], L^\infty(\Omega))$, $V \in L^2([0,T]; \mathcal{V}(t))$, with $\partial_t H \in L^2([0,T]; L^2(\Omega)^2)$, such that

$$\partial_t H + \operatorname{div}_{\mathbf{x}}(HV) = 0, \tag{3.3}$$

and

$$\forall \Psi \in \mathcal{V}(t), \quad \int_\Omega H\Big(\partial_t V + (V\cdot\nabla_x)V\Big)\cdot(\Psi - V)dx + \int_\Omega \beta V\cdot(\Psi - V)dx$$
$$+ \int_\Omega 2\eta H D(V) : D(\Psi - V)dx + \int_\Omega 2\eta H div_x V(div_x\Psi - div_x V)dx$$
$$+ \int_\Omega \sqrt{2}\tau_y H\Big(\sqrt{D(\Psi)\colon D(\Psi) + (div_x\Psi)^2} - \sqrt{D(V)\colon D(V) + (div_x V)^2}\Big)dx$$
$$\geqslant \int_\Omega H(f_\Omega + f_z\,\nabla_x b)\cdot(\Psi - V)dx - \int_\Omega \frac{H^2}{2} f_z(div_x\Psi - div_x V)dx, \qquad (3.4)$$

where

$$D(U) := \frac{1}{2}\left[\nabla_x U + (\nabla_x U)^t\right], \qquad (3.5)$$

$$\nabla_x U := \left(\frac{\partial U_i}{\partial x_j}\right)_{i,j}, \quad i = 1,2,\ j = 1,2, \qquad (3.6)$$

$$div_x U := \frac{\partial U_1}{\partial x_1} + \frac{\partial U_2}{\partial x_2}, \qquad \forall\, U(t,\cdot) := (U_1, U_2) \in \mathcal{V}(t). \qquad (3.7)$$

The *shallow water* formulation (2.24) is in weak form. Note that the derivation of (2.24) comes from the asymptotic analysis of the integrated 3D equations: this explains why we first present this variational form. From (2.24), we can then find the strong (i.e. non-variational) form (2.29)-(2.30) , which is clearer to read. Obviously, we obtain a Bingham constitutive law but it is modified compared to the canonical law. Indeed, the integration of the 3D equations to the 2D form leads to an *integrated* Bingham law (2.30) (with corrector terms $tr(D(V))I$). Let us consider the space $X = \mathbb{R}^{2\times 2}$ with scalar product $(p,q) := (p\colon q + tr(p)\,tr(q))$ and associated norm $\|\cdot\|$. That is, for $p \in X$,

$$\|p\| = \sqrt{\sum_{i,j} p_{i,j}^2 + \left(\sum_i p_{i,i}\right)^2}. \qquad (3.8)$$

By using this notation the strong formulation of (2.24) can be written as follows:

$$H\Big(\partial_t V + (V\cdot\nabla_x)V\Big) - div_x(H\sigma) = H(f_\Omega + f_z\,\nabla_x b) - \nabla_x\left(\frac{H^2}{2} f_z\right) - \beta V, \qquad (3.9)$$

where

$$\begin{cases} \sigma = 2\eta\,(D(V) + tr(D(V))I) + \sqrt{2}\tau_y \frac{D(V)+tr(D(V))I}{\|D(V)\|^2} & \text{if } \|D(V)\| \neq 0 \\ \\ \|\sigma\| \leqslant \sqrt{2}\tau_y & \text{if } \|D(V)\| = 0. \end{cases}$$

(3.10)

Let us remark that the $\sqrt{2}$ factor multiplying τ_y appears because of the use of Frobenius norm. Then, the actual formulation is equivalent to the one considering a Eulerian norm.

Note that in the following, the body force will be the influence of gravity, denoted by g. To write this force, we must decide what is the orientation of the plane generated by Ω; by convention we will say that if (x_1, x_2, z) is the frame of reference (cf. Figure 3.1), then the tilted axis (with respect to the horizontal) is x_1, i.e.

$$f_\Omega = (-g \sin\alpha\,,\, 0), \quad f_z = -g\cos\alpha. \tag{3.11}$$

Note also that for numerical accuracy, it is often better to consider the simulation of geophysical flows over large domains (like for instance in Section 3.5.4 for the Taconnaz avalanche path) by rescaling the equations to simulate the flow on a domain of order one length. Namely, we introduce a characteristic horizontal length L_c and vertical height H_c. We then make the following rescaling (denoting $\epsilon = H_c/L_c$):

$$\begin{aligned} &\mathbf{x} = L_c\tilde{\mathbf{x}},\ z = H_c\tilde{z},\ t = \frac{L_c}{\sqrt{gH_c}}\tilde{t},\ b = H_c\tilde{b},\ V = \sqrt{gH_c}\tilde{V},\\ &\eta = H_c\sqrt{gH_c}\tilde{\eta},\ \tau_y = \epsilon g H_c\tilde{\tau_y},\ \beta = \epsilon\sqrt{gH_c}\tilde{\beta},\ f_\cdot = g\tilde{f}_\cdot. \end{aligned} \tag{3.12}$$

In these new variables (and omitting the tildes), (3.4) reads:

$$\begin{aligned} &\forall \Psi \in \mathcal{V}(t), \quad \int_\Omega H\Big(\partial_t V + (V\cdot\nabla_{\mathbf{x}})V\Big)\cdot(\Psi - V)d\mathbf{x} + \int_\Omega \beta V\cdot(\Psi - V)d\mathbf{x}\\ &+ \int_\Omega \epsilon 2\eta H D(V) : D(\Psi - V)d\mathbf{x} + \int_\Omega \epsilon 2\eta H \mathrm{div}_{\mathbf{x}} V(\mathrm{div}_{\mathbf{x}}\Psi - \mathrm{div}_{\mathbf{x}} V)d\mathbf{x}\\ &+ \int_\Omega \epsilon\sqrt{2}\tau_y H\Big(\|D(\Psi)\| - \|D(V)\|\Big)d\mathbf{x}\\ &\geqslant \int_\Omega H(f_\Omega + f_z\,\nabla_{\mathbf{x}} b)\cdot(\Psi - V)d\mathbf{x} - \int_\Omega \frac{H^2}{2} f_z(\mathrm{div}_{\mathbf{x}}\Psi - \mathrm{div}_{\mathbf{x}} V)d\mathbf{x}. \end{aligned} \tag{3.13}$$

As most often done in the literature and since the main objective of this work is to treat the viscoplastic discretization difficulty, we consider a first order backward semi-discretization in time. If we denote by Δt the time step, we have from (3.3)-(3.4) :

$$\frac{H^{n+1} - H^n}{\Delta t} + \mathrm{div}_{\mathbf{x}}(H^n V^n) = 0, \tag{3.14}$$

and

$$\int_\Omega H^n\left(\frac{V^{n+1}-V^n}{\Delta t}+(V^n\cdot\nabla_x)V^n\right)\cdot(\Psi-V^{n+1})dx+\int_\Omega \beta V^{n+1}\cdot(\Psi-V^{n+1})dx$$
$$+\int_\Omega 2\eta H^n D(V^{n+1}):D(\Psi-V^{n+1})dx+\int_\Omega 2\eta H^n div_x V^{n+1}(div_x\Psi-div_x V^{n+1})dx$$
$$+\int_\Omega \sqrt{2}\tau_y H^n\Big(\|D(\Psi)\|-\|D(V^{n+1})\|\Big)dx$$
$$\geqslant\int_\Omega H^n(f_\Omega+f_z\nabla_x b)\cdot(\Psi-V^{n+1})dx-\int_\Omega\frac{(H^n)^2}{2}f_z(div_x\Psi-div_x V^{n+1})dx,\quad\forall\Psi.$$

Doing so, we see that problems on the height and on the velocity are decoupled. At each time step, supposing that we know (H^n,V^n), we need to solve both problems for (H^{n+1},V^{n+1}). As in the companion paper [FGV14], we compare two duality methods to handle the variational inequality of the problem on the velocity, namely the Augmented Lagrangian method and Bermúdez-Moreno method. It is the subject of the next section.

3.3 DUALITY METHODS IN 2D

3.3.1 *The AL approach*

We will extend in 2D the derivation done in [FGV14]. Supposing that (H^n,V^n) are known, the goal is here to solve the problem (3.15) for V^{n+1}. Using *ad hoc* spaces, variational inequality (3.15) is now equivalent to a minimization problem

$$\mathcal{J}^n(V^{n+1}) \quad = \quad \min_{V\in\mathcal{V}}\mathcal{J}^n(V), \tag{3.16}$$

where $\mathcal{J}^n(V)=F^n(B(V))+G^n(V)$, with $\mathcal{V}=(H_0^1(\Omega))^2$. Let us also denote $\mathcal{H}=L^2(\Omega)^{2\times2}$,

$$B:\begin{pmatrix}\mathcal{V}&\to&\mathcal{H}\\ V&\mapsto&B(V)=D(V)\end{pmatrix},\qquad F^n:\begin{pmatrix}\mathcal{H}&\to&\mathbb{R}\\ \lambda&\mapsto&F^n(\lambda)=\int_\Omega\tau_y H^n\|\lambda\|dx\end{pmatrix},$$

and

$$G^n:\mathcal{V}\to\mathbb{R},$$

$$\begin{aligned}G^n(V) \quad = \quad &\int_\Omega H^n\left(\frac{|V|^2/2-V^n\cdot V}{\Delta t}+(V^n\cdot\nabla_x V^n)\cdot V\right)dx+\int_\Omega\beta\frac{|V|^2}{2}dx\\ &+\int_\Omega\eta H^n\|B(V)\|^2dx-\int_\Omega H^n\,(f_\Omega+f_z\,\nabla_x b)\cdot Vdx\\ &+\int_\Omega f_z\frac{(H^n)^2}{2}div_x Vdx.\end{aligned}$$

In 2D, we define the Lagrangian functional by

$$\mathcal{L}^n:\mathcal{V}\times\mathcal{H}\times\mathcal{H}\to\mathbb{R},$$

$$\mathcal{L}^n(V, q, \mu) = F^n(q) + G^n(V) + \int_\Omega H^n(\mu, B(V) - q)dx,$$

and the augmented Lagrangian functional, for a given positive value $r \in \mathbb{R}$, as:

$$\mathcal{L}^n_r(V, q, \mu) = \mathcal{L}^n(V, q, \mu) + \frac{r}{2}\int_\Omega H^n \|B(V) - q\|^2 dx. \tag{3.17}$$

Again, we determine the saddle point of $\mathcal{L}^n_r(V, q, \mu)$ over $\mathcal{V} \times \mathcal{H} \times \mathcal{H}$ thanks to an augmented Lagrangian algorithm (cf. [FG83]).

Augmented Lagrangian algorithm (2D)

- **Initialization**: suppose that V^n, H^n and μ^n are known. For $k = 0$, we set $V^k = V^n$ and $\mu^k = \mu^n$.
- **Iterate**:
  - Find $q^{k+1} \in \mathcal{H}$ solution of

$$\mathcal{L}^n_r(V^k, q^{k+1}, \mu^k) \leqslant \mathcal{L}^n_r(V^k, \underline{q}, \mu^k), \quad \forall \underline{q} \in \mathcal{H}.$$

    In other words, $q^{k+1} \in \mathcal{H}$ is the solution of following minimization problem:

$$\min_{\underline{q}\in\mathcal{H}} \left(\frac{H^n r}{2}\|\underline{q}\|^2 + H^n\sqrt{2}\tau_y \, \|\underline{q}\| - H^n(\mu^k + rB(V^k)) : \underline{q} - H^n \operatorname{tr}(\mu^k + rB(V^k)) \operatorname{tr}(\underline{q}) \right). \tag{3.18}$$

    And the solution of this problem is computed locally for all $x \in \Omega$:

$$q^{k+1} = \begin{cases} 0 & \text{if } \|\mu^k + rB(V^k)\| < \sqrt{2}\tau_y, \\ \dfrac{1}{r}\left((\mu^k + rB(V^k)) - \sqrt{2}\tau_y \, \dfrac{\mu^k + rB(V^k)}{\|\mu^k + rB(V^k)\|} \right) & \text{otherwise.} \end{cases} \tag{3.19}$$

  - Find $V^{k+1} \in \mathcal{V}$ solution of

$$\mathcal{L}^n_r(V^{k+1}, q^{k+1}, \mu^k) \leqslant \mathcal{L}^n_r(V, q^{k+1}, \mu^k), \quad \forall V \in \mathcal{V}.$$

    From (3.17), by differentiating $\mathcal{L}^n_r(V, q, \mu)$ with respect to V, we deduce that V^{k+1} is the solution of the following linear problem (whose resolution is detailed in Section 3.4):

$$\begin{aligned} H^n \left(\frac{V^{k+1} - V^n}{\Delta t} \right) + \beta V^{k+1} - (2\eta + r) \left(\operatorname{div}_x(H^n D(V^{k+1})) \right. \\ \left. + \nabla_x(H^n \operatorname{div}_x(V^{k+1})) \right) + H^n(V^n \cdot \nabla_x V^n) - (f_\Omega + f_z \, \nabla_x b) \, H^n \\ - \nabla_x \left(\frac{(H^n)^2}{2} f_z \right) - \operatorname{div}_x \left(H^n \left(\mu^k - r q^{k+1} \right) \right) \\ - \nabla_x \left(H^n \operatorname{tr}(\mu^k - r q^{k+1}) \right) = 0. \end{aligned} \tag{3.20}$$

- Update the Lagrange multiplier via

$$\mu^{k+1} = \mu^k + r\left(B(V^{k+1}) - q^{k+1}\right). \tag{3.21}$$

- Check convergence (see below) and update: $V^k = V^{k+1}$, $\mu^k = \mu^{k+1}$, $k = k+1$ and go to the next iteration ...

- ... **until** convergence is reached:

$$\frac{\|\mu^{k+1} - \mu^k\|}{\|\mu^k\|} \leqslant \text{tol}. \tag{3.22}$$

At convergence, we get the value of V^{n+1} by setting $V^{n+1} = V^{k+1}$ (in the numerical tests presented in this paper, we set $\text{tol} = 10^{-5}$). It is also shown in [FG83] that this algorithm converges to the saddle point of (3.17).

3.3.2 *The BM approach and its optimal parameter*

3.3.2.1 *The BM algorithm*

The BM algorithm in the two-dimensional case follows similar guidelines as in [FGV14], once a proper choice of norms is made. In particular, we use the space $\mathcal{V} = H_0^1(\Omega)^2$ endowed with the scalar product

$$(V, W)_{\mathcal{V}} = \int_\Omega D(V) : D(W)\,dx + \int_\Omega \text{div}_x(V)\text{div}_x(W)\,dx, \quad V, W \in \mathcal{V}.$$

It readily follows from the arithmetic-geometric mean property and Korn inequality that the associated norm

$$\|V\|_{\mathcal{V}} = \left(\|D(V)\|_{L^2}^2 + \|\text{div}_x(V)\|_{L^2}^2\right)^{1/2}$$

verifies $C_K^{-1}\|\nabla V\|_{L^2} \leqslant \|V\|_{\mathcal{V}} \leqslant \sqrt{3}\|\nabla V\|_{L^2}$, where C_K is a Korn constant. Therefore, the norm $\|\cdot\|_{\mathcal{V}}$ is equivalent to the norm $\|\nabla \cdot\|_{L^2}$ in $H_0^1(\Omega)^2$, so $\mathcal{V}$ turns out to be a Hilbert space. In a similar way, the space $\mathcal{H} = L^2(\Omega)^{2\times 2}$ is also a Hilbert space with the scalar product

$$(Z, W)_{\mathcal{H}} = \int_\Omega Z : W\,dx + \int_\Omega \text{tr}(Z)\,\text{tr}(W)\,dx,$$

as the associated norm is equivalent to $\|\cdot\|_{L^2}$. Notice also that $\|V\|_{\mathcal{V}} = \|B(V)\|_{\mathcal{H}}$ for every $V \in \mathcal{V}$.

Consider now the linear operator $A : \mathcal{V} \to \mathcal{V}'$ defined as

$$\langle A(V), \Psi\rangle = \int_\Omega \left(\frac{H^n}{\Delta t} + \beta\right) V \cdot \Psi\,dx + \int_\Omega 2\eta H^n D(V) : D(\Psi)\,dx$$

$$+ \int_\Omega 2\eta H^n \text{div}_x(V)\text{div}_x(\Psi)\,dx,$$

which is coercive with constant $\gamma = 2\eta H^n_{\min}$ (where $H^n_{\min} = \min H^n(\mathbf{x}) > 0$):

$$\langle A(V), V\rangle \geqslant \left(\frac{H^n_{\min}}{\Delta t} + \beta\right)\|V\|^2_{L^2} + 2\eta H^n_{\min}\|V\|^2_{\mathcal{V}} \geqslant 2\eta H^n_{\min}\|V\|^2_{\mathcal{V}}, \quad \forall V \in \mathcal{V}.$$

Define also the functional $j\colon \mathcal{V} \to \mathbb{R}$ given by

$$j(V) = \int_\Omega \sqrt{2}\tau_y H^n \sqrt{|D(V)|^2 + \mathrm{div}_x(V)^2}\,dx,$$

and let $L \in \mathcal{V}'$ be

$$\begin{aligned}\langle L, \Psi\rangle = &\int_\Omega \frac{H^n}{\Delta t}V^n \cdot \Psi dx - \int_\Omega H^n V^n \cdot \nabla_x V^n \Psi dx \\ &+ \int_\Omega H^n(f_\Omega + f_z\nabla_x b)\cdot\Psi dx - \int_\Omega \frac{(H^n)^2}{2} f_z \mathrm{div}_x(\Psi) dx.\end{aligned}$$

Then, the variational inequality (3.15) can be expressed as: Find $V \in \mathcal{V}$ such that

$$\langle A(V), \Psi - V\rangle + j(\Psi) - j(V) \geqslant \langle L, \Psi - V\rangle, \quad \forall \Psi \in \mathcal{V}. \tag{3.23}$$

Let $\Phi\colon \Omega \times X \to \mathbb{R}$ be the function

$$\Phi(\mathbf{x}, p) = \sqrt{2}\tau_y H^n(\mathbf{x})\|p\|,$$

and define $T\colon \mathcal{H} \to \mathbb{R}$ as

$$T(Z) = \int_\Omega \Phi(\mathbf{x}, Z(\mathbf{x}))dx.$$

Using that $\mathrm{div}_x(V) = \mathrm{tr}(D(V))$ we have $j(V) = T(B(V))$, where $B\colon \mathcal{V} \to \mathcal{H}$ is given by $B(V) = D(V)$. Now, reasoning as in [FGV14], the variational inequality (3.23) can be written as: Find $V \in \mathcal{V}$ and $\theta \in \mathcal{H}$ such that

$$\begin{cases} A(V) + \omega B^*(B(V)) + B^*(\theta^k) = L, \\ \theta = G^\omega_\lambda(B(V) + \lambda\theta), \end{cases} \tag{3.24}$$

where G^ω_λ is the Yosida approximation of $G^\omega = \partial T - \omega I$; the parameters λ and ω are arbitrary positive numbers satisfying $\lambda\omega < 1$. The BM method for (3.24) reads then as follows: For $k \geqslant 0$, θ^k being known, compute V^k and θ^{k+1} by solving

$$\begin{cases} A(V^k) + \omega B^*(B(V^k)) + B^*(\theta^k) = L, \\ \theta^{k+1} = G^\omega_\lambda(B(V^k) + \lambda\theta^k). \end{cases} \tag{3.25}$$

From now on we will assume the condition $\lambda\omega = 1/2$, which ensures the convergence of the BM algorithm and it is also fundamental in the computation of the optimal parameters in Section 3.3.2.2 (see [FGV14]

and the references therein).

Remark: The BM method share some conceptual properties with the iterative method introduced in [CG72] (see also [DGG07, Sect. 7.3]). This method is a version of the classical Uzawa's algorithm, which is based on a projection operator on a closed convex set. In the BM algorithm, the projector is substituted by a Yosida approximation, which can be applied in more general contexts. Indeed, when the functional $j(v)$ is the support function of a closed convex set, BM reduces to Uzawa's method.

Recall that ([ET99]):

$$\partial T(Z) = \{W \in \mathcal{H} \colon W(\mathbf{x}) \in \partial\Phi(\mathbf{x}, Z(\mathbf{x})) \text{ a.e. } \mathbf{x} \in \Omega\}. \tag{3.26}$$

The subdifferential of T can thus be computed pointwise in terms of the subdifferential of Φ. To this end, remember that we have defined the space $X = \mathbb{R}^{2\times 2}$ with scalar product $(p, q) = (p \colon q + \operatorname{tr}(p)\operatorname{tr}(q))$ and associated norm $\|\cdot\|$. Then, define $\phi \colon X \to \mathbb{R}$ as $\phi(p) = c\|p\|$, where c is an arbitrary constant. For $p \neq 0$, the function ϕ is Gâteaux differentiable, so the subdifferential $\partial\phi(p)$ consists only of the gradient:

$$\nabla_{\mathbf{x}}\phi(p) = c\frac{p}{\|p\|}.$$

On the other hand, one can see that

$$\partial\phi(0) = \{q \in X \colon \|q\| \leqslant c\}.$$

Finally, the Yosida approximation G_λ^ω can be computed as follows: for a.e. $\mathbf{x} \in \Omega$ and $Z \in \mathcal{H}$,

$$G_\lambda^\omega(Z)(\mathbf{x}) = \begin{cases} \dfrac{Z(\mathbf{x})}{\lambda} & \text{if } \|Z(\mathbf{x})\| \leqslant \lambda\sqrt{2}\tau_y H^n(\mathbf{x}), \\[2ex] \dfrac{\sqrt{2}\tau_y H^n(\mathbf{x}) - \omega\|Z(\mathbf{x})\|}{(1-\lambda\omega)\|Z(\mathbf{x})\|} Z(\mathbf{x}) & \text{if } \|Z(\mathbf{x})\| > \lambda\sqrt{2}\tau_y H^n(\mathbf{x}). \end{cases}$$

This expression can be regarded as a generalization of the formula obtained in the one-dimensional case. We notice that

$$\|Z(\mathbf{x})\| = \sqrt{Z(\mathbf{x}) \colon Z(\mathbf{x}) + \operatorname{tr}(Z(\mathbf{x}))^2}, \quad \text{a.e. } \mathbf{x} \in \Omega,$$

so the following relation holds:

$$\|Z\|_{\mathcal{H}} = \left(\int_\Omega \|Z(\mathbf{x})\|^2 d\mathbf{x}\right)^{1/2}.$$

We end this section by giving the explicit form of the linear problem to be solved at each iteration of (3.25). After integration by parts, it can be written as follows (and compared to (3.20)):

$$H^n\left(\frac{V^{k+1}-V^n}{\Delta t}\right)+\beta V^{k+1}-2\eta(\mathrm{div}_x(H^n D(V^{k+1}))$$
$$+\nabla_x(H^n\mathrm{div}_x(V^{k+1})))-\omega(\mathrm{div}_x(D(V^{k+1}))+\nabla_x(\mathrm{div}_x(V^{k+1})))$$
$$+H^n(V^n\cdot\nabla_x V^n)-(f_\Omega+f_z\,\nabla_x b)\,H^n-\nabla_x\left(\frac{(H^n)^2}{2}f_z\right)$$
$$-\mathrm{div}_x(\theta^k)-\nabla_x(\mathrm{tr}(\theta^k))=0. \qquad (3.27)$$

3.3.2.2 *Study of the optimal parameter*

The analysis on the optimal choice of parameters performed in [FGV14] can be adapted to the 2D case. First, let $\mathcal{V}_h$ be a finite-dimensional subspace of $\mathcal{V}$ of standard conforming $\mathbb{P}_1$ finite elements, being h the mesh size (dependence on h will be dropped unless necessary). Now, [FGV14, Equation (62)] and [FGV14, Equation (64)] read as

$$\langle A(V^k-V),\Psi\rangle+\omega\,(B(V^k-V),B(\Psi))_{\mathcal{H}}+(\theta^k-\theta,B(\Psi))_{\mathcal{H}}=0,\quad \forall\Psi\in\mathcal{V}_h, \qquad (3.28)$$

and

$$\|\theta^{k+1}-\theta\|^2_{\mathcal{H}}\leqslant\|\theta^k-\theta\|^2_{\mathcal{H}}-4\omega\langle A(V^k-V),V^k-V\rangle, \qquad (3.29)$$

respectively. Notice that the condition $\lambda\omega=1/2$ has been assumed.

Let now C_P and C_K be, respectively, the constants in the Poincaré and Korn inequalities (i.e., $\|\Psi\|_{L^2}\leqslant C_P\|\nabla\Psi\|_{L^2}$ and $\|\nabla\Psi\|_{L^2}\leqslant C_K\|D(\Psi)\|_{L^2}$, for every $\Psi\in\mathcal{V}_h$), and define $\gamma_1=C_P^{-1}C_K^{-1}$. Let γ_2 be such that $\|V\|_{\mathcal{V}}\leqslant\gamma_2\|V\|_{L^2}$ for every $V\in\mathcal{V}_h$. Then, equation (3.28) implies, for all $\Psi\in\mathcal{V}_h$,

$$(\theta^k-\theta,B(\Psi))_{\mathcal{H}}\leqslant\left(\frac{H^n_{\max}}{\Delta t}+\beta\right)\|V^k-V\|_{L^2}\|\Psi\|_{L^2}+(\omega+2\eta H^n_{\max})\|B(V^k-V)\|_{\mathcal{H}}\|B(\Psi)\|_{\mathcal{H}}$$
$$\leqslant\Gamma(\omega)\|V^k-V\|_{L^2}\|B(\Psi)\|_{\mathcal{H}},$$

where $H^n_{\max}=\|H^n\|_\infty$ and

$$\Gamma(\omega)=\left(\frac{H^n_{\max}}{\Delta t}+\beta\right)\gamma_1^{-1}+(\omega+2\eta H^n_{\max})\gamma_2.$$

Assuming that $\Psi\in\mathcal{V}_h$ is such that $B(\Psi)=\theta^k-\theta$, it follows that

$$\|\theta^k-\theta\|_{\mathcal{H}}\leqslant\Gamma(\omega)\|V^k-V\|_{L^2}.$$

Finally, using the inequality $\|V\|_{\mathcal{V}}\geqslant\gamma_1\|V\|_{L^2}$ and the coerciveness of A, from (3.29) we deduce that

$$\|\theta^{k+1}-\theta\|^2_{\mathcal{H}}\leqslant\mathcal{L}(\omega)\|\theta^k-\theta\|^2_{\mathcal{H}},$$

where

$$\mathcal{L}(\omega) = 1 - 4\omega\gamma\gamma_1^2\Gamma(\omega)^{-2}.$$

Minimization of $\mathcal{L}(\omega)$ leads to the following expression for the optimal parameter ω_{opt}:

$$\omega_{opt} = \gamma_1^{-1}\gamma_2^{-1}\left(\frac{H_{max}^n}{\Delta t} + \beta\right) + 2\eta H_{max}^n. \tag{3.30}$$

It only remains to estimate the constants γ_1 and γ_2. Following [KO88, Sect. 5.6], the Korn constant can be simply taken as $C_K = \sqrt{2}$. Assuming that the domain Ω is convex, it is known (see [PW60]) that the optimal choice for C_P is d/π, where d is the diameter of Ω. Thus, $\gamma_1 = \pi/\sqrt{2}d$. On the other hand, we have that $\|V\|_\mathcal{V} \leqslant \sqrt{3}\|\nabla V\|_{L^2} \leqslant \sqrt{3}\tilde{\gamma}_2\|V\|_{L^2}$ for a certain constant $\tilde{\gamma}_2$, so $\gamma_2 = \sqrt{3}\tilde{\gamma}_2$. Reasoning as in [FGV14, Appendix C], $\tilde{\gamma}_2$ can be taken as $\sqrt{\mu_{max}}$, where μ_{max} is the maximum eigenvalue of the discrete Laplacian problem; in general, this value has to be computed numerically.

Remark: In the particular case of a rectangle $\Omega = [x_{10}, x_{10} + L_{x_1}] \times [x_{20}, x_{20} + L_{x_2}]$ with a uniform discretization $(\Delta x_1, \Delta x_2)$, γ_1 would be

$$\gamma_1 = \frac{\pi}{\sqrt{2(L_{x_1}^2 + L_{x_2}^2)}},$$

while γ_2 could be taken as

$$\gamma_2 = \sqrt{3\pi^2\left(\frac{1}{\Delta x_1^2} + \frac{1}{\Delta x_2^2}\right)}.$$

Note that very recently the FISTA method [TMP16] was introduced for the simulation of viscoplastic flows. It is inspired by proximal gradient methods and allows to speed-up computations, compared to the non opimized augmented Lagrangian. FISTA could be a complementary approach to the present BM method which has an automatic computation of the optimal duality parameter while giving the same quality results of plastic zones, as the long proven AL method [SW17].

3.4 DISCRETIZATION IN SPACE AND WELL-BALANCING IN 2D

In this section, we define the spatial discretization for the conservation equation (3.14) and the velocity equation associated to the iterative algorithm of the AL (equation (3.20)) and the BM (equation (3.27)). As mentioned in the companion paper [FGV14] in 1D, there is a rather subtle coupling between both equations through the well-balanced property of the global scheme. This need to be carefully extended when going to the 2D framework.

3.4.1 *Definitions*

Note that both equations (3.20) and (3.27) can be written under the same structure. Namely, for a time $t = t^n$ and known the velocity at iteration n, V^n, the common system is

$$\begin{aligned} &H^n \frac{V^{k+1}}{\Delta t} + \beta V^{k+1} - \big(\mathrm{div}_x((2\eta H^n + \delta^n) D(V^{k+1})) \\ &+\nabla_x((2\eta H^n + \delta^n)\mathrm{div}_x(V^{k+1}))\big) = H^n \left(\frac{V^n}{\Delta t} - V^n \cdot \nabla_x V^n + (f_\Omega + f_z \, \nabla_x(b + H^n)) \right) \\ &+\mathrm{div}_x(H^n \Pi^k) + \nabla_x(\mathrm{tr}(H^n \Pi^k)), \end{aligned} \tag{3.31}$$

where:

- for the AL method:

$$\delta^n = r H^n, \quad \Pi^k = \mu^k - r q^k; \tag{3.32}$$

- for the BM method:

$$\delta^n = \omega^n, \quad \Pi^k = \theta^k / H^n, \tag{3.33}$$

  where ω^n is defined by the optimal value (3.30), in terms of H^n.

Let us suppose that the domain Ω is a rectangle, $\Omega = [x_{10}, x_{10} + L_{x_1}] \times [x_{20}, x_{20} + L_{x_2}]$. Let us consider a partition of N_{x_1} intervals of length $\Delta x_1 = L_{x_1}/N_{x_1}$ along x_1; and another partition with N_{x_2} intervals of length $\Delta x_2 = L_{x_2}/N_{x_2}$ along x_2. The 2D mesh is then defined by the union of control volumes

$$\{\mathcal{K}_{i,j}\}_{i=1,\dots,N_{x_1}}^{j=1,\dots,N_{x_2}}, \quad \text{where} \quad \mathcal{K}_{i,j} = [x_{1,i-1/2}, x_{1,i+1/2}] \times [x_{2,j-1/2}, x_{2,j+1/2}],$$

$$i = 1, \dots, N_{x_1}, \quad j = 1, \dots, N_{x_2},$$

with

$$x_{1,i+1/2} := x_{10} + i\,\Delta x_1, \qquad i = 0, \dots, N_{x_1},$$

$$x_{2,j+1/2} := x_{20} + j\,\Delta x_2, \qquad j = 0, \dots, N_{x_2}.$$

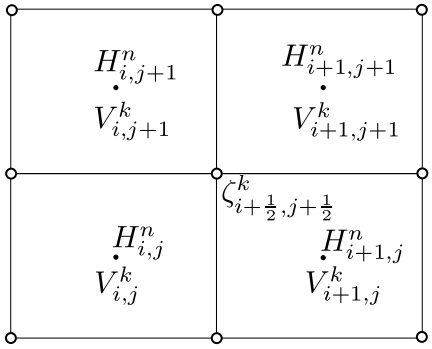

Figure 3.2: Notations for the discretization

To approximate H^n and V^k, solutions of the semi-discrete system defined by (3.14)-(3.31), we consider a finite-volume solver. Then, let us denote at $(x_{1,i}, x_{2,j})$, center of $\mathcal{K}_{i,j}$,

$$H^n_{i,j} \approx \frac{1}{|\mathcal{K}_{i,j}|}\int_{\mathcal{K}_{i,j}} H^n(\mathbf{x})d\mathbf{x}, \quad V^k_{i,j} \approx \frac{1}{|\mathcal{K}_{i,j}|}\int_{\mathcal{K}_{i,j}} V^k(\mathbf{x})d\mathbf{x}.$$

The *duality multiplier* Π^k is approximated at the vertices of the partition, then let us denote (see figure 3.2)

$$\Pi^k_{i+1/2,j+1/2} \approx \Pi^k(x_{1,i+1/2}, x_{2,j+1/2}).$$

By the definition of Π^k, equations (3.32)-(3.33), we denote

$$\Pi^k_{i+1/2,j+1/2} = \begin{cases} \mu^k_{i+1/2,j+1/2} - rq^k_{i+1/2,j+1/2}, & \text{for AL,} \\ \theta^k_{i+1/2,j+1/2}/H^n_{i+1/2,j+1/2}, & \text{for BM,} \end{cases}$$

and

$$H^n_{i+1/2,j+1/2} = (H^n_{i,j} + H^n_{i+1,j} + H^n_{i,j+1} + H^n_{i+1,j+1})/4. \tag{3.34}$$

In order to discretize in space the system (3.14)-(3.31), we consider a well-balanced finite volume method defined in terms of a diagonal viscosity matrix. This implies that we can present the discretization of the system equation by equation. Nevertheless, their discretizations are not really decoupled because, in order to obtain a well-balanced property, it is necessary to take into account the definition of the *duality multipliers* Π^k in the approximation of the mass conservation equation. Then, we first present the discretization of equation (3.31) and, second, the discretization of (3.14).

▷ *Discretization of the velocity equation (3.31) associated to the iterative algorithm*

Equation (3.31) is approximated as follows:

$$\left(\frac{H^n_{i,j}}{\Delta t}+\beta\right)V^{k+1}_{i,j}-\mathcal{D}^{k+1}_{i,j}=H^n_{i,j}\left(\frac{V^n_{i,j}}{\Delta t}-\frac{1}{\Delta x_1\Delta x_2}\left(\Delta x_2(\mathcal{F}^{n-}_{i+1/2,j}+\mathcal{F}^{n+}_{i-1/2,j})+\Delta x_1(\mathcal{F}^{n-}_{i,j+1/2}+\mathcal{F}^{n+}_{i,j-1/2})\right)\right)+\mathcal{E}^k_{i,j}, \quad (3.35)$$

where

$$\mathcal{F}^{n\pm}_{i+1/2,j}=\frac{(V_1)^n_{i,j}+(V_1)^n_{i+1,j}}{2}(V^n_{i+1,j}-V^n_{i,j})-f_\Omega\frac{\Delta x_1}{4}+\frac{f_z}{2}(b_{i+1,j}+H^n_{i+1,j}-b_{i,j}-H^n_{i,j})\begin{pmatrix}1\\0\end{pmatrix}\pm\frac{S_{i+1/2,j}}{2}(V^n_{i+1,j}-V^n_{i,j}),$$

$$\mathcal{F}^{n\pm}_{i,j+1/2}=\frac{(V_2)^n_{i,j}+(V_2)^n_{i,j+1}}{2}(V^n_{i,j+1}-V^n_{i,j})-f_\Omega\frac{\Delta x_2}{4}+\frac{f_z}{2}(b_{i,j+1}+H^n_{i,j+1}-b_{i,j}-H^n_{i,j})\begin{pmatrix}0\\1\end{pmatrix}\pm\frac{S_{i,j+1/2}}{2}(V^n_{i,j+1}-V^n_{i,j}),$$

being $S_{i+1/2,j}$ and $S_{i,j+1/2}$ the coefficients associated to a finite volume method discretizing the Saint-Venant system with a diagonal viscosity matrix. In this article, we use a Rusanov method, defined by:

$$S_{i+1/2,j}=\left|\frac{V^n_{i,j}+V^n_{i+1,j}}{2}\right|+\sqrt{|f_z|\,\frac{H^n_{i,j}+H^n_{i+1,j}}{2}},\quad S_{i,j+1/2}=\left|\frac{V^n_{i,j}+V^n_{i,j+1}}{2}\right|+\sqrt{|f_z|\,\frac{H^n_{i,j}+H^n_{i,j+1}}{2}}. \quad (3.36)$$

The term $\mathcal{E}^k_{i,j}=\mathcal{E}(\Pi^k_{i-1/2,j-1/2},\Pi^k_{i+1/2,j-1/2},\Pi^k_{i-1/2,j+1/2},\Pi^k_{i+1/2,j+1/2})$ is associated to the approximation of $\mathrm{div}_x(H^n\Pi^k)+\nabla_x(\mathrm{tr}(H^n\Pi^k))$, we set (denoting $[\cdot]_l$, the l-th component of a vector)

$$\begin{aligned}\left[\mathcal{E}^k_{i,j}\right]_1 &= \frac{H^n_{i+1/2,j}\left(2(\Pi_{11})^k_{i+1/2,j}+(\Pi_{22})^k_{i+1/2,j}\right)-H^n_{i-1/2,j}\left(2(\Pi_{11})^k_{i-1/2,j}-(\Pi_{22})^k_{i-1/2,j}\right)}{\Delta x_1}\\ &\quad+\frac{H^n_{i,j+1/2}(\Pi_{12})^k_{i,j+1/2}-H^n_{i,j-1/2}(\Pi_{12})^k_{i,j-1/2}}{\Delta x_2},\\ \left[\mathcal{E}^k_{i,j}\right]_2 &= \frac{H^n_{i,j+1/2}\left(2(\Pi_{22})^k_{i,j+1/2}+(\Pi_{11})^k_{i,j+1/2}\right)-H^n_{i,j-1/2}\left(2(\Pi_{22})^k_{i,j-1/2}-(\Pi_{11})^k_{i,j-1/2}\right)}{\Delta x_2}\\ &\quad+\frac{H^n_{i+1/2,j}(\Pi_{12})^k_{i+1/2,j}-H^n_{i-1/2,j}(\Pi_{12})^k_{i-1/2,j}}{\Delta x_1},\end{aligned} \quad (3.37)$$

where we have used the following notations:

$$H^n_{i+1/2,j}=\frac{H^n_{i,j}+H^n_{i+1,j}}{2},\qquad H^n_{i,j+1/2}=\frac{H^n_{i,j}+H^n_{i,j+1}}{2},$$

$$\Pi^k_{i+1/2,j}=\frac{\Pi^k_{i+1/2,j+1/2}+\Pi^k_{i+1/2,j-1/2}}{2},\qquad \Pi^k_{i,j+1/2}=\frac{\Pi^k_{i-1/2,j+1/2}+\Pi^k_{i+1/2,j+1/2}}{2}.$$

Finally, the term $\mathcal{D}_{i,j}^{k+1}$ is associated to the discretization of

$$\left(\mathrm{div}_{\mathbf{x}}((2\eta H^n + \delta^n)D(V^{k+1})) + \nabla_{\mathbf{x}}((2\eta H^n + \delta^n)\mathrm{div}_{\mathbf{x}}(V^{k+1}))\right).$$

Let us remark that several possibilities to define the term $\mathcal{D}_{i,j}^{k+1}$ can be considered. Nevertheless, it is necessary to consider a consistent approximation with definition (3.37), in order to improve the convergence of the iterative algorithm and the well-balanced property. The following definition is considered:

$$
\begin{aligned}
[\mathcal{D}_{i,j}^{k+1}]_1 = \; & 2\Big((2\eta H_{i+1/2,j}^n + \delta_{i+1/2,j}^n)\,\Delta_1(V_1^{k+1})|_{i+1/2,j} - (2\eta H_{i-1/2,j}^n + \delta_{i-1/2,j}^n)\,\Delta_1(V_1^{k+1})|_{i-1/2,j}\Big)/\Delta x_1^2 \\
& + \Big((2\eta H_{i,j+1/2}^n + \delta_{i,j+1/2}^n)\,\Delta_2(V_1^{k+1})|_{i,j+1/2} - (2\eta H_{i,j-1/2}^n + \delta_{i,j-1/2}^n)\,\Delta_2(V_1^{k+1})|_{i,j-1/2}\Big)/(2\Delta x_2^2) \\
& + \Big((2\eta H_{i+1/2,j}^n + \delta_{i+1/2,j}^n)\,\Delta_2(V_2^{k+1})|_{i+1/2,j} - (2\eta H_{i-1/2,j}^n + \delta_{i-1/2,j}^n)\,\Delta_2(V_2^{k+1})|_{i-1/2,j}\Big)/(\Delta x_1 \Delta x_2) \\
& + \Big((2\eta H_{i,j+1/2}^n + \delta_{i,j+1/2}^n)\,\Delta_1(V_2^{k+1})|_{i,j+1/2} - (2\eta H_{i,j-1/2}^n + \delta_{i,j-1/2}^n)\,\Delta_1(V_2^{k+1})|_{i,j-1/2}\Big)/(2\Delta x_1 \Delta x_2), \\
[\mathcal{D}_{i,j}^{k+1}]_2 = \; & 2\Big((2\eta H_{i,j+1/2}^n + \delta_{i,j+1/2}^n)\,\Delta_2(V_2^{k+1})|_{i,j+1/2} - (2\eta H_{i,j-1/2}^n + \delta_{i,j-1/2}^n)\,\Delta_2(V_2^{k+1})|_{i,j-1/2}\Big)/\Delta x_2^2 \\
& + \Big((2\eta H_{i+1/2,j}^n + \delta_{i+1/2,j}^n)\,\Delta_1(V_2^{k+1})|_{i+1/2,j} - (2\eta H_{i-1/2,j}^n + \delta_{i-1/2,j}^n)\,\Delta_1(V_2^{k+1})|_{i-1/2,j}\Big)/(2\Delta x_1^2) \\
& + \Big((2\eta H_{i+1/2,j}^n + \delta_{i+1/2,j}^n)\,\Delta_2(V_1^{k+1})|_{i+1/2,j} - (2\eta H_{i-1/2,j}^n + \delta_{i-1/2,j}^n)\,\Delta_2(V_1^{k+1})|_{i-1/2,j}\Big)/(2\Delta x_1 \Delta x_2) \\
& + \Big((2\eta H_{i,j+1/2}^n + \delta_{i,j+1/2}^n)\,\Delta_1(V_1^{k+1})|_{i,j+1/2} - (2\eta H_{i,j-1/2}^n + \delta_{i,j-1/2}^n)\,\Delta_1(V_1^{k+1})|_{i,j-1/2}\Big)/(\Delta x_1 \Delta x_2),
\end{aligned}
$$

where,

$$
\Delta_1(V_l)|_{i+1/2,j} = \tfrac{1}{4}\Big((V_l)_{i+1,j+1} + 2(V_l)_{i+1,j} + (V_l)_{i+1,j-1} - (V_l)_{i,j+1} - 2(V_l)_{i,j} - (V_l)_{i,j-1}\Big), \qquad l = 1, 2.
$$

$$
\Delta_2(V_l)|_{i+1/2,j} = \tfrac{1}{4}\Big((V_l)_{i,j+1} + (V_l)_{i+1,j+1} - (V_l)_{i,j-1} - (V_l)_{i+1,j-1}\Big),
$$

$$
\Delta_1(V_l)|_{i,j+1/2} = \tfrac{1}{4}\Big((V_l)_{i+1,j+1} + (V_l)_{i+1,j} - (V_l)_{i-1,j+1} - (V_l)_{i-1,j}\Big),
$$

$$
\Delta_2(V_l)|_{i,j+1/2} = \tfrac{1}{4}\Big((V_l)_{i+1,j+1} + 2(V_l)_{i,j+1} + (V_l)_{i-1,j+1} - (V_l)_{i+1,j} - 2(V_l)_{i,j} - (V_l)_{i-1,j}\Big).
$$

Let us denote by $\mathcal{V}^k$ the vector of components $\mathcal{V}_l^k$, for $l = 1, \ldots, 2N_{x_1}N_{x_2}$. Being $(V_1)_{i,j}^k = \mathcal{V}_{2(i+(j-1)N_{x_1})-1}^k$ and $(V_2)_{i,j}^k = \mathcal{V}_{2(i+(j-1)N_{x_1})}^k$, where $V_{i,j}^k = ((V_1)_{i,j}^k, (V_2)_{i,j}^k)$, for $i = 1, \ldots, N_{x_1}$ and $j = 1, \ldots, N_{x_2}$. Then, to obtain the values of $\mathcal{V}^{k+1}$, it is necessary to solve the linear system defined by equations (3.35) for $i = 1, \ldots, N_{x_1}$ and $j = 1, \ldots, N_{x_2}$.

▷ *Well-balanced discretization of the mass conservation equation (3.14)*

Before to consider the updating of the mass conservation equation, we must previously compute the velocity approximation $\{V_{i,j}^{n+1}\}_{i=1,\ldots,N_{x_1}}^{j=1,\ldots,N_{x_2}}$ by the iterative algorithm corresponding to the AL or the BM method. In particular, when the iterative algorithm has converged, this also gives the value of multipliers $\{\Pi_{i+1/2,j+1/2}^{\bar{k}}\}_{i=0,\ldots,N_{x_1}}^{j=0,\ldots,N_{x_2}}$, being $\bar{k}$ the last iteration of the algorithm.

We consider the following well-balanced finite-volume discretization:

$$
H_{i,j}^{n+1} = H_{i,j}^n - \frac{\Delta t}{\Delta x_1}(\phi_{i+1/2,j}^n - \phi_{i-1/2,j}^n) - \frac{\Delta t}{\Delta x_2}(\phi_{i,j+1/2}^n - \phi_{i,j-1/2}^n),
$$

(3.38)

where

$$\phi^n_{i+1/2,j} = \frac{H^n_{i+1,j}V^n_{i+1,j} + H^n_{i,j}V^n_{i,j}}{2} - \frac{1}{2}S_{i+1/2,j}(H^n_{i+1,j} - H^n_{i,j} - \mathcal{G}^n_{i+1/2,j}), \tag{3.39}$$

and analogously

$$\phi^n_{i,j+1/2} = \frac{H^n_{i,j+1}V^n_{i,j+1} + H^n_{i,j}V^n_{i,j}}{2} - \frac{1}{2}S_{i,j+1/2}(H^n_{i,j+1} - H^n_{i,j} - \mathcal{G}^n_{i,j+1/2}). \tag{3.40}$$

For (3.38)-(3.40) to be well-balanced (as proved in section 3.4.3), the key point is to build in $\mathcal{G}^n_{\cdot,\cdot}$ a discrete approximation of the $\mathrm{div}_x(.) + \nabla_x(\mathrm{tr}(.))$ operator acting on the duality corrector $\Pi^{\bar{k}} + D(V^{\bar{k}})$. This follows the insight of the 1D study (see [FGV14]) but the construction is more intricate. We introduce progressively the following quantities, computed from the available discrete variables. First, we define:

$$(\xi_{11})^k_{i+1/2,j+1/2} := (\Pi_{11})^k_{i+1/2,j+1/2} + \frac{\delta^k_{i+1/2,j+1/2}}{2H^n_{i+1/2,j+1/2}\Delta x_1}[V^{n+1}_{i+1,j+1} + V^{n+1}_{i+1,j} - V^{n+1}_{i,j+1} - V^{n+1}_{i,j}]_1, \tag{3.41}$$

$$(\xi_{22})^k_{i+1/2,j+1/2} := (\Pi_{22})^k_{i+1/2,j+1/2} + \frac{\delta^k_{i+1/2,j+1/2}}{2H^n_{i+1/2,j+1/2}\Delta x_2}[V^{n+1}_{i,j+1} + V^{n+1}_{i+1,j+1} - V^{n+1}_{i,j} - V^{n+1}_{i+1,j}]_2, \tag{3.42}$$

$$(\xi_{12})^k_{i+1/2,j+1/2} := (\Pi_{12})^k_{i+1/2,j+1/2} + \frac{\delta^k_{i+1/2,j+1/2}}{4H^n_{i+1/2,j+1/2}} \times \left(\frac{[V^{n+1}_{i+1,j+1} + V^{n+1}_{i+1,j} - V^{n+1}_{i,j+1} - V^{n+1}_{i,j}]_2}{\Delta x_1} + \frac{[V^{n+1}_{i,j+1} + V^{n+1}_{i+1,j+1} - V^{n+1}_{i,j} - V^{n+1}_{i+1,j}]_1}{\Delta x_2} \right), \tag{3.43}$$

where, following (3.32)-(3.33) and using (3.34), we set

$$\delta^k_{i+1/2,j+1/2} := \begin{cases} rH^n_{i+1/2,j+1/2} & \text{for AL,} \\ \omega^n = \omega_{opt}(H^n_{i+1/2,j+1/2}) & \text{for BM.} \end{cases}$$

Then, we compute these quantities at the center of the edges of control volumes (where the flux is needed). For $l \in 1,2$ we denote

$$(\xi_{ll})^k_{i+1/2,j} = \frac{(\xi_{ll})^k_{i+1/2,j+1/2} + (\xi_{ll})^k_{i+1/2,j-1/2}}{2},$$

$$(\xi_{ll})^k_{i,j+1/2} = \frac{(\xi_{ll})^k_{i+1/2,j+1/2} + (\xi_{ll})^k_{i-1/2,j+1/2}}{2}.$$

Let us also denote by η the free surface level computed from the reference plane,

$$\eta^n_{i,j} = b_{i,j} + H^n_{i,j} := b(\mathbf{x}_{i,j}) + H^n_{i,j}.$$

We are now able to write our definition of the correction terms $\mathcal{G}^n_{i+1/2,j}$ and $\mathcal{G}^n_{i,j+1/2}$, in terms of the aforementioned quantities:

$$\begin{aligned}\mathcal{G}^n_{i+1/2,j} = {} & \tfrac{[f_\Omega]_1}{f_z}\Delta x_1 + (b_{i+1,j} - b_{i,j}) + \tfrac{1}{H^n_{i+1/2,j} f_z}\left(H^n_{i+1/2,j+1/2}(\xi_{12})^{\bar{k}}_{i+1/2,j+1/2} - H^n_{i+1/2,j-1/2}(\xi_{12})^{\bar{k}}_{i+1/2,j-1/2}\right)\tfrac{\Delta x_1}{\Delta x_2} \\ & + \mathcal{Z}\Big(H^n_{i-1/2,j}\left(2(\xi_{11})^{\bar{k}}_{i-1/2,j} + (\xi_{22})^{\bar{k}}_{i-1/2,j}\right), H^n_{i+1/2,j}\left(2(\xi_{11})^{\bar{k}}_{i+1/2,j} + (\xi_{22})^{\bar{k}}_{i+1/2,j}\right), \\ & \quad H^n_{i+3/2,j}\left(2(\xi_{11})^{\bar{k}}_{i+3/2,j} + (\xi_{22})^{\bar{k}}_{i+3/2,j}\right), \eta^n_{i-1,j}, \eta^n_{i,j}, \eta^n_{i+1,j}, \eta^n_{i+2,j}\Big)\tfrac{1}{H^n_{i+1/2,j} f_z},\end{aligned}$$

$$\begin{aligned}\mathcal{G}^n_{i,j+1/2} = {} & \tfrac{[f_\Omega]_2}{f_z}\Delta x_2 + (b_{i,j+1} - b_{i,j}) + \tfrac{1}{H^n_{i,j+1/2} f_z}\left(H^n_{i+1/2,j+1/2}(\xi_{12})^{\bar{k}}_{i+1/2,j+1/2} - H^n_{i-1/2,j+1/2}(\xi_{12})^{\bar{k}}_{i-1/2,j+1/2}\right)\tfrac{\Delta x_2}{\Delta x_1} \\ & + \mathcal{Z}\Big(H^n_{i,j-1/2}\left((\xi_{11})^{\bar{k}}_{i,j-1/2} + 2(\xi_{22})^{\bar{k}}_{i,j-1/2}\right), H^n_{i,j+1/2}\left((\xi_{11})^{\bar{k}}_{i,j+1/2} + 2(\xi_{22})^{\bar{k}}_{i,j+1/2}\right), \\ & \quad H^n_{i,j+3/2}\left((\xi_{11})^{\bar{k}}_{i,j+3/2} + 2(\xi_{22})^{\bar{k}}_{i,j+3/2}\right), \eta^n_{i,j-1}, \eta^n_{i,j}, \eta^n_{i,j+1}, \eta^n_{i,j+2}\Big)\tfrac{1}{H^n_{i,j+1/2} f_z},\end{aligned}$$

where again $[\cdot]_l$ is the l-th component of a vector.
To define $\mathcal{Z}$, we use a combination of a second order approximation and a first order upwind approximation via a flux limiter, (see [FGV14]):

$$\mathcal{Z}(d_l, d_c, d_r, s_{-1}, s_0, s_1, s_2) = \chi\,\frac{d_r - d_l}{2} + (1-\chi)\overline{\Delta d}_1, \tag{3.44}$$

with

$$\overline{\Delta d}_1 = \begin{cases} d_c - d_l & \text{if } s_0 < s_1, \\ d_r - d_c & \text{if } s_0 > s_1, \\ (d_r - d_l)/2 & \text{if } s_0 = s_1. \end{cases}$$

This definition of $\mathcal{Z}$ introduces an upwinding in the discretization of the normal (to the edge of the control volume) variation of the multiplier Π, in the cases of high variations of the free surface. Note that the variations of the multiplier are also related to the pressure gradient, and as a consequence to the free surface. If in the numerical tests we do not have high gradients of the free surface a simple centered difference could be used, as:

$$\mathcal{Z}(d_l, d_c, d_r, s_{-1}, s_0, s_1, s_2) = \frac{d_r - d_l}{2}.$$

The term $\chi = \chi(\nu(s_{-1}, s_0, s_1, s_2))$ is a flux limiter function with $\nu(s_{-1}, s_0, s_1, s_2) \in [0, 1]$,

$$\nu = \max(0, \min(1, \tilde{\nu})), \qquad \tilde{\nu} = \begin{cases} \frac{3(s_0 - s_{-1})}{s_2 - s_{-1}}, & \text{if } s_1 > s_0, \\ \frac{3(s_2 - s_1)}{s_2 - s_{-1}}, & \text{if } s_1 < s_0, \\ 1 & \text{if } s_1 = s_0 \text{ or } s_2 = s_{-1}. \end{cases}$$

In [FGV14] has been proposed the following definition of the flux limiter:

$$\chi(\nu) = 1 - (1 - \nu^{1/4})^4.$$

Remark: The terms $(\xi_{lm})^k_{i+1/2,j+1/2}$, $l, m = 1, 2$, defined by (3.41)-(3.43), have been considered only in the evaluation of the correction terms $\mathcal{G}^n_{i+1/2,j}$ and $\mathcal{G}^n_{i,j+1/2}$. These terms allow us to obtain a scheme verifying the well-balanced properties described in Theorem 1.

Let us remark that we can obtain the same well-balanced properties of the schemes if we set $(\xi_{lm})^k_{i+1/2,j+1/2} = (\Pi_{lm})^k_{i+1/2,j+1/2}$. That is, if we neglect the terms depending on the velocity in the definitions (3.41)-(3.43). Nevertheless, these terms are necessary for stability purposes. If we do not include these terms then the CFL condition depends on the parameter of the duality method: the CFL being more restrictive for bigger values of $\{r, \omega\}$.

The correction terms $\mathcal{G}^n_{i+1/2,j}$ and $\mathcal{G}^n_{i,j+1/2}$ are defined as the sum of four terms. The first one takes into account the slope of the reference plane; the second one, the slope of the local topography; the third one, the tangential variation of the multiplier Π on the edge. And the last one, the normal variation to the edge of the multiplier. Note that to preserve general 2D stationary solutions is extremely more complicated than in the 1D case. The proposed definition of the third and fourth terms allows to preserve stationary solutions with a general shape of the free surface with good accuracy (as shown in the numerical tests).

Remark: On the treatment of wet/dry fronts. It is actually done as the natural extension in 2D of the treatments proposed in the companion paper [FGV14]. For sake of brevity, they are not redescribed here.

3.4.2 *The global coupled scheme*

Capitalizing on the previous sections, the description of the global coupled scheme for (3.14)-(3.15) can be described in a few words. This global structure is actually the same as for the 1D case [FGV14].

Only the update of the duality variable is more involved due to the tensorial nature of $D(V)$; however, the "dual" localization of V (at $(x_{1,i}, x_{2,j})$) and the duality variables (at $(x_{1,i+1/2}, x_{2,j+1/2})$) allows to compute the gradient in a natural way with centered differentiation. In brief, the global scheme for both AL and BM is the following:

- Initialization at time $t = 0$, $n = 0$, V^n and H^n are given by the initial conditions
- Time loop:
  - Resolution of V^{n+1}:
    - Initialization of the duality loop
    - Duality loop:
      - Resolution of V^{k+1}: this is a linear system coming from the discretization presented in the previous section
      - Update of the duality multipliers. A discretization is needed for equations (3.19), (3.21) for the AL method and for the second equation of (3.25) for the BM method. In order to discretize these equations, we just need to specify $B(V^k)|_{i+1/2,j+1/2}$, approximation of $B(V^k)|_{(x_{1,i+1/2},x_{2,j+1/2})}$. We consider the following discretization for the three components of this symmetric tensor:

$$\left[B(V^k)|_{i+1/2,j+1/2}\right]_{11} = \frac{1}{2\Delta x_1}\left[V^k_{i+1,j+1} + V^k_{i+1,j} - V^k_{i,j+1} - V^k_{i,j}\right]_1,$$

$$\left[B(V^k)|_{i+1/2,j+1/2}\right]_{12} = \frac{1}{4\Delta x_1}\left[V^k_{i+1,j+1} + V^k_{i+1,j} - V^k_{i,j+1} - V^k_{i,j}\right]_2 + \frac{1}{4\Delta x_2}\left[V^k_{i,j+1} + V^k_{i+1,j+1} - V^k_{i,j} - V^k_{i+1,j}\right]_1,$$

$$\left[B(V^k)|_{i+1/2,j+1/2}\right]_{22} = \frac{1}{2\Delta x_2}\left[V^k_{i,j+1} + V^k_{i+1,j+1} - V^k_{i,j} - V^k_{i+1,j}\right]_2,$$

    - At convergence: $V^{n+1} \leftarrow V^{k+1}$
  - Resolution of H^{n+1}: it is an explicit computation using the discretization presented in the previous section and using the last duality multiplier coming from the computation of V^{n+1} just above.

3.4.3 *Well-balanced properties*

Theorem 1
Let us consider the following initialization of the components of $\{(\Pi^0)_{i+1/2,j+1/2}\}_{i=0,\dots,N_{x_1}}^{j=0,\dots,N_{x_2}}$,

$$(\Pi^0_{11})_{i+1/2,j+1/2} = -2(\Pi^0_{22})_{i+1/2,j+1/2}, \qquad (\Pi^0_{12})_{i+1/2,j+1/2} = 0,$$

(3.45)

and $(\Pi^0_{22})_{i+1/2,j+1/2}$ is defined recursively as follows:

• for $j = 0$: $i \in \{0, \dots, N_{x_1}\}$

$$(\Pi^0_{22})_{i+1/2,1/2} = \left([f_\Omega]_1 \Delta x_1 + f_z(b_{i+1,1} + H^0_{i+1,1} - b_{i,1} - H^0_{i,1})\right) \frac{1}{3H^0_{i+1/2,1}} \left(\sum_{k=1}^{i} H^0_{k,1} - C\right),$$

• for $j = 1, \dots, N_{x_2}$: $i \in \{0, \dots, N_{x_1}\}$

$$(\Pi^0_{22})_{i+1/2,j+1/2} = \left([f_\Omega]_1 \Delta x_1 + f_z(b_{i+1,j+1/2} + H^0_{i+1,j+1/2} - b_{i,j+1/2} - H^0_{i,j+1/2})\right)$$
$$\times \frac{2}{3H^0_{i+1/2,j}} \left(\sum_{k=1}^{i} H^0_{k,j} - C\right) - (\Pi^0_{22})_{i+1/2,j-1/2}, \tag{3.46}$$

for any constant C. Particularly, we can set $C = \sum_{i=1,N_{x_1}/2}^{j=1,N_{x_2}/2} H^0_{i,j}$.

The proposed scheme verifies that if we set this initial value: $(\Pi)^0_{i+1/2,j+1/2} = (\Pi^0)_{i+1/2,j+1/2}$ ($\forall\, i, j$), then it preserves exactly two kinds of solutions at rest:

(i) Material at rest with *horizontal free surface*, defined by the initial conditions:

$$V^0_{i,j} = 0, \quad (x_1)_{i,j} \sin\alpha + (b_{i,j} + H^0_{i,j}) \cos\alpha = \eta,$$

being η a constant value, corresponding to the level of the free surface.

(ii) Material at rest with *free surface parallel to the plane of reference*, defined by the initial conditions:

$$V^0_{i,j} = 0, \quad b_{i,j} + H^0_{i,j} = c, \tag{3.47}$$

begin c a constant value —the distance from the free surface to the plane of reference—, if the material is rigid enough, i.e. if τ_y verifies:

$$\|\Pi^0_{i+1/2,j+1/2}\| \leqslant \sqrt{2}\tau_y \quad \forall\, i, j. \tag{3.48}$$

Proof

(i) In this case, the initialization of the multipliers is zero, then it is equivalent to prove that the proposed finite volume method preserves exactly water at rest, which is a classical result and can be proven easily. So, for the purpose of brevity we omit the details.
(ii) In this case, let us divide the proof into two steps: to prove that

the velocity remains null and that the height does not change in the time loop.

[Step 1] Let us prove that the velocity remains zero.

First, note that, by (3.19)-(3.21) and (3.25), condition (3.48) implies that in both cases, for AL and BM methods, the given initialization of the multipliers remains constant in the iterative process. That is,

$$\Pi^k_{i+1/2,j+1/2} = \Pi^0_{i+1/2,j+1/2}, \forall k.$$

As $V^k_{i,j} = 0$ is the solution of the linear system defined by (3.35), it is enough to prove that the right hand side of the linear system is null. By using that the initial condition verifies (3.47), the right hand side of the linear system is:

$$f_\Omega H^0_{i,j} + \mathcal{E}^k_{i,j}.$$

Where, by (3.37), (3.35) and using (3.45), we have:

$$\mathcal{E}^k_{i,j} = \begin{pmatrix} -3\dfrac{H^0_{i+1/2,j}(\Pi_{22})^k_{i+1/2,j} - H^0_{i-1/2,j}(\Pi_{22})^k_{i-1/2,j}}{\Delta x_1} \\ \\ 0 \end{pmatrix}, \quad (3.49)$$

By using (3.46), and that $b_{i,j} + H^n_{i,j} = c$, we obtain

$$\begin{aligned}(\Pi_{22})^k_{i+1/2,j} = (\Pi_{22})^0_{i+1/2,j} &= \frac{(\Pi_{22})^0_{i+1/2,j+1/2} + (\Pi_{22})^0_{i+1/2,j-1/2}}{2} \\ &= [f_\Omega]_1 \Delta x_1 \frac{2}{3H^0_{i+1/2,j}} \left(\sum_{k=1}^{i} H^n_{k,j} - C \right). \quad (3.50)\end{aligned}$$

Then,

$$-3\frac{H^0_{i+1/2,j}(\Pi_{22})^k_{i+1/2,j} - H^0_{i-1/2,j}(\Pi_{22})^k_{i-1/2,j}}{\Delta x_1} = -H^0_{i,j}[f_\Omega]_1.$$

and, as a consequence, we obtain

$$f_\Omega H^0_{i,j} + \mathcal{E}^k_{i,j} = 0.$$

[Step 2] Finally, we prove that the height remains constant. By (3.38)-(3.40), it is enough to prove that the terms multiplying the numerical viscosity coefficients $S_{i+1/2,j}$ and $S_{i,j+1/2}$ are zero, i.e. to prove:

$$H^0_{i+1,j} - H^0_{i,j} - \mathcal{G}^n_{i+1/2,j} = 0, \qquad \text{and} \qquad H^0_{i,j+1} - H^0_{i,j} - \mathcal{G}^0_{i,j+1/2} = 0.$$

First, by using (3.45) and that the stationary solution verifies $b_{i,j} + H^0_{i,j} = c$, we obtain

$$\begin{aligned}&H^0_{i+1,j} - H^0_{i,j} - \mathcal{G}^0_{i+1/2,j} = \frac{[f_\Omega]_1}{f_z}\Delta x_1 + \frac{1}{f_z H_{i+1/2,j}} \times \\ &\mathcal{Z}\Big(-3H^0_{i-1/2,j}(\xi_{22})^0_{i-1/2,j}, -3H^0_{i+1/2,j}(\xi_{22})^0_{i+1/2,j}, -3H^0_{i+3/2,j}(\xi_{22})^0_{i+3/2,j}, c, c, c, c \Big). \quad (3.51)\end{aligned}$$

Moreover, if we consider a centered approximation of $\mathcal{Z}$ or definition (3.44), we obtain

$$\mathcal{Z}\Big(-3H^0_{i-1/2,j}(\xi_{22})^0_{i-1/2,j}, -3H^0_{i+1/2,j}(\xi_{22})^0_{i+1/2,j}, -3H^0_{i+3/2,j}(\xi_{22})^0_{i+3/2,j}, c, c, c, c\Big)$$
$$= \frac{-3H^0_{i+3/2,j}(\xi_{22})^0_{i+3/2,j} + 3H^0_{i-1/2,j}(\xi_{22})^0_{i-1/2,j}}{2}.$$

As the velocity is zero, we obtain

$$(\xi_{22})^0_{i+1/2,j} = (\Pi_{22})^0_{i-1/2,j}, \quad \forall i, j$$

Then, using (3.50), we obtain

$$H^0_{i+1/2,j}(\xi_{22})^0_{i+1/2,j} = [f_\Omega]_1 \Delta x_1 \frac{2}{3}\left(\sum_{k=1}^{i} H^0_{k,j} - C\right).$$

As a consequence,

$$\frac{-3H^0_{i+3/2,j}(\xi_{22})^0_{i+3/2,j} + 3H^0_{i-1/2,j}(\xi_{22})^0_{i-1/2,j}}{2} = -[f_\Omega]_1 \Delta x_1 H_{i+1/2,j}.$$

Then, by using (3.51),

$$H^n_{i+1,j} - H^n_{i,j} - \mathcal{G}^n_{i+1/2,j} = 0.$$

Secondly, by using also (3.45) and that the stationary solution verifies $b_{i,j} + H^n_{i,j} = c$, we obtain

$$H^n_{i,j+1} - H^n_{i,j} - \mathcal{G}^n_{i,j+1/2} = \frac{[f_\Omega]_2}{f_z}\Delta x_2 + \frac{1}{f_z H_{i,j+1/2}}\mathcal{Z}\Big(0, 0, 0, c, c, c, c\Big). \tag{3.52}$$

As $\mathcal{Z}\Big(0, 0, 0, c, c, c, c\Big) = 0$ and $[f_\Omega]_2 = 0$, then,

$$H^n_{i,j+1} - H^n_{i,j} - \mathcal{G}^n_{i,j+1/2} = 0,$$

which concludes the proof.

3.5 NUMERICAL TESTS

3.5.1 *The Couette-Bingham flow*

We aim at evaluating the performance of our schemes with respect to the viscoplastic features of the model. We use a test inspired by the classical (Newtonian) Couette flow between two concentric rotating cylinders. From the numerical viewpoint this is a full 2D test. But thanks to the axisymmetric geometry, we can derive an analytic solution defined in 1D, in polar coordinates (r, θ). We then have a useful non-trivial test to check the precision of our implementation of the duality methods, in a 2D space configuration.

The so-called Couette-Bingham problem consists in writing the Stokes equation between two concentric rotating cylinders (see the first plot of Figure 3.3) but using the Bingham law instead of the original Newtonian law. The problem is the following. Assume that a viscoplastic material of viscosity η and yield stress τ_y is between the two cylinders which are rotating at velocity v_i at $r = r_i$ (resp v_e at $r = r_e$) for the inner (resp. external) cylinder. Momentum conservation equations reads (in Cartesian coordinates as in the main text):

$$-\mathrm{div}_x(\sigma) = 0 \text{ with} \tag{3.53}$$

$$\begin{cases} \sigma = 2\eta D(V) + \sqrt{2}\tau_y \frac{D(V)}{|D(V)|} \text{ if } D(V) \neq 0 \\ |\sigma| \leqslant \sqrt{2}\tau_y \text{ if } D(V) = 0, \end{cases} \tag{3.54}$$

where $D(V) = \frac{1}{2}\left(\nabla V + (\nabla V)^T\right)$. There is no body force but the motion of cylinders leads to a shear-driven flow. In cylindrical coordinates, we can look for a velocity $V = v(r)\mathbf{e}_\theta$. As a matter of fact, the model of the main text degenerates to this problem when $H \equiv 1$, $f = 0$, friction, body force and non-linear convective terms are cancelled. Under such assumptions, when $t \to +\infty$, the solution of the main model converges to the solution of (3.53)-(3.54). The derivation of the analytic solution was initially performed by Reiner and Riwlin [RR27] (with only one non-zero velocity for the two cylinders) and various formulations can be found in other more recent articles like [Pia79], [LFM06] and [LV04]. We propose here a more general algorithm to compute the (semi)analytic solution, formulated independently from the torque. This formulation is useful as a test-case for 2D viscoplastic codes with velocities given as boundary conditions.

Algorithm: Couette-Bingham flow
Input data. Geometry: r_i, r_e. Fluid properties: η, τ_y. Boundary conditions: v_i, v_e.
Step 1. Check if we are in the case of a solid body rotation or not by comparing $\frac{v_i}{r_i}$ and $\frac{v_e}{r_e}$.

- If $\frac{v_i}{r_i} = \frac{v_e}{r_e} =: \varpi$, this is a solid body rotation. All the material is unyielded and $\forall r \in [r_i, r_e]$, $v(r) = r\varpi$. The problem is fully solved.
- If $\frac{v_i}{r_i} < \frac{v_e}{r_e}$ then the stress will be **positive**; let $sg = 1$ and go to Step 2.
- If $\frac{v_i}{r_i} > \frac{v_e}{r_e}$ then the stress will be **negative**; let $sg = -1$ and go to Step 2.

Step 2. As expected in this kind of problem, when the material is not fully unyielded, we need to determine if there is a "plug" zone in the domain $[r_i, r_e]$. To do so, it is sufficient to solve numerically the following problem for $r_y > r_i$:

$$\frac{2\eta}{\tau_y}\left|\frac{v_e}{r_e} - \frac{v_i}{r_i}\right| = \left(\frac{r_y}{r_i}\right)^2 - 2\ln\left(\frac{r_y}{r_i}\right) - 1. \tag{3.55}$$

Step 3. Two situations may occur:

- If $r_y \in]r_i, r_e[$, then there is a plug zone on $[r_y, r_e]$ (on the side of the external cylinder) where $v(r) = r\frac{v_e}{r_e}$ and a yielded zone on $[r_i, r_y]$ with $v(r)$ given by (3.57) and the following definition of the velocity at $r = r_y$:

$$v_y := \frac{v_e}{r_e} r_y. \tag{3.56}$$

- If $r_y \geqslant r_e$, then the material is completely yielded (*i.e.* there is no plug zone) and the velocity is given by (3.57) in which (r_y, v_y) needs naturally to be replaced by (r_e, v_e):

$$\begin{aligned} v(r) \;=\; & \underbrace{\frac{v_y r_y}{r(r_y^2 - r_i^2)}\left(\left[1 - \frac{r_i v_i}{r_y v_y}\right] r^2 + \left[\frac{r_y v_i}{r_i v_y} - 1\right] r_i^2\right)}_{\text{Newtonian part}} \\ & + sg\,\underbrace{\frac{2\tau_y}{\eta}\,\frac{r_y^2(r^2 - r_i^2)\ln\left(\frac{r_y}{r_i}\right) - r^2(r_y^2 - r_i^2)\ln\left(\frac{r}{r_i}\right)}{r(r_y^2 - r_i^2)}}_{\text{"Plastic correction"}}. \end{aligned} \tag{3.57}$$

This ends the resolution of the velocity of (3.53)-(3.54).

Numerical results
In Figure 3.3, we present the flow computed with our implementation for $r_i = 0.3$, $r_e = 2.0$, $v_i = 1.5$, $v_e = 2.1$, and a material such that

$\eta = \sqrt{2}$ and $\tau_y = \sqrt{2}/2$. Note that in this case, there exist both a fluid zone (yielded) and a plastic zone (unyielded) in the computation domain whose interface is at $r = r_y = 1.3344$. The discretization is done with a regular 400×400 grid. The numerical and the analytic solutions are superposed, validating our implementation of the computation of plastic and fluid zones. We also performed a grid refinement study showing a convergence in L^2-norm of the computed solution towards the exact solution. It must but noted that this test case has the numerical difficulty of being posed in a cylindrical geometry which can be handled by our Cartesian implementation (thanks to a direct penalization technique with an imposed velocity for all points outside the torus) but not with the optimal order of convergence (actually we loose one order in convergence magnitude) due to the inaccuracy of the Cartesian geometry to handle curved boundaries. This is a well known fact (see e.g. [SW38; YM15]) and one can adopt a more adapted space discretization to deal with general curved boundaries, as proposed for instance in [VBL04] (see also [LV04]). Since this is not the main objective of the present paper, we do not perform such an implementation. The main point in this section is that our scheme is convergent to the 2D analytic solution. Note that for the other tests of the paper, we use square computation domains for which we recover full accuracy of the scheme as it can be seen in the main text.
Let us now describe in more details the various results of Figure 3.3. The first plot illustrates the full 2D computation domain and show the numerical velocity field in the torus associated to (r_i, r_e): we can verify that the computed vector field is as expected by the analytic solution, rotationally symmetrical (independent on the angular variable θ). The colormap shows that, on a given azimuth θ from r_i to r_e, the velocity magnitude (in absolute value) is decreasing (dark brown to light brown) then increasing (light brown to black). This velocity magnitude is quantitatively described in the two following plots. Namely, the second plot gives, in Cartesian coordinates, the values of the y component of the velocity, namely $u_y(x, y)$, on the torus. Finally the third plot, in 1D, gives the slice of the previous u_y on the axis $y = 0$ ($u_y(x, 0)$) and from $x = r_i$ to $x = r_e$ (from $x = -r_i$ to $x = -r_e$, u_y is antisymmetric and is thus not shown). Recall that here, we have $u_x(x, y) = 0$, for the first component of the velocity. There are three types of information in this plot:

- the black thick line is the exact solution (3.57);
- the colored thin lines (starting from the null function in blue) are some of the computed u_y during the duality loop: they are converging to the exact solution as expected by the theory (note, as said above, that this fact is also true on the whole 2D domain, not only on the axis $y = 0$ which is shown for ease of visibility);

- the red dashed cross is the localization of the fluid/plastic transition at $x = r_y$, with a speed $u_y(r_y, 0) = v_y = 1.4011$ given by (3.56). It can be seen that for $x \in [r_y, r_e]$, $u_y(x, 0)$ is linear and the material moves with a solid body rotation.

Figure 3.3 is split on these two pages.

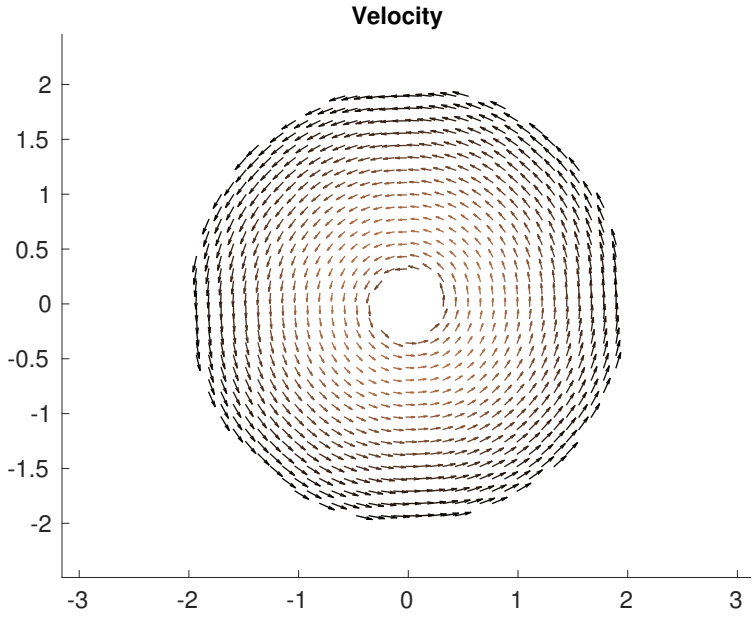

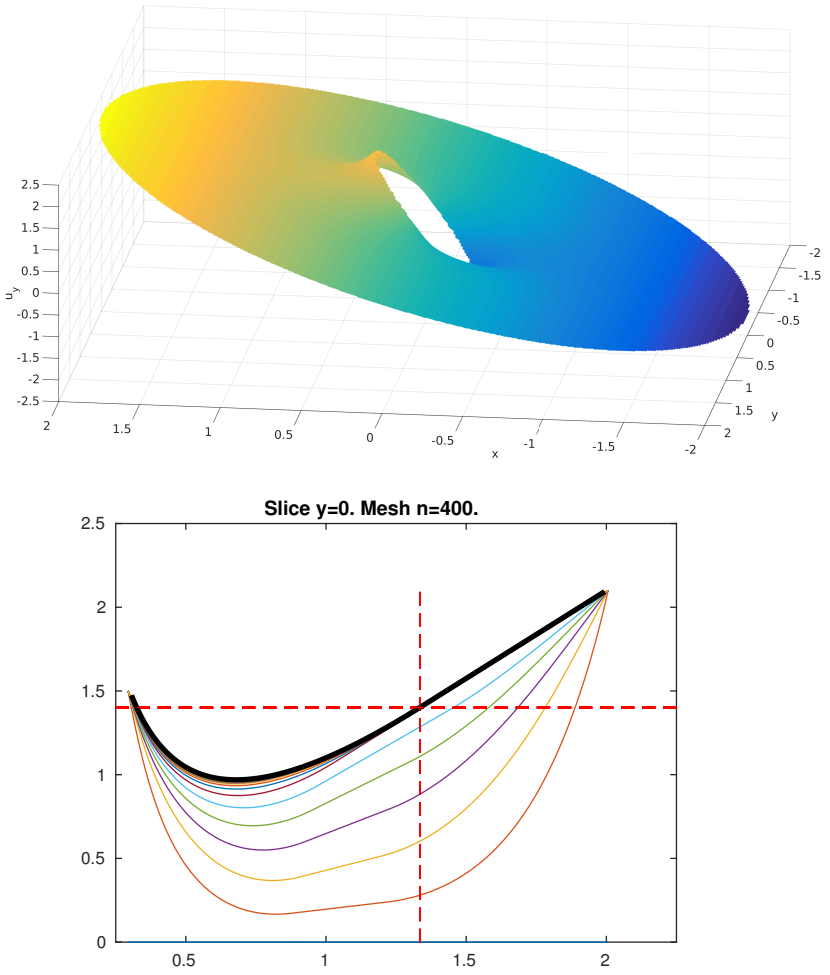

Figure 3.3: Computation in 2D of the Couette-Bingham flow. See text for the value of the physical parameters and detailed description. The computational mesh contains 400^2 points. The first (quiver) plot gives the velocity field inside the two cylinders. The colormap is based on the velocity magnitude which is precised in the two subsequent plots. The second plot is the surface of the second component of the velocity, $u_y(x, y)$, on the computation domain (note that u_x and u_y are symmetric so only one of them is shown). The third plot is the slice of the same u_y on the axis $y = 0$ (where $u_x = 0$), with several curves corresponding to the evolution in the duality loop (see main text). The colored curves start with a blue zero function corresponding to the initialization of the duality loop. The colored curves then converge to the black thick line which is the exact solution given by (3.57). The convergence of the duality loop to the exact solution holds true not only graphically as in this plot but also in L^2-norm when refining the computation mesh. The red dashed cross is given here for ease of localization of the yield zone at $x = r_y$: on the left, the material is yielded whereas on the right, it is unyielded (solid body rotation).

For completeness, we give in Figure 3.4 the results of the code for two other cases which can be exhibited by the model (3.53)-(3.54), namely the completely yielded regime and the pure plug regime. Geometry and fluid characteristics are the same as in the previous paragraph (illustrated by Fig. 3.3): only the values of the boundary condition are changed in order to obtain the two aforementioned regimes. We directly give the slice of u_y on the axis $y = 0$ (where $u_x = 0$) since the whole velocity field is well computed as in Fig. 3.3. On the left of Fig. 3.4, the boundary conditions are $\nu_i = 0.15$ and $\nu_e = 4.6$, associated to a purely yielded flow. Whereas on the right of Fig. 3.4, $\nu_i = 0.315$ and $\nu_e = 2.1$ leading to a solid body rotation in the whole domain: the velocity slice is a perfect line. In both cases, the exact solution is accurately computed.

Of note, in this special Couette geometry, it is evident that the Dirichlet boundary conditions on the speed are not homogeneous (i.e. $V \neq 0$), as assumed in the theory of the two duality methods performed in this paper. While we have just seen in previous paragraphs that the AL performs well even if the boundary condition is not equal to 0, it appears that the BM method as exposed in this article is not able to converge for this Couette geometry. However, it is possible to modify the BM algorithm in such a way it can handle non-homogeneous boundary conditions. For instance, this has been done in article [PCM02]. However this modification is problem dependent and need to be done on a case by case basis. Since the Bingham-Couette problem with non-zero boundary condition is not the main objective of this paper, we do not perform such implementation. As a consequence, we do not present the results with the BM method for the Bingham-Couette flow. However, in the main text, simulations are performed with homogeneous boundary conditions and it is shown that AL and BM methods give identical results for V, as expected by the theory.

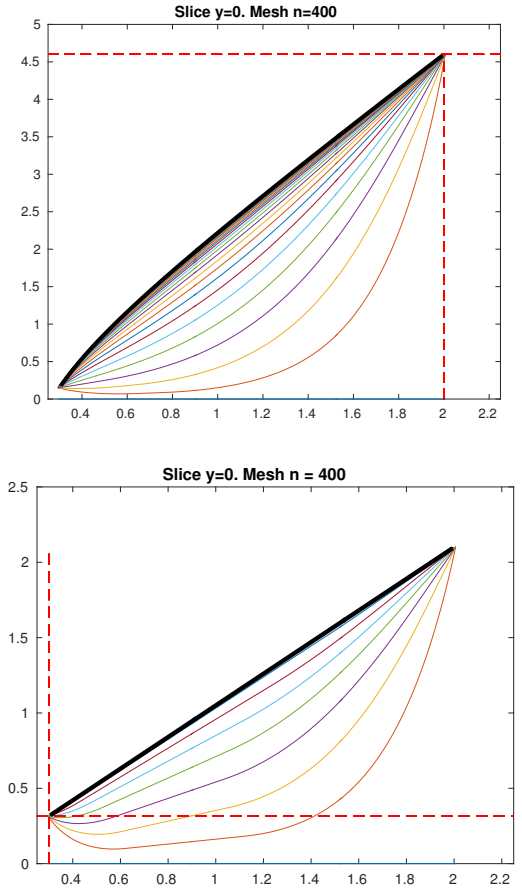

Figure 3.4: Slice of u_y on the axis $y = 0$ (where $u_x = 0$), with several curves corresponding to the evolution in the duality loop (as in Fig. 3.3(bottom), see also main text). The colored curves start with a blue zero function corresponding to the initialization of the duality loop. The colored curves then converge to the black thick line which is the exact solution of problem (3.53)-(3.54). The red dashed cross is given here for ease of localization of the yield zone at $x = r_y$: on the left, the material is yielded whereas on the right, it is unyielded (solid body rotation). Geometry and fluid characteristics are the same as in Fig. 3.3, only the values of the boundary condition are changed. Left: $\nu_i = 0.15$ and $\nu_e = 4.6$, case of a completely yielded material (the red cross in thus exactly on the right boundary). Right: $\nu_i = 0.315$ and $\nu_e = 2.1$, case of pure plug regime (the red cross in thus exactly on the left boundary).

3.5.2 *Well-balanced test on stochastic bottom*

In this first test, we consider a bottom defined as a random perturbation of a parabolic bottom over a Ω-plane with an angle $\alpha = 30°$. And the free surface is parallel to the reference plane as shown in Figure 3.5. The random perturbation is considered at each point of the mesh, which has been set to 100^2 points in the domain $[0,1] \times [0,1]$. The initial condition is defined as follows:

$$H(\boldsymbol{x},0) = \max(6 - b(\boldsymbol{x}), 0) \quad \text{with} \quad b(\boldsymbol{x}) = 4e^{-\tilde{r}} + 15\left((x_1 - 0.5)^2 + (x_2 - 0.5)^2\right),$$

being $\tilde{r}$ a random number between 0 and 1. We see in Figure 3.5 that this leads to complex wet/dry fronts. We set $\eta = 10^{-3}$ m^2.s^{-1}, $\beta = 10^{-3}$ m.s^{-1} and $g = 9.81$ m.s^{-2}. For τ_y, one can take any value greater than the smallest one ensuring that condition (3.48) is fulfilled.

If we consider the initialization of the multiplier defined in Theorem 1 (eqs (3.45)-(3.46)), the stationary solution is preserved up to machine precision for a value of τ_y verifying condition (3.48). For sake of conciseness we do not show the illustrations here.

In the present test, we instead initialize the multipliers to zero. The simulation is done from $t = 0$ to 1. Actually, at the first time iteration, the multipliers converge (inside the duality loop) to some function which then remains unchanged along the subsequent time iterations. As in 2D the multiplier is (intricately) not uniquely defined, it is not assured that the iterative algorithm converges to the one defined by (3.45)-(3.46), which ensures the exact well-balanced property. Nevertheless, we can see numerically that both AL & BM schemes still preserve the stationary solution with a good accuracy. In Figure 3.6, the multiplier to which the algorithm converges is plotted for illustration (this is done with the BM method but the results are the same with the AL algorithm). We obtain that the time averaged L^2 error for $t \in [0,1]$ is 6.3×10^{-4} for H and 1.4×10^{-8} for the velocity norm. The averaged difference between $H(x,t)$ and the initial condition, for $t \in [0,1]$, is represented in Figure 3.7, together with the averaged norm of the velocity (also for $t \in [0,1]$).

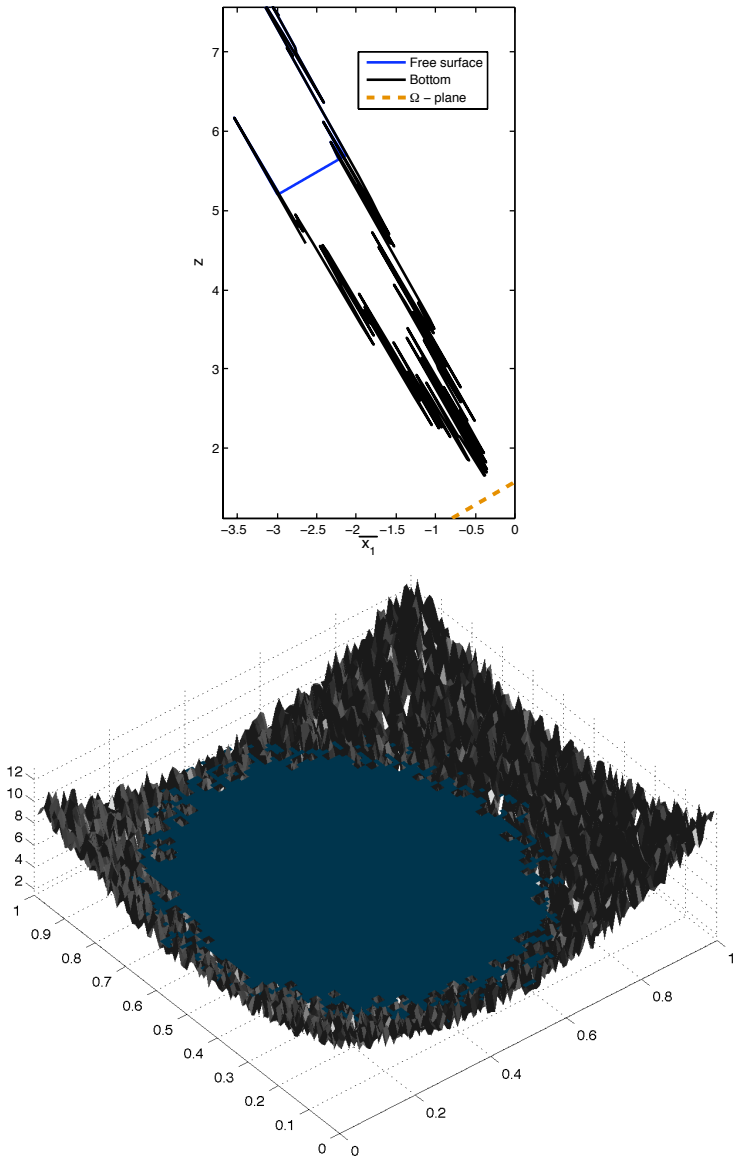

Figure 3.5: Left: slice of the bottom and the free surface at $x_2 = 0.5$ in *global coordinates* (meaning that $\overline{x_1}$ is obtained via the rotation associated to the angle α, see Fig. 3.1). Right: bottom $b(\mathbf{x})$ (in black) and initial condition $b + H$ (blue), in *local* coordinates.

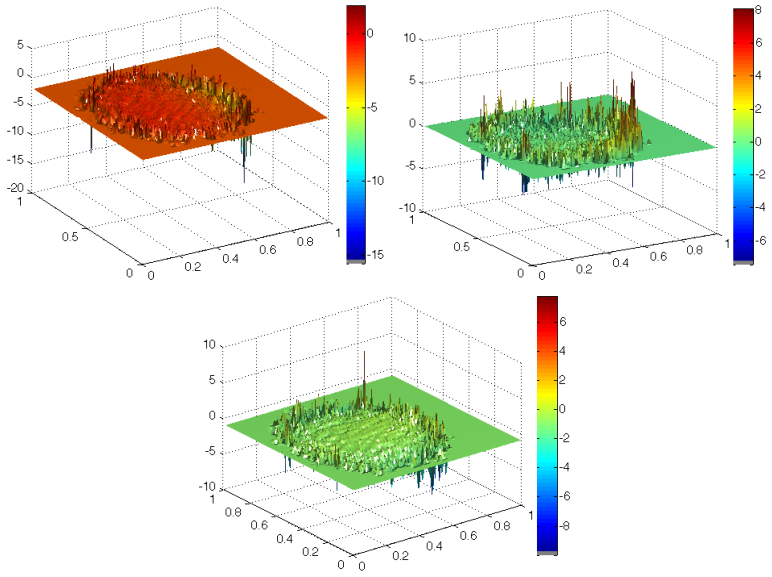

Figure 3.6: Multiplier at $t = 1$. Left: Π^k_{11}, center: Π^k_{12}, right: Π^k_{22}, being k the last iteration of the duality algorithm.

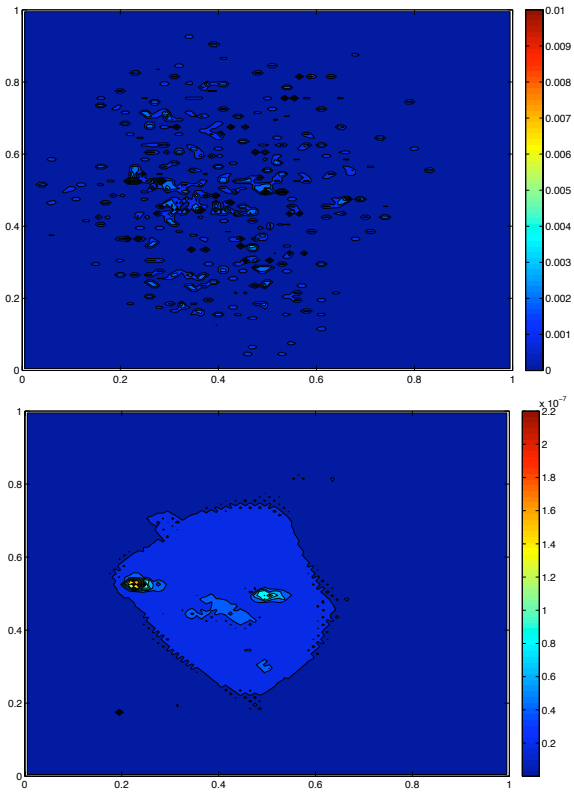

Figure 3.7: Left: Averaged error, $|H(x,t) - H(x,0)|$ for $t \in [0,1]$. Right: identically, averaged norm of the velocity for $t \in [0,1]$.

3.5.3 *Well-balanced test on academic avalanche*

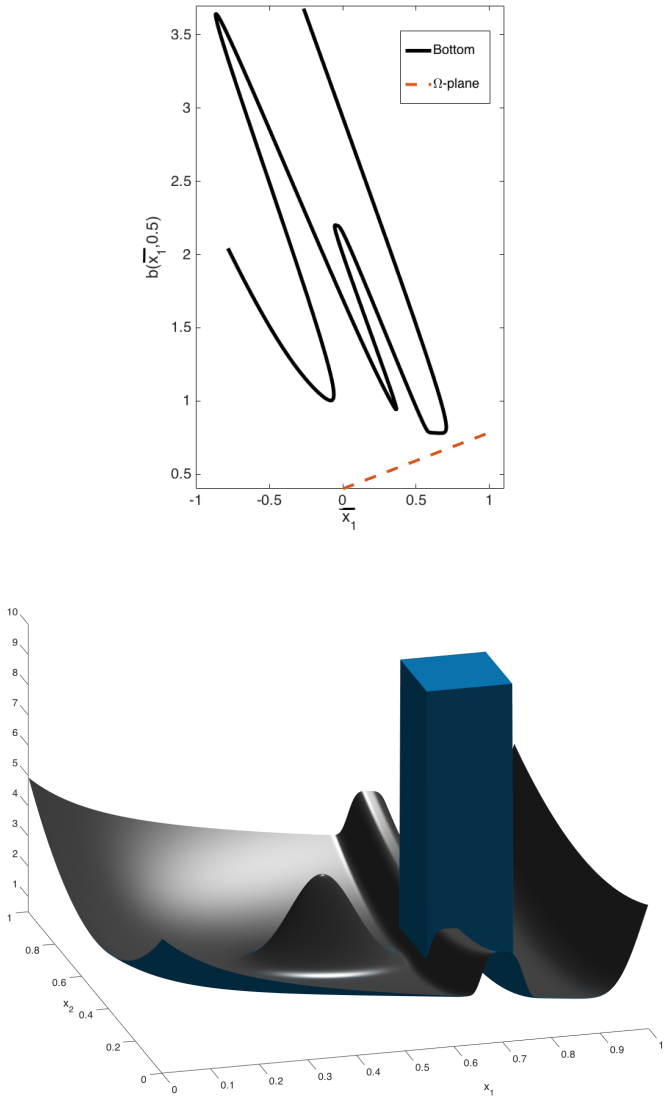

Figure 3.8: Left: slice of the bottom $b(\overline{x_1}, 0.5)$ with the plane of reference inclined with an angle of 20°, in *global coordinates* (meaning that $\overline{x_1}$ is obtained via the rotation associated to the angle α, see Fig. 3.1). Right: bottom $b(\mathbf{x})$ (in black) and initial condition $b + H$ (blue), in *local* coordinates.

This test is a dam break simulation where the Ω-plane is sloping at $\alpha = 20°$ and the bottom with two obstacles is defined as follows on $[0;1]^2$ (cf Figure 3.8):

$$\begin{aligned} b(\mathbf{x}) \quad = \quad & 1.5e^{-[20(x_1-0.75)]^4} + 6e^{-[5(x_1-1.25)]^4} + 3e^{-[10(x_1-0.5)]^2-[18(x_2-0.5)]^2} \\ & + \left(10(x_2-0.5)^2+1\right) 1.1e^{-0.9x_1} + 1.1e^{-9x_1}. \end{aligned} \tag{3.58}$$

As initial condition, we set $V \equiv 0$ and (see Figure 3.8)

$$H(\mathbf{x}) = \begin{cases} 10 - b(\mathbf{x}) & \text{if } (x_1, x_2) \in [0.7; 0.89] \times [0.4; 0.6], \\ 0 & \text{otherwise .} \end{cases} \tag{3.59}$$

We set $\eta = 10^{-3}$ m^2.s^{-1}, $\tau_y = \sqrt{2}/2$ m^2.s^{-2}, $\beta = 10^{-3}$ m.s^{-1} and $g = 9.81$ m.s^{-2}. Even though b is defined analytically and it is an academic avalanche, this test is very demanding due to the high slope and the strong gradients of the bottom as well as the quantity of material in the initial column (note the strong aspect ratios in Figures 3.8 left and right). With these values of the parameters, the material reaches a stationary state around $t = 1$ s, so we made simulations up to $t = 6$ s to check the ability of the 2D scheme to preserve this rigid free surface. This test has a rich hydrodynamics, as shown on Figures 3.10, 3.11 and 3.12. Recall that $V = 0$ on $\partial\Omega$. In the first phase of the collapse of the column, there are reflections (principally in the x_1 direction) on the wall at $x_1 = 1$ and on both obstacles (ridge at $x_1 = 0.75$ and Gaussian at $(x_1, x_2) = (0.5, 0.5)$) inside the domain (see $t = 0.05$ s). This notably leads to counterwaves which collide on the ridge (see $t = 0.09$ s and $t = 0.11$ s). Then, the material essentially separates in two parts on each side of the ridge and then reaches a steady state. In the upper part the material oscillates for a short time (feeding a bit the other side of the ridge), cf $t = 0.21$ and 0.26 s on Figure 3.11. The lower part of the material separates and goes around the Gaussian to finally meets at the bottom of the hill and reaches a stationary shape with $V \ll 1$ and H with a shape with very high gradients (after $t \approx 1$ s, see Figures 3.12 and 3.13). It is very difficult to compute a stationary solution in this kind of configuration with wet/dry fronts but we see in Figs 3.13-3.14 that our scheme performs well to do so: the velocity is very small ($\|V\|_2(\Omega) = 1.5e-9$) and the level lines $\{\mathbf{x}|H(\mathbf{x}) = 0\}$ are indeed very well superposed between $t = 5$ and 6 s. Note that these results are computed on a mesh with 450^2 points and can be considered as converged in terms of spatial resolution. Indeed, Fig. 3.14b shows a mesh convergence study of the level lines $\{\mathbf{x}|H(t = 6, \mathbf{x}) = 0\}$ for various Δx. It can be seen that the results for the two more refined meshes are very close.

We also use this test to compare the AL and the BM methods in terms of numerical cost. Note that following our 1D study for BM [FGV14, Section 3.1.3], we directly present the wet/dry front optimized version, ϖ_{opt}, of the optimal choice of the ω parameter. We proceed as follows. For both methods, we simulate from $t = 0$ to $t = 1$, with 110^2 mesh points for the Ω square, and we study the cost of the duality loops as a function of the duality parameter (we use 14 discrete values between 0.01 and 64). This cost is defined as the sum, along all the iterations in time (t^n), of the iterations of each duality loop used to compute V^n. We perform this study for four values of

$\tau_y = \sqrt{2}/20, \sqrt{2}/2, 2\sqrt{2}$ and $5\sqrt{2}$ $m^2.s^{-2}$, which are representative of 4 different dynamics of this 2D test case. Remark that we limited the number of iterations in a dual loop at 10,000 iterations: in practice, it is not reached except for the BM method at $\tau_y = \sqrt{2}/20$ $m^2.s^{-2}$. Consequently this does not change the following conclusions but allows to perform this study in a more reasonable CPU time. The results are presented in Figure 3.9. Recall that the duality parameter is taken as a constant for all the time iterations for the AL and the standard BM. However, when optimal BM is used with the a priori derived $\varpi_{opt} = \varpi_{opt}(t)$, one can not give a meaning to the cost for a given ϖ and there is only one value of the duality cost: this leads to the horizontal lines in Fig. 3.9. We can see that, for this dam break problem, when τ_y increases the duality cost decreases for both AL and BM methods. Remark that the BM curve for $\tau_y = \sqrt{2}/20$ $m^2.s^{-2}$ is far less convex than the other curves because, at some time iterations, it reached the maximum number of duality iterations (= 10,000) as mentioned above. But, still, we can observe an optimal value of ω, which is furthermore close to the ϖ_{opt} estimation. The AL seems to always be cheaper than the BM, especially at small τ_y. However, it can be seen that ϖ_{opt} always leads to a good estimation of the observed optimal cost and that when τ_y increases, this cost of the BM is closer to the cost of the AL. As a consequence, the optimal BM method can be very competitive w.r.t. the AL, especially at high τ_y. Indeed the optimal r for the AL method is not known a priori and the practitioner can be far from it, leading to significantly higher CPU times.

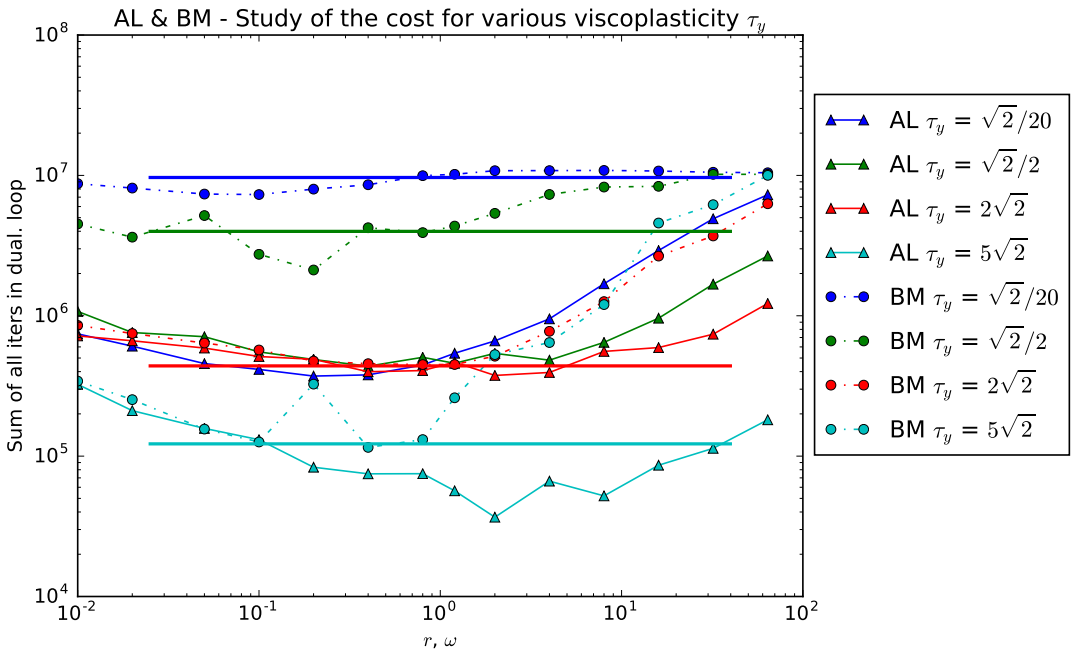

Figure 3.9: Duality numerical cost for four τ_y. The colored continuous curves are for the AL while the dashed ones are for the standard BM. The horizontal thick lines correspond to the cost for the BM with the optimal duality parameter ϖ_{opt} : their colors (varying with τ_y) correspond to the same colored dashed curve of the standard BM to which it principally needs to be compared; namely $\tau_y = \sqrt{2}/20, \sqrt{2}/2, 2\sqrt{2}, 5\sqrt{2}$ $m^2.s^{-2}$ is in blue, green, red, cyan, respectively.

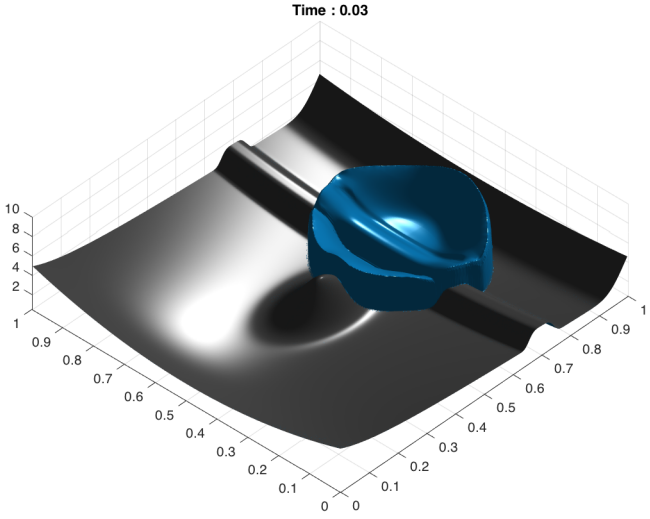

(a) t = 0.03

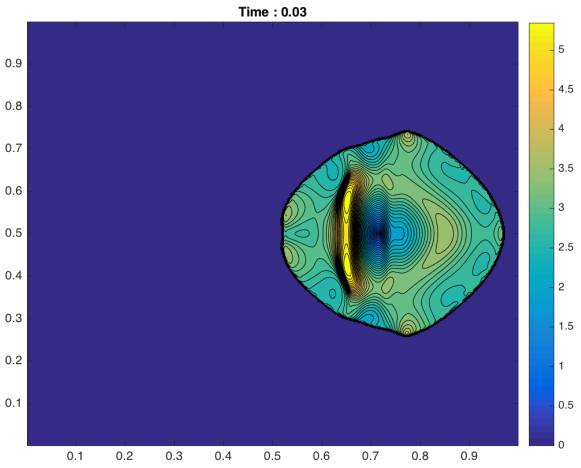

(b) $\|V\|_2(x)$, t = 0.03

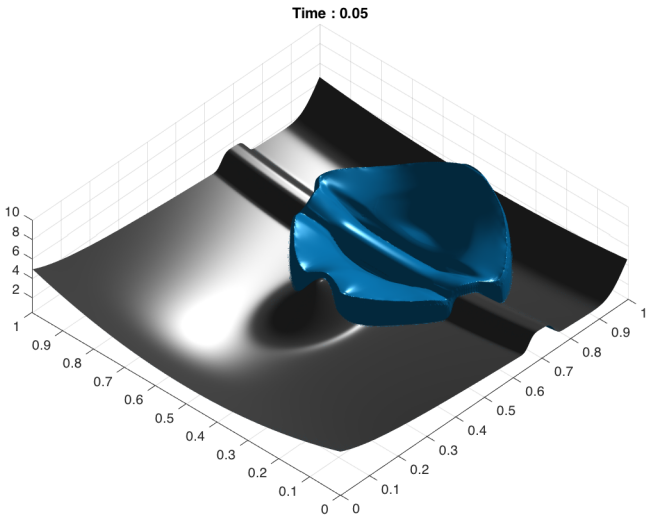

(c) t = 0.05

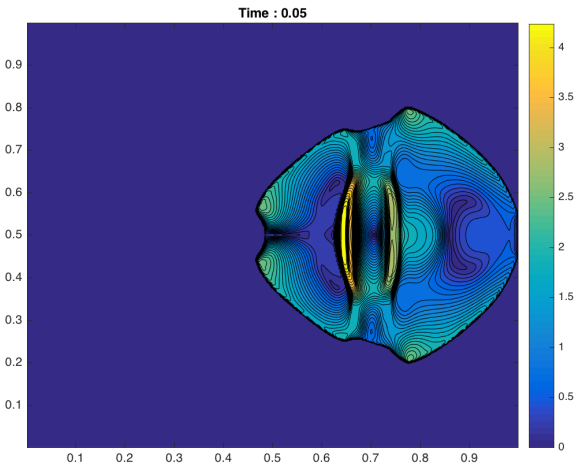

(d) $\|V\|_2(x)$, t = 0.05

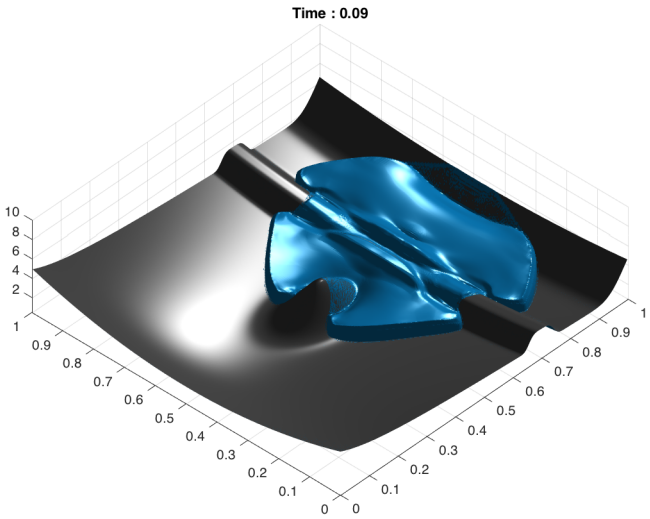

(e) t = 0.09

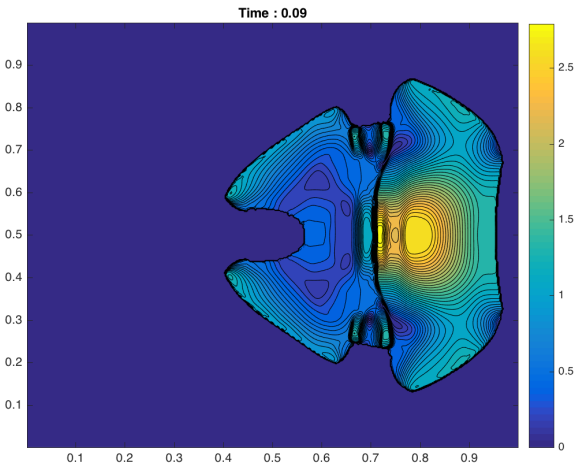

(f) $\|V\|_2(x)$, t = 0.09

Figure 3.10: Left: Free surface (blue) and bottom (black). Right: contours of $\|V\|_2(x)$. From t = 0.03 to 0.09.

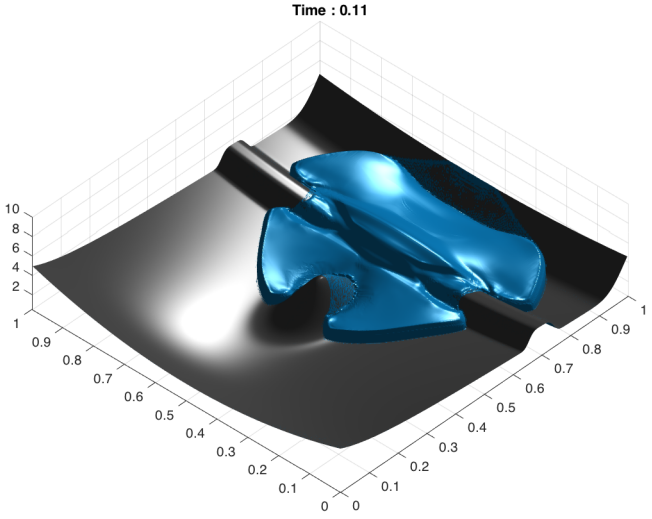

(a) t = 0.11

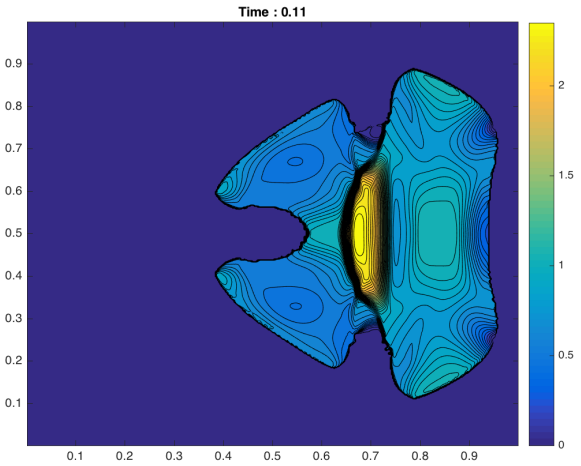

(b) t = 0.11

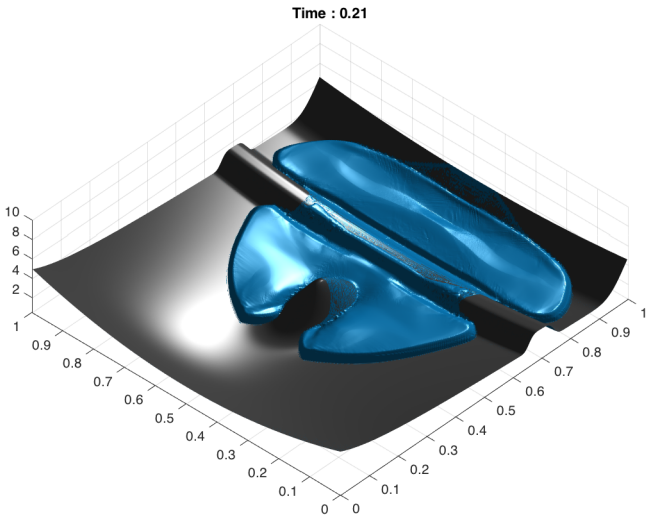

(c) t = 0.21

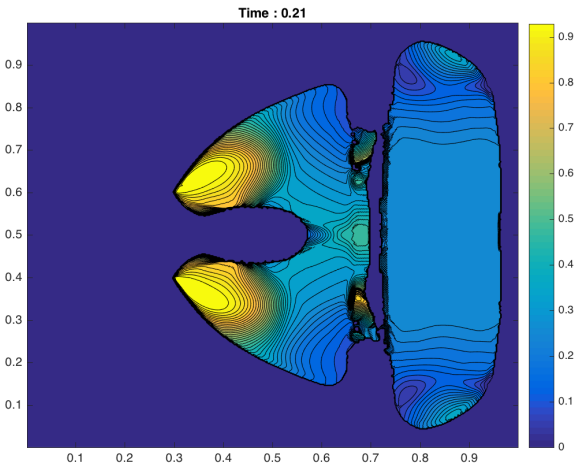

(d) t = 0.21

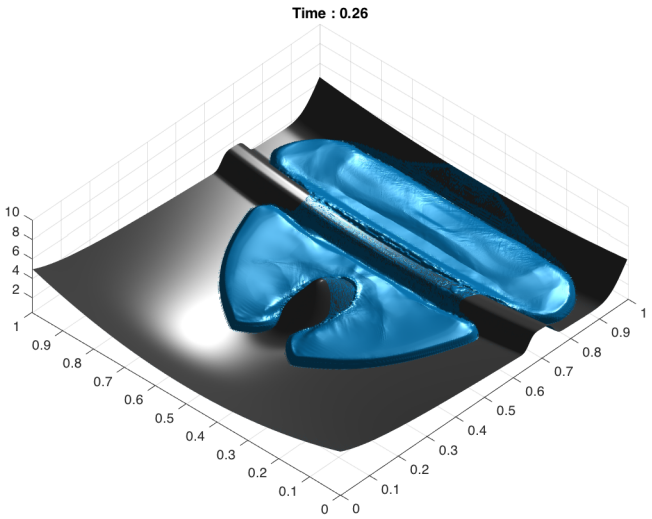

(e) t = 0.26

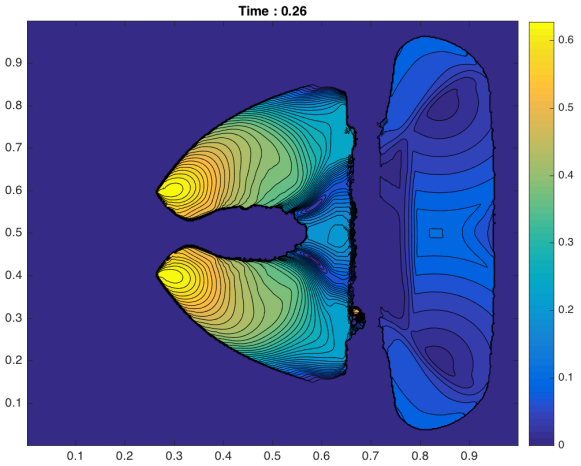

(f) t = 0.26

Figure 3.11: Left: Free surface (blue) and bottom (black). Right: contours of $\|V\|_2(x)$. From t = 0.11 to 0.26.

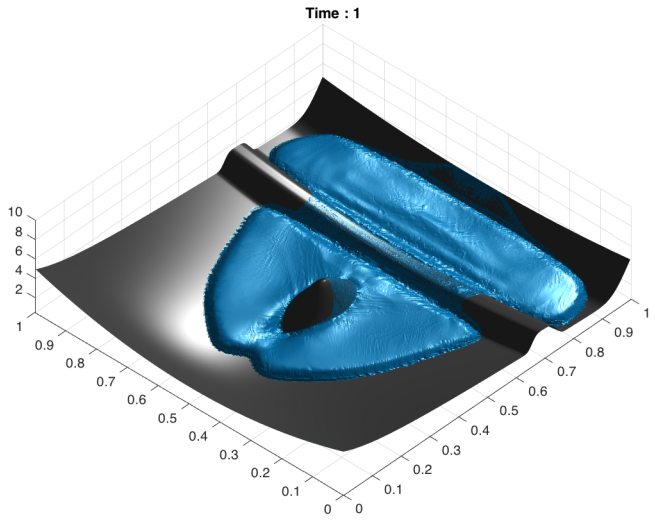

(a) $t = 1$

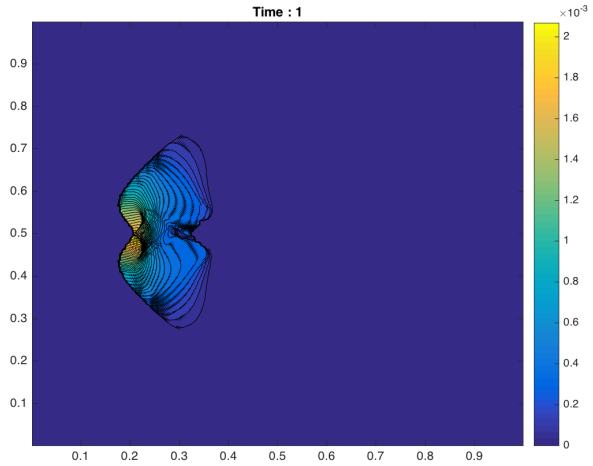

(b) $t = 1$

Figure 3.12: Left: Free surface (blue) and bottom (black). Right: contours of $\|V\|_2(x)$. At $t = 1$.

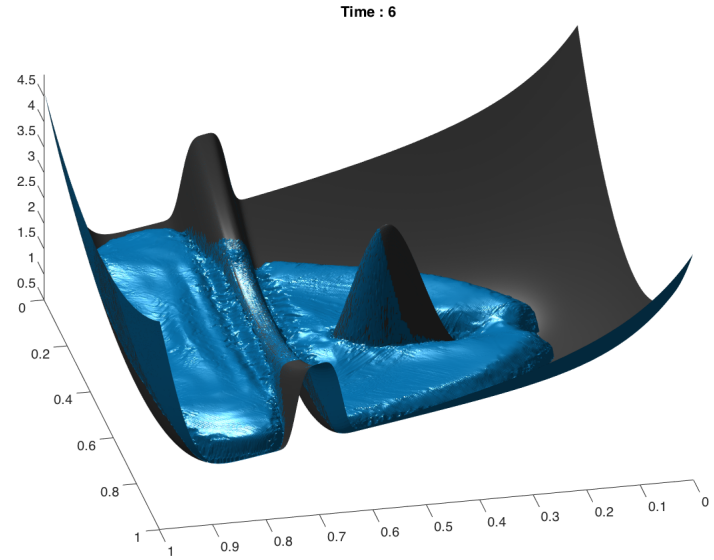

(a) Free surface at $t = 6$: rotated view to better see high gradients of H at the wet-dry front.

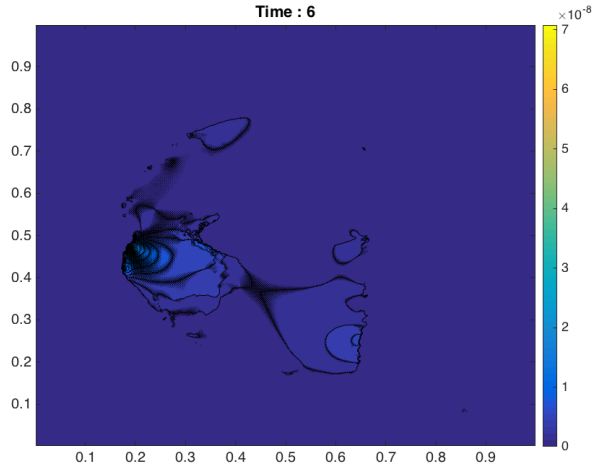

(b) Contours of $\|V\|_2(x)$ at $t = 6$. Note: $\|V\|_2(\Omega) = 1.5e-9$.

Figure 3.13: Details on the stationary state at $t = 6$.

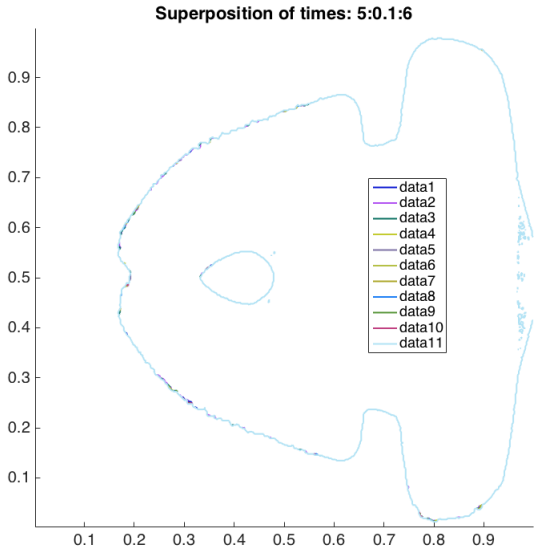

(a) Another stationary evidence. Square mesh with 450^2 points. Level line $\{\mathbf{x}|H(\mathbf{x}) = 0\}$ for different times: datai for $i = 1$ to 11 stands for t from 5 to 6 with a time step of 0.1.

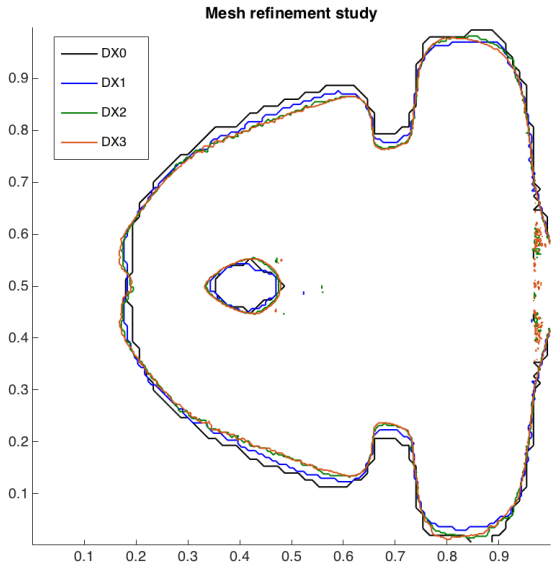

(b) Mesh refinement study: level line $\{\mathbf{x}|H(\mathbf{x}) = 0\}$ at $t = 6$ for different mesh sizes. DX0,1,2 and 3 stands for a square grid discretized with respectively $75^2, 150^2, 300^2$ and 450^2 mesh points.

Figure 3.14: Details on the stationary state & Mesh convergence study.

3.5.4 *Taconnaz avalanche path, Chamonix - Mont-Blanc*

(a) Photo of the upper part of the site (Dome du Gouter on the far left and Gros Bechard on the right), courtesy [Chr09]. Note the significant amount of ice and complexity of the terrain.

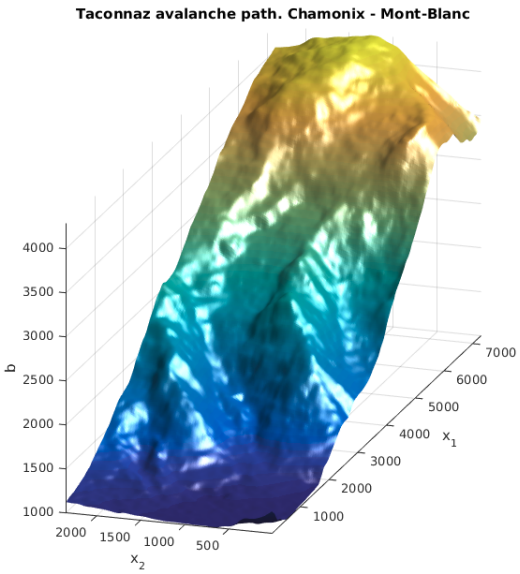

(b) Topography from ASTER GDEM: 431×213 mesh resolution. Dome du Gouter approximately at (6500,1600) and Gros Bechard at (3500,1000).

Figure 3.15: Topography of the Taconnaz avalanche path, Chamonix - Mont-Blanc.

In this section, we test the ability of the 2D numerical scheme to simulate an avalanche on a real topography. Namely, we choose the Taconnaz avalanche path in the region of Chamonix, France. This site is one of the longest in Europe with a length close to 7000 m

(avalanches can start around 3300 m above sea level and stop around 1000 m a.s.l.), a width between 300 and 400 m and a mean slope of 25° (with some portions in departure areas of avalanches of mean slopes 30°). Taconnaz is well known for a significant frequency of avalanches (composed of dense and mixed snow, with speed of 70 m/s in the worst case scenario), with 75 events between years 1900 and 2000 [Naa+10].
We obtain the topography of the Taconnaz avalanche path thanks to the ASTER Global Digital Elevation Model (GDEM) v2, whose initial resolution in x_1 and x_2 is around 25-30 m [AST09]. For simulation purposes, we interpolate the topography on a finer grid: we built a uniform square mesh with a 16 m resolution (431×213 points in $x_1 \times x_2$), see Fig. 3.15. Based on historical observations [Naa+10], we put on top of this topography a truncated Gaussian of material for H whose maximal height is 9 m and volume is 0.6×10^6 m^3 (observed volumes are between 0.01×10^6 and 1.5×10^6 m^3) at an altitude of 3700 m a.s.l on the slopes of Dome du Gouter, see Figures 3.16a and 3.16b. Namely,

$$H(t=0,x) = \max\left(0, -2 + 11e^{-(4.10^{-5})(x_1-6380)^2-(2.10^{-5})(x_2-1050)^2}\right). \tag{3.60}$$

This is used as an initial condition to represent the dense snow composing the avalanche; further $V(t=0) \equiv 0$. For the material, we set $\eta = 10^{-1}$ $m^2.s^{-1}$, $\tau_y = \sqrt{2}$ $m^2.s^{-2}$, $\beta = 2.10^{-3}$ $m.s^{-1}$, $g = 9.81$ $m.s^{-2}$. Of note, for a given real observed avalanche, it is very difficult to give precise values of these parameters so we put reasonable values which lead to an observed deposit of the avalanche in the field (see [Loc14]); in particular, we do not enforce that physical time scales are relevant, focusing only on the localization of the deposit. The objective is here to show that algorithms derived in this paper are applicable on real avalanches data to compute the stopping state. The fitting of these parameters is out of the scope of this paper and is left for future works.

The dynamics of this test, which spans from $t = 0$ to $120,000$ s can be decomposed in 3 phases, going to the stationary state. A first "fast" phase on a "short" time scale ($t = 0$ to approx. 3000 s) where the deposit reaches the bottom of Taconnaz path. The front is not stationary but it is not far from its stationary localization, see Figure 3.17. In a second phase, on a longer time scale (from approx. $t = 3000$ s to $40,000$ s), the velocities are decreasing but there is a significant motion of the material in the whole deposit from the mountain top to the bottom: this leads to a progressive advance of the front of the avalanche. In a last "slow" phase on a much longer time (from approx. $t = 40,000$ s to $106,000$ s), there is essentially no motion on the top $3/4$ of the deposit and most of the material is in the $1/4$ bottom part where the slope is still significant (see H on Fig. 3.21 (b) Bottom): as a consequence there is a slow but progressive sliding motion of this bottom part (as also shown by the time evolution of $\max_{x\in\Omega} \|V\|_2(t,x)$

on Figure 3.19) and the deposit front is moving a bit (compare Figs. 3.18 and 3.20) but finally stops at about $t = 106,000$ s. We show that the front $\{\mathbf{x}|H(\mathbf{x}) = 0\}$ is completely stationary after $t = 106,000$ s by also showing the solution at $t = 120,000$ s (Fig. 3.20). Note that the final shape of the deposit is very close to one of the biggest deposits shown in [Loc14] and measured from true avalanches at Taconnaz. Our test thus covers all the topographical difficulties associated to the Taconnaz avalanche path.

It can be seen that the stationary state is very well computed: the final velocity is locally of order 10^{-10}, and globally $\|V\|_2(\Omega) \leqslant 4.6 \times 10^{-9}$, see Figure 3.20. The position of the wet/dry front is shown to be stationary with superimposed level lines $\{\mathbf{x}|H(\mathbf{x}) = 0\}$ after $t = 106,000$ s with a very good accuracy (it does not move up to $t = 120,000$ s), see Figure 3.22. Note that the stationary state is difficult to capture since the major part of the deposit accumulates in a zone where there is a significant slope of b, see Figure 3.21. The viscoplastic nature of the material with a bumped surface of the deposit (H) is clearly exhibited in this stationary state. These results show the ability of present well-balanced schemes to perform accurate simulations for Bingham type materials with real topographies from digital elevation models (DEM).

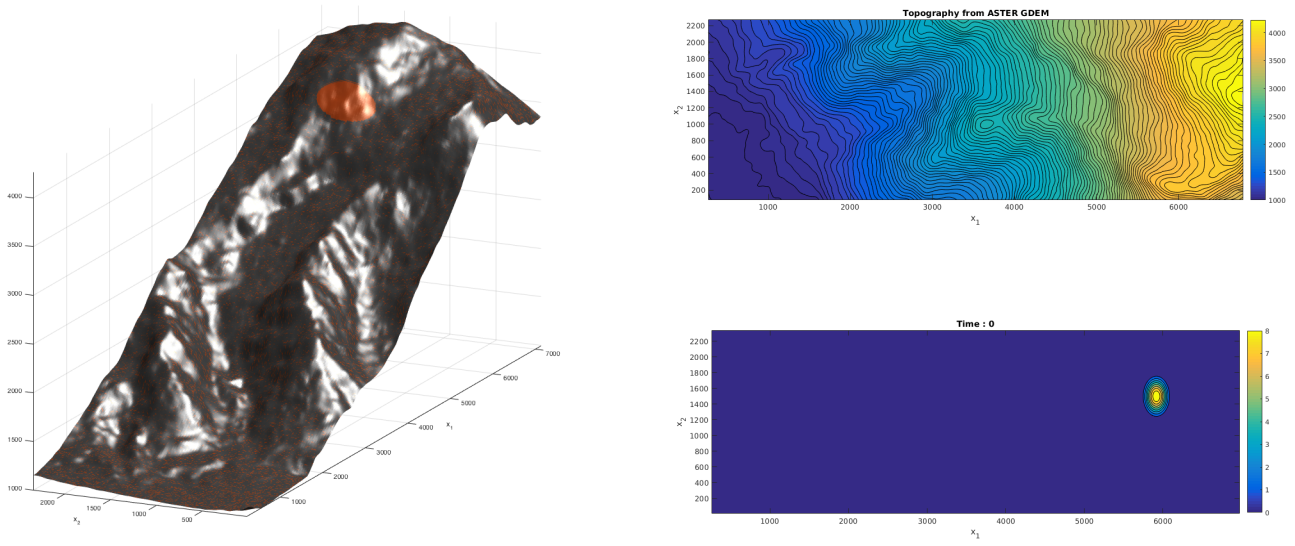

(a) topography $b(\mathbf{x})$ (black) and free surface H (brown).

(b) filled contours of b (top) and H at $t = 0$ (bottom).

Figure 3.16: Details on topography and initial condition of the simulation on Taconnaz avalanche path. Note that Fig. 3.21b gives also b together with its gradient.

3.6 CONCLUSIONS

In this article, we presented 2D numerical schemes in the finite volume framework which allow to compute accurately shallow viscoplastic flows: thanks to a specific design coupling duality methods and well-balancing, they preserve with a good accuracy the stationary solutions (naturally associated to the viscoplasticity) on general 2D shapes of bottom and free surfaces. These schemes deal with true wet/dry fronts and there is no need to add a small quantity of material in all the domain (as sometimes done by other methods). The well-balanced property is shown to be exact on two kinds of stationary solutions (Theorem 1). A careful study of the optimal cost of the two duality methods (Augmented Lagrangian and Bermúdez-Moreno) was performed and showed that the BM method can become competitive at high τ_y due to the fact that the optimal duality parameter is known a priori. Such studies are quite rare in the 2D framework. We finally give numerical evidence that these numerical methods can be successfully applied to real topographies as shown by the avalanche test case in the Taconnaz path obtained from ASTER GDEM. As a by-product of this study, we also provide a 2D benchmark for classic 2D Bingham codes thanks to an analytic solution with totally non homogeneous boundary conditions on the velocity.

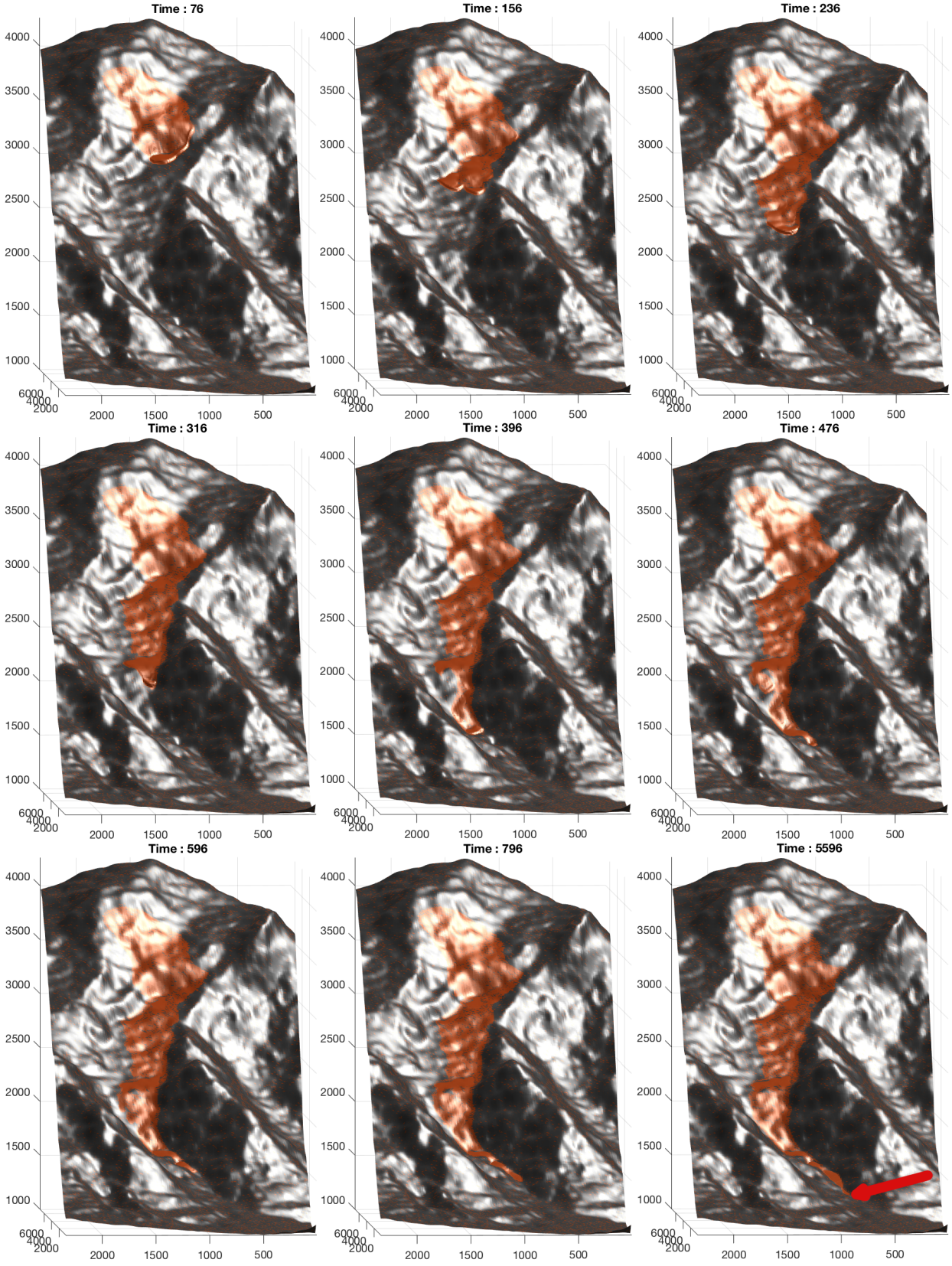

Figure 3.17: First times of the avalanche between $t = 76$ and $t = 5596$: topography b (black) and free surface H (brown). See also Fig. 3.18 for the corresponding velocities. At $t = 5596$, the red arrow shows the localization of the zoom made on Fig. 3.21a.

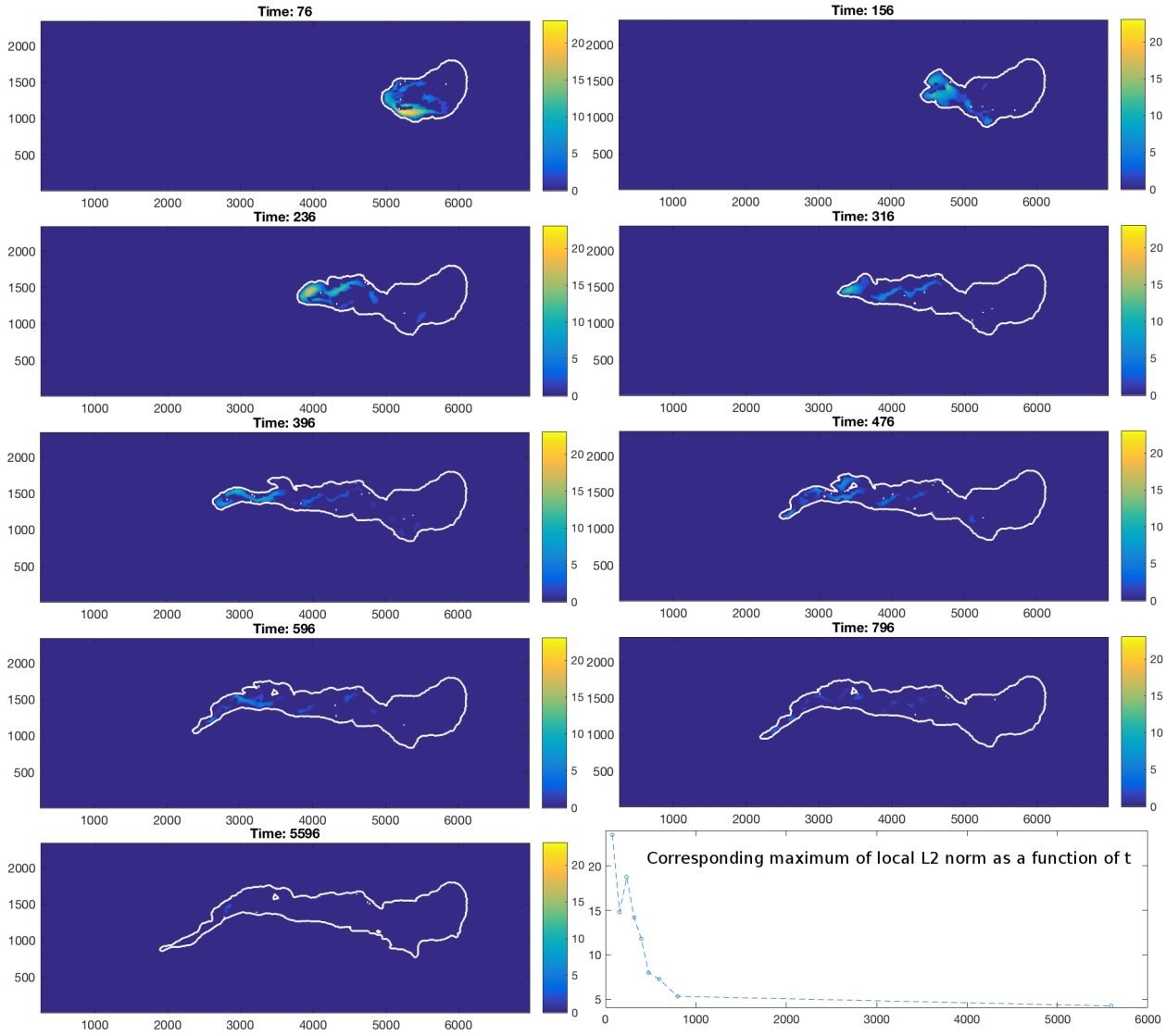

Figure 3.18: First times of the avalanche between $t = 76$ and $t = 5596$: $\|V\|_2(x)$ (filled contours) and level line $\{x|H(x) = 0\}$ (white thick line). The colorbar is the same on all snapshots so we also give, at the bottom right of the figure, the corresponding maximum values of $\|V\|_2(x)$ as a function of time. Note: at $t = 5596$, $\max_x \|V\|_2(x) = 4.22$, see also Fig. 3.19 for the total history. See also Fig. 3.17 for the corresponding 3D views of b and H.

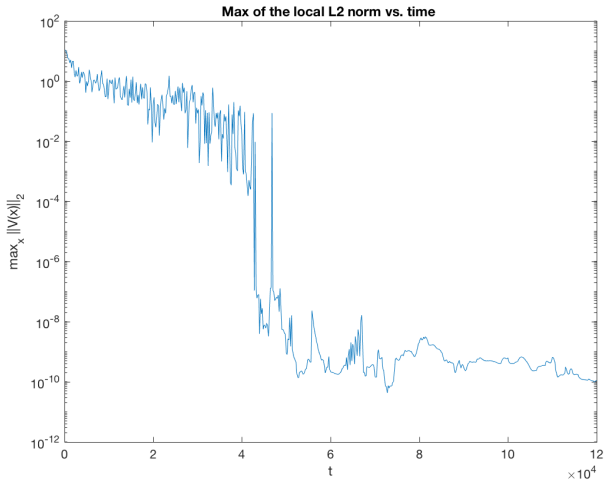

Figure 3.19: History of V converging to the stationary state for the Taconnaz test, in semi-log scale.

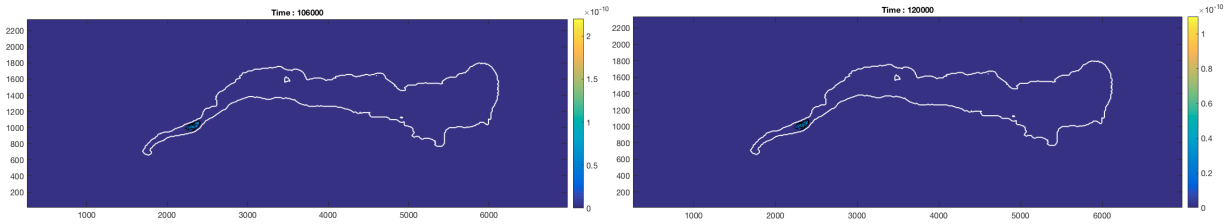

(a) $t = 106,000$ (b) $t = 120,000$

Figure 3.20: Reaching the stationary state of the avalanche: $\|V\|_2(x)$ (filled contours) and $\{x|H(x) = 0\}$ (white thick line). Note: $\|V\|_2(\Omega) = 9.0e-9$ at $t = 106,000$ (a) and $4.6e-9$ at $t = 120,000$ (b).

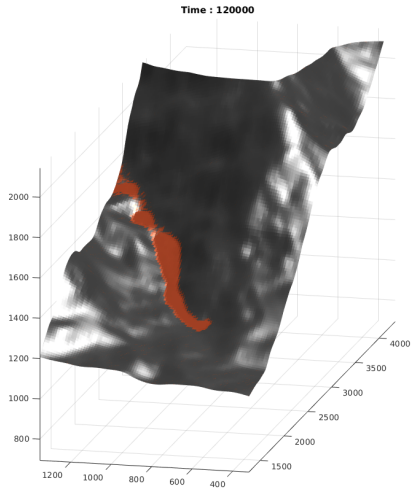

(a) Zoom (mentioned in Fig. 3.17) on the 3D view of $b(\mathbf{x})$ (black) and H (brown) at the front.

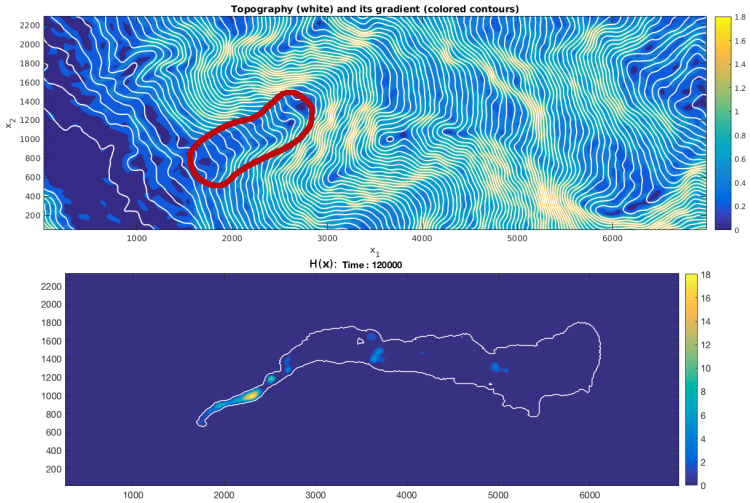

(b) Top: b with white contours and $\|\nabla b\|_2(\mathbf{x})$ with colored contours. Thick red line localize the bottom part of the deposit shown on the left (for ease of reading only). Bottom: $H(\mathbf{x})$ (filled contours) and $\{\mathbf{x}|H(\mathbf{x}) = 0\}$ (white line = total deposit shape).

Figure 3.21: Reaching the stationary state of the avalanche: $t = 120,000$, physiognomy of the deposit front and evidence of the slope of b.

(a) Total deposit

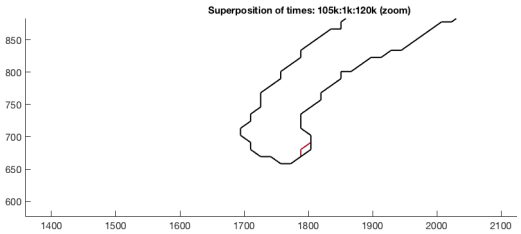

(b) Zoom on the front of the avalanche of left figure.

Figure 3.22: Another evidence of the stationary state: (a) levels $\{\mathbf{x}|H(\mathbf{x}) = 0\}$ from $t = 105,000$ to $120,000$ with step 1000. Two colors are seen: the red contour is $t = 105,000$, then from $t = 106,000$, all contours are superimposed and correspond to the black contour. (b) A zoom is needed to better see this small motion (of order one mesh point) between $t = 105,000$ and $t = 106,000$.

4

AL FOR 2D BINGHAM IN EXPANSION-CONTRACTION

This chapter deals with the Ph.D. Thesis (2015 - 2018) of Arthur Marly, who I am advising at UMPA, ENS de Lyon. Synthesized results presented here were published in [MV17]. They were done in the context of a CNRS INSU-INSMI grant of the Tellus program 2016.

We study the ability of Augmented Lagrangian (AL) methods to simulate two dimensional flows of viscoplastic materials in rectangular expansion-contraction geometries. We are specifically interested in the numerical simulation of recent physical experiments of Chevalier et al. [Che+13] and Luu et al. [LPC15], cf Fig . We provide a detailed analysis of the velocity profiles and unyielded zones.

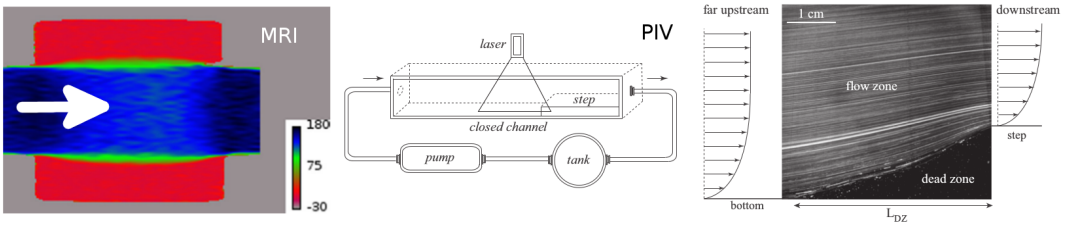

Figure 4.1: To fix the ideas, a brief schematic overview of the experimental configurations studied by [Che+13] with MRI (left, in $\mu m/s$) and [LPC15] with Particle Image Velocimetry (PIV, middle and right).

Even if the fluids used in the above experiments are described by a Herschel-Bulkley law, we restrict ourselves to a Bingham constitutive law since, as mentioned in the PhD thesis of Chevalier, it still allows to have good insight of these viscoplastic flows. This will be confirmed in the present results. Moreover for such experiments, flows are studied when reaching a stationary state.

Precisely, we thus want to solve the following 2D stationary, so called, Stokes-Bingham problem:

$$\begin{cases} -\nabla.\tau + \nabla p = 0 \\ \qquad \nabla.\mathbf{u} = 0, \end{cases} \tag{4.1}$$

where τ is given by the Bingham constitutive law:

$$\begin{cases} \tau = 2\eta D(\mathbf{u}) + \tau_y \dfrac{D(\mathbf{u})}{|D(\mathbf{u})|} \Leftrightarrow D(\mathbf{u}) \neq 0 \\ |\tau| \leqslant \tau_y \Leftrightarrow D(\mathbf{u}) = 0. \end{cases} \tag{4.2}$$

This kind of viscoplastic formalism was already presented in page 10, together with the state of the art on numerical methods.

Of course, since it is widely used in practical applications, the expansion-contraction geometry has been studied in many previous works. Let us mention the work of de Souza et al. [Sou+07] which seems to be the first work close to the present study: they present experiments with Carbopol and compare with numerical solutions obtained with a regularization method. In addition, similar configurations are simulated in [RF13] and [RGF15] using an AL method on unstructured meshes. Their code is implemented with the excellent Rheolef library [Sar15] of Saramito and coworkers (see e.g. [RS03] for the flow around a cylinder). An impressive range of Bingham numbers, aspect ratios of the geometry and shapes of the cavity (rectangular, sinusoidal wave, triangular, semi-fractal) are presented. But they did not describe in depth the velocity profiles in conjunction with the plug zone, along the lines of the physical experiments of Coussot's and Chambon's groups [Che+13; LPC15].

The characteristics of [MV17] are the following.

- As said previously we use an AL approach and we adopt a finite-difference approach (on Cartesian meshes) for the discretization in space. This is in the spirit of Wachs and co-workers (see [VWA05] or, for a longer description, [GW11]), as well as E. Muravleva, A. Muravleva, Olshanskii and coworkers (see e.g. [MO08], [Mur15]) but our implementation differs on the resolution of the induced generalized Stokes problem which is here also tackled with another AL approach (to fulfill the incompressibility condition). See section 4.2. In addition, we make a finely tuned use of parallel linear system solvers which helps in using very fine (isotropic) Cartesian meshes, not that often published in the simulation of viscoplastic flows considered here.

- Code results are scrutinized in terms of accuracy of the localization of the plastic zone and computational times, given the fact that we impose a really small residue ($\sim 10^{-12}$) in the AL loop : such information are rarely given in the associated literature and can serve for future comparisons.

- As a validation/application of the code, we retrieve the results of the *frustrated* regime studied in [Che+13] and additionally show the evolution of the yielded boundary layer width as a function of the Bingham number. We also retrieve the existence of a so-called *slip line* and the Poiseuille-like behaviour above this slip line shown in [LPC15] (showing further more that it is robust on the variation of the choice of the angle of the tilted reference frame). Of note, we also give the horizontal length of

the dead zone at the corner of the cavity as a function of the Bingham number (section 4.3).

4.1 DESCRIPTION OF THE PROBLEM

The geometry and notations of the expansion-contraction problem are illustrated in figure 4.2, where only the upper half is shown. In the following, we will use either (4.1)-(4.2) or their dimensionless form (by denoting dimensionless variables with a *tilde* symbol) which reads:

$$\begin{cases} -\tilde{\nabla}.\tilde{\tau} + \tilde{\nabla}\tilde{p} = 0 \\ \qquad \tilde{\nabla}.\tilde{\mathbf{u}} = 0, \end{cases} \tag{4.3}$$

with

$$\begin{cases} \tilde{\tau} = 2\tilde{D}(\tilde{\mathbf{u}}) + B\dfrac{\tilde{D}(\tilde{\mathbf{u}})}{|\tilde{D}(\tilde{\mathbf{u}})|} \Leftrightarrow \tilde{D}(\tilde{\mathbf{u}}) \neq 0 \\ |\tilde{\tau}| \leqslant B \Leftrightarrow \tilde{D}(\tilde{\mathbf{u}}) = 0. \end{cases} \tag{4.4}$$

In this dimensionless Stokes-Bingham model, there is a unique dimensionless number $B = \frac{\tau_y D}{\eta \bar{U}}$, called the Bingham number, where D is the small channel half-width (see figure 4.2) and $\bar{U}$ is the mean flow velocity in the x-direction at the entrance (see (4.5)). Indeed, the dimensionless model is obtained from (4.1)-(4.2) by scaling the lengths with D, the velocities with $\bar{U}$ and stresses with $\frac{\eta \bar{U}}{D}$. In dimensional

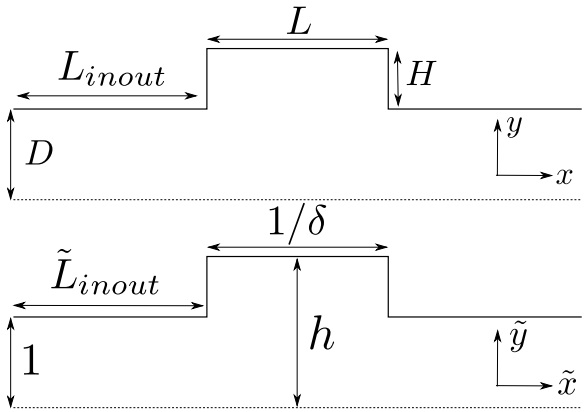

Figure 4.2: Geometry of the expansion-contraction and notations for the dimensional form of the model (top, cf. eqs. (4.1)-(4.2)) and the dimensionless one (bottom, cf. eqs. (4.3)-(4.4)). Only the upper half is represented thanks to the symmetry w.r.t. the x-axis.

variables, we have

$$\bar{U} = \frac{1}{D}\int_0^D u(0,y)dy. \tag{4.5}$$

We consider the two following aspect ratios:

$$h = \frac{D+H}{D} \qquad \text{and} \qquad \delta = \frac{D}{L}. \tag{4.6}$$

In the inlet and outlet, we set the flow equal to the Poiseuille flow (with a unit net flux) in the infinitely long channel. At the lateral wall, the velocity is set equal to 0. Of note, we present the results for the [Che+13] configuration in the dimensionless form, but we will use the dimensional form to compare more easily with the results in the configuration of [LPC15].

To sum up, in dimensionless variables, the free parameters are h, δ and the Bingham number B.

4.2 SALIENT FEATURES OF THE NUMERICAL RESULTS

As said in the introduction, we implemented an Augmented Lagrangian method as in the seminal work of Glowinski and coworkers [FG83; GW11]. The discretization in space is done with finite-differences on rectangular grids. As such, *present work is complementary to [RF13; RGF15] since it allows to compare the results between structured and non-structured grids discretizations.*

The first key point is that the simulations presented in the paper are much more converged in terms of the AL iterations than many of the associated simulations previously published. For instance, instead of enforcing a convergence of 10^{-6} for the Bingham AL loop's convergence criterion, we used $6 \cdot 10^{-12}$ (and also validated the code up to machine precision 10^{-15}). The second important point is that the linear systems which need to be solved are handled by the MUMPS library [Ame+01; Ame+06]. This massively parallel solver allows us to use very fine meshes up to $7.8 \cdot 10^6$ points and to obtain computational times shorter than 2 days on 16 cores.

Figure 4.3 shows typical computed velocity, pressure and $|\tilde{d}|$ (which approximates $|\tilde{D}(\tilde{u})|$ in the AL method) fields, for $\delta = 0.5$, $h = 2$ and $B = 5$. We directly remark that velocity, pressure and deformation are symmetric with respect to both middle axis in the $\tilde{x}$ and $\tilde{y}$ directions (and it is the same for the stress tensors). Hence, often in the sequel, we only show the upper-left quarter of the domain. Further, as often done in the literature, we cover the plastic zones in the stress fields with a black patch since there's no consistent notion of pressure or stress in the rigid zone, for the Bingham model (4.1)-(4.2).

Let us detail how we localize the plastic zones in the following sections. In figure 4.3 (bottom, right), instead of showing, as in the pressure field on its left, just one level of $\tilde{D}(\tilde{u})$ (or $\tilde{d}$, which is virtually equivalent, see next paragraph), we show the whole deformation field *in log scale* since it allows the reader to have a precise idea on how the numerical method is performing. Of note, this presentation is not quite often done in the literature: to our knowledge [PFM09] is one of the very few published papers showing the complete Lagrange

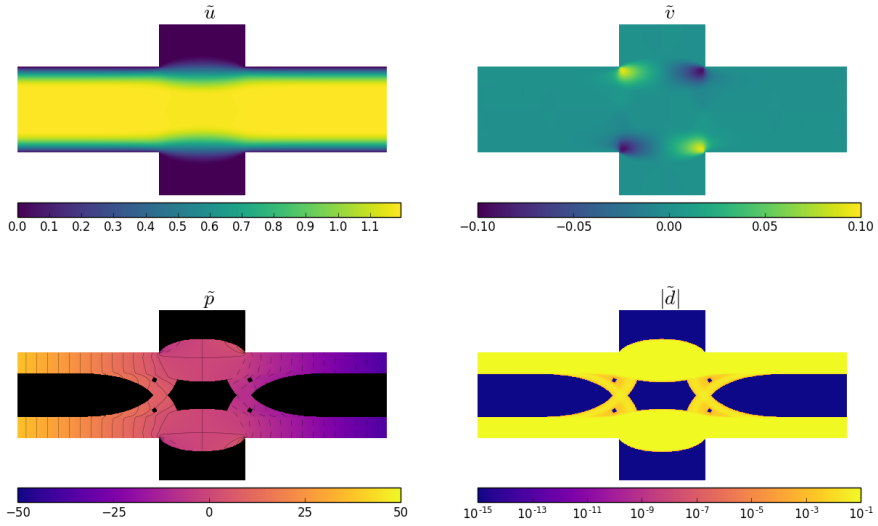

Figure 4.3: Solution computed for $\delta = 0.5$, $h = 2$ and $B = 5$, dimensionless variables.

multiplier, but, still, not in log scale, leading to a less clearer view (in particular in the pseudo-plug region, see below). Two main features appear in this case:

- First, we observe a huge slope of the deformation and of the multiplier in the region of the yield surface; this is visible with a very fast transition (almost a single line) in log scale between 10^{-15} and 10^{-1} at the edge of the dead zone in the cavity, at the horizontal edges of the central disconnected plug and in most of the entry/exit channels. Here, the plastic zone is very clearly seen. This is a sign of a very good quality of the convergence of the AL.

- Second, it is also interesting to note that a pseudo-plug zone [PFM09] can be seen (by looking at the values between $[10^{-5}; 10^{-3}]$) surrounding the disconnected plug located in the center of the domain (see also figure 4.4 for a zoom). Of note, inside this pseudo-plug zone, one can also see four little "square" plugs which are also exhibited in [RGF15; Rou16]. These four plugs are confirmed under mesh refinement (see below).

Let us have a closer look at the plastic zone indicators. The figure 4.4 shows $|\tilde{D}(\tilde{\mathbf{u}})|$, $\tilde{d}$ and their difference, all in the *log scale*. We see that both $|\tilde{D}(\tilde{\mathbf{u}})|$ and $\tilde{d}$ are good indicators of the plastic zones but $\tilde{d}$ is slightly better. This is clearly understood by the structure of the AL for which the plastic threshold is directly used in the computation of $\tilde{d}$ (which is local), whereas $|\tilde{D}(\tilde{\mathbf{u}})|$ is obtained by discrete differentiation of $\tilde{\mathbf{u}}$. Quantitatively, it appears that taking the zone $\{|\tilde{d}| = 10^{-15}\}$ (the machine precision for 0) or an upper level belonging to $[10^{-10}; 10^{-6}]$)

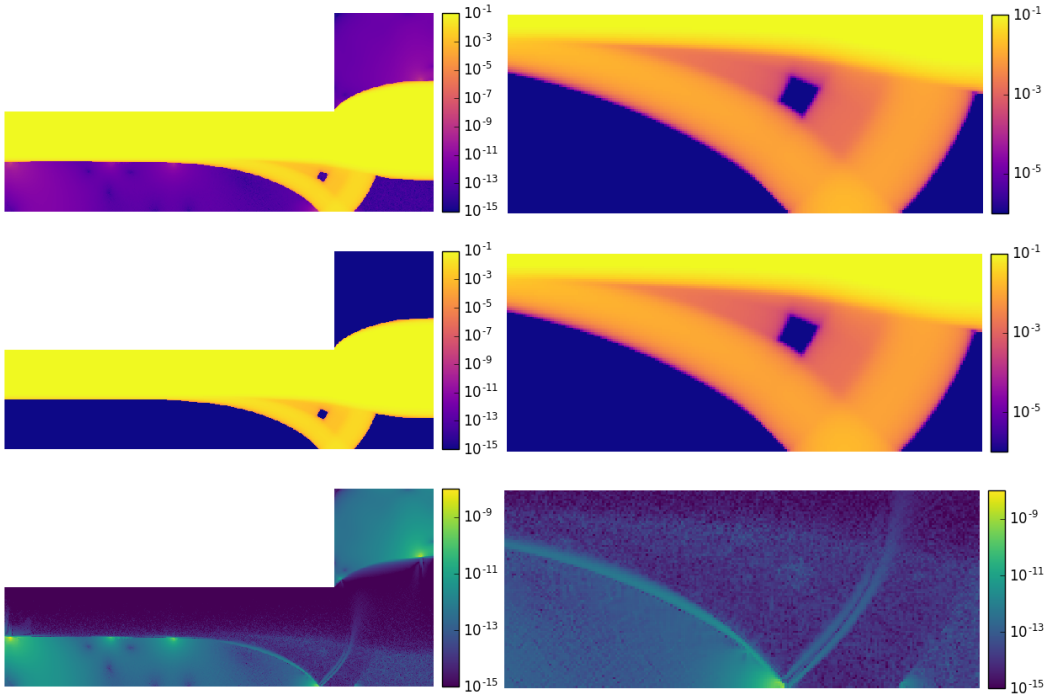

Figure 4.4: Localization of the plastic zone with *log scale* (zoom of fig. 4.3). $\delta = 0.5$, $h = 2$ and $B = 5$. From top to bottom: $|\tilde{D}(\tilde{u})|$, $\tilde{d}$ and the residue $|\tilde{D}(\tilde{u}) - \tilde{d}|$. Left: the whole quarter domain. Right: zoom of Left on the pseudo-plug zone, remark that the colormap is refined between $[10^{-6}; 10^{-1}]$.

to delimit the plastic zone leads to the same results. In the rest of the paper, we will thus present the $|\tilde{d}|$ fields (instead of $|\tilde{D}(\tilde{u})|$) of our various simulations to localize the plastic zones.

Figure 4.5 shows the evolution of the plastic zone (defined here as the level $|\tilde{d}| = 10^{-10}$) when the mesh is refined. One can observe that these lines are very close to one another. Moreover, the volume of the plug zone seems to increase monotonically and converges to a limit plug. This convergence is another sign of the well-posedness of the algorithm and discretization. The fact that one needs to zoom to point out these minor differences invites us to use the less refined mesh. In the rest of the paper, otherwise stated, we set the length of a cell such that there are 600 points in a section of cavity. This condition ensures a dramatic reduction of CPU time without a significant loss of accuracy.

Of note, the meshes used in the figure 4.5 have from 1.25 to 7.8 $\cdot 10^6$ cells and the CPU times were between 5h30 and 32h30. Since the literature is very scarce in terms of CPU times information for such simulations, the interested reader can find in [MV17] the computation

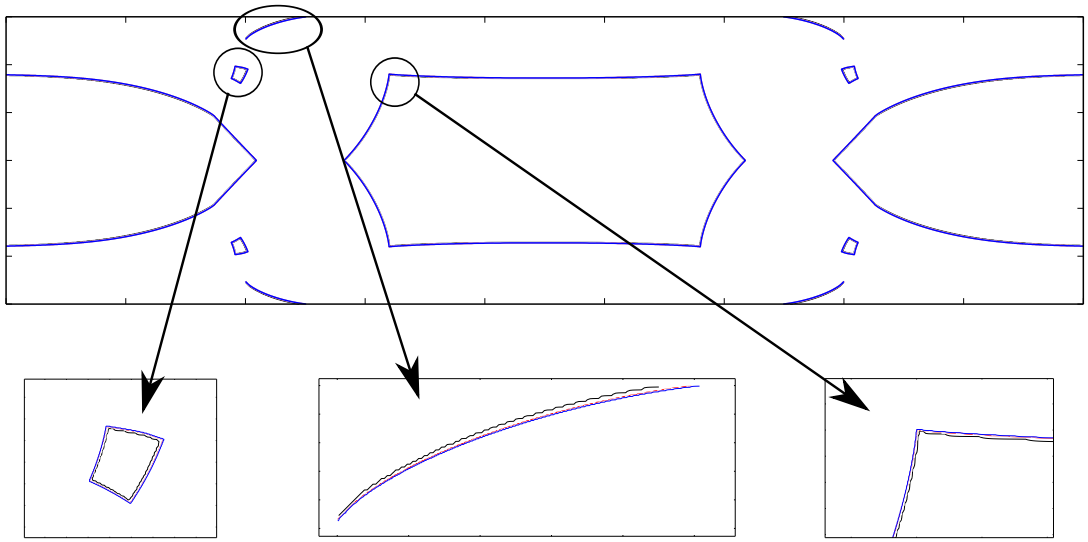

Figure 4.5: Mesh refinement study: $\delta = 1/5$, $h = 6/5$ and $B = 20$. Contour $|\tilde{d}| = 10^{-10}$ for $\Delta\tilde{x} = 4 \cdot 10^{-3}$ (black), $\Delta\tilde{x} = 2 \cdot 10^{-3}$ (red) and $\Delta\tilde{x} = 1.6 \cdot 10^{-3}$ (blue).

times of a wide range of simulations done in this paper, which can be used for future comparisons.

4.3 DIFFERENT PLASTIC ZONES

Typical plastic domains are displayed in figure 4.6: we highlight the evolution of the plastic zones when B increases. When B is low, we observe a break in the plug zone whereas, when B is high, the whole middle of the domain moves rigidly. In between (for instance $B = 5$, in Magenta on figure 4.6), little patches of rigid material appear in the pseudo-plug zone, and they increase with B to finally fusion within the continuous plug zone in the center of the channel.

In the case of "long" cavities as presented in Figure 4.7 and as in the configuration of [LPC15], where the dead zone at the back of the cavity is disconnected, one can measure the horizontal length of the deadzone, denoted as L_d (see Fig. 4.7). We plotted L_d as a function of the Bingham number. Figure 4.8 tends to show that this dependence follows a linear law in log-log coordinates. Another striking result of this work is the to-date most detailed structure of the pseudo-plugs exhibited by simulation: Figure 4.9 shows the full strain rate fields to better see these pseudo-plugs. We believe that further research both theoretically and numerically deserve to be done to better explain these structures. For all the details of methods and results, the reader is referred to the full article [MV17].

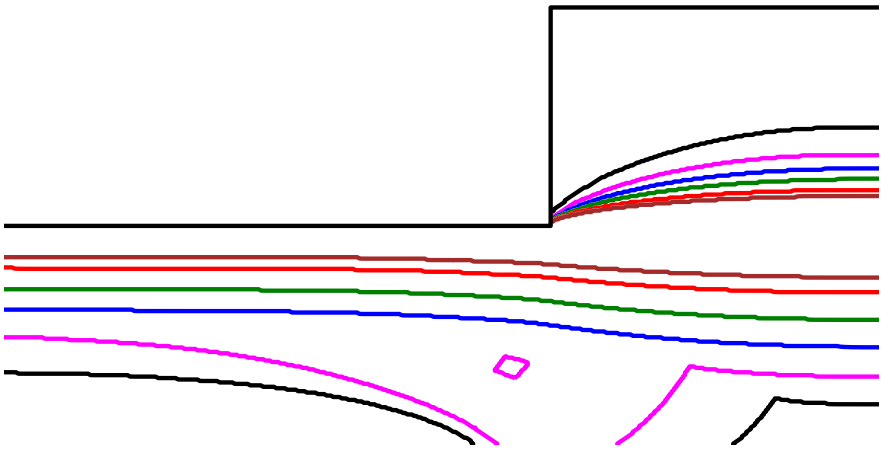

Figure 4.6: Different plastic zones. $\delta = 0.5$, $h = 1$ and various B: 2 (Black), 5 (Magenta), 10 (Blue), 20 (Green), 50 (Red) and 100 (Brown).

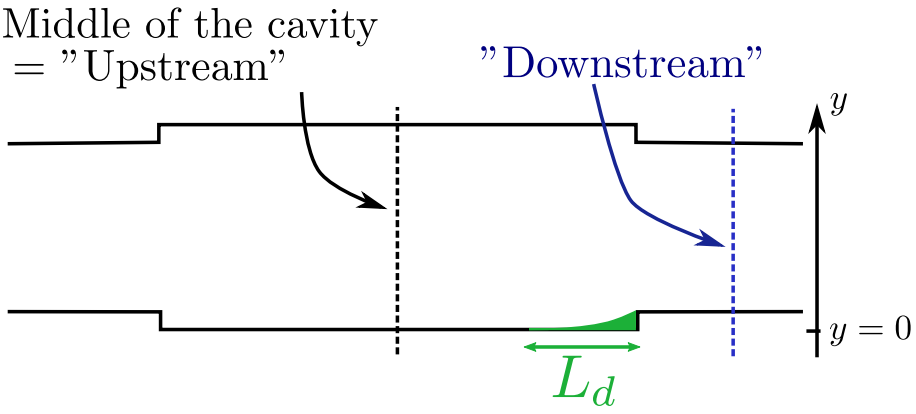

Figure 4.7: A typical aspect ratio for longer channels. A typical dead zone in the configuration of [LPC15] is shown in green at the corner of the exit step and gives the definition of the length of the dead zone L_d.

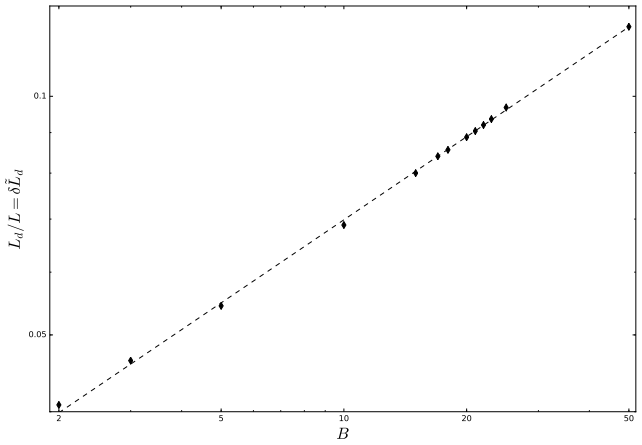

Figure 4.8: Length of the dead zone (scaled by L) as a function of B in log-log scale (for $L = 25$ and $\delta = 1/5$). A linear fit is done as a guide for the eye and the slope is 0.346.

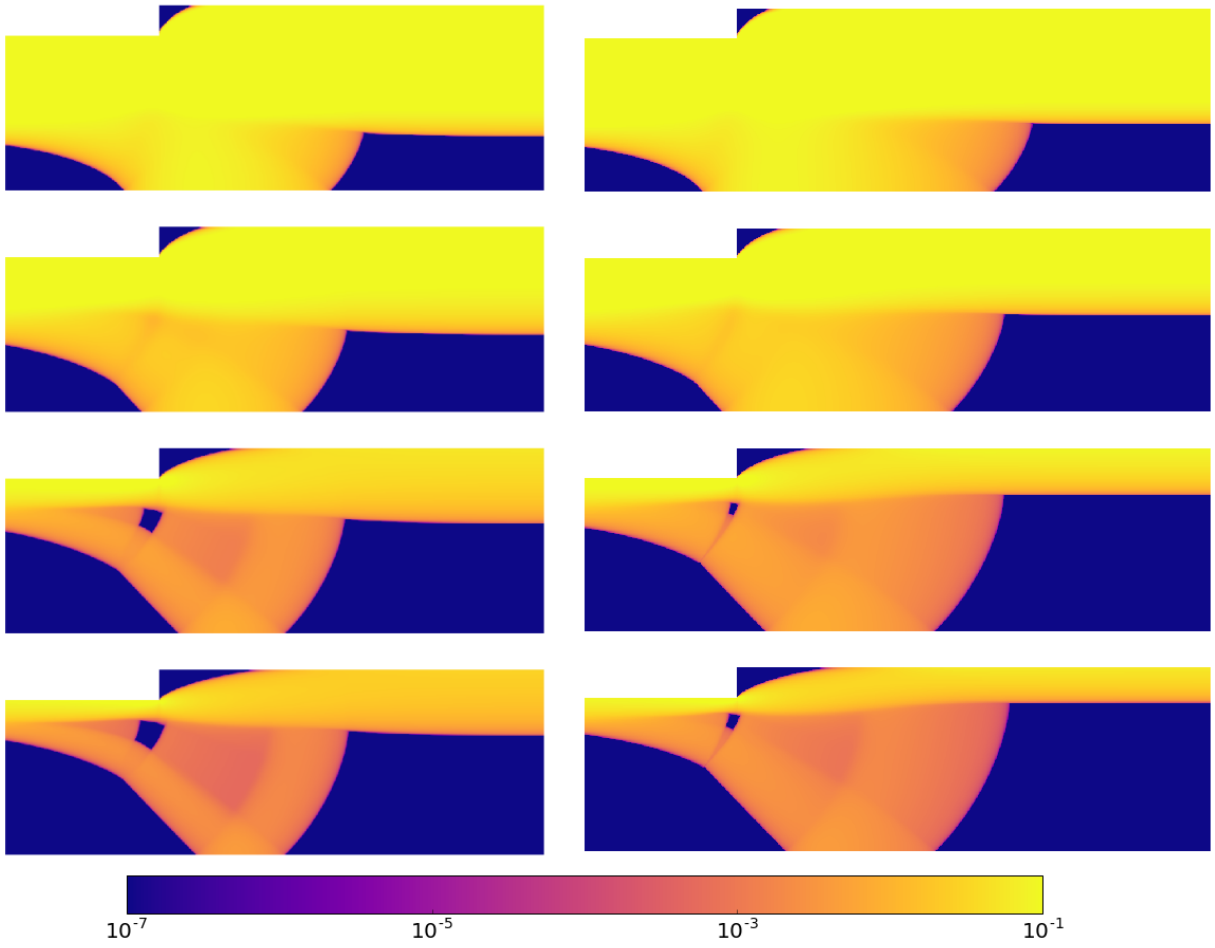

Figure 4.9: $|D(\mathbf{u})|$ for $H = 1$, $D = 5$ and $L = 25$ (Left) or $L = 60$ (Right). From top to bottom: $B = 2$, 5, 25 and 50.

4.4 FUTURE DIRECTIONS OF RESEARCH FOR THE PART I

Several aspects of the numerical modelling of viscoplastic materials need long term research efforts.

Concerning the derivation of the models themselves there is still much to be done, both for full tensorial description and integrated versions. As a matter of fact, constructing rheological laws for complex fluids – even if much progress was made – is still a challenge today: physical experiments are often delicate to perform and ensuring a general uniform framework of their interpretation is not necessarily ensured. Indeed all material features are not always understood and some hidden characters are difficult to track. A typical example is the presence of elasticity in viscoplastic materials. Another illustration is the fact that recent laws such as the $\mu(I)$ rheology [JFP06] (which proves very successful in several particular situations) were derived in simple shear configurations which do not describe necessarily all the rheological characteristics of these materials.
Then, assuming that we have a good tensorial constitutive law in 3D, the derivation of a consistent integrated version to obtain more tractable shallow formulations is still a work of its own.
The design of rheological models for geophysical applications which are thermodynamically consistent is still open and very active.

Mathematically, for such models and in full generality, well-posedness, qualitative properties, *etc* are still mostly open and also a field of intense activity. From the numerical point of view many paths need to be explored: just to name two of them, one can mention the design of *consistent* schemes for such models – is not necessarily straightforward – and the computation times of rheology's solvers need and can be improved.
Concerning "Bingham solvers", very recently were proposed several unregularized approaches for the resolution of the Bingham problem trying to replace or/and improve the Augmented Lagrangian. For instance Treskatis et al. [TMP16] present an acceleration of the AL thanks to a FISTA method. Applying the Newton method, hoping for super-linear convergence, directly to the original Bingham problem leads to a singular Jacobian matrix. In a promising article, Saramito [Sar16] treats directly this singularity and preserve quadratic convergence. Note however that this approach treats only the *scalar* Bingham problem and the extension to the vector version (2D or 3D) is not done. See the very recent [SW17] for a review.

Among other natural sequels of the present works will be: (i) orientation to HPC with the study of the implementation of such approaches to parallel environments (CPU/GPU), (ii) extensive testing of the 2D schemes on laboratory experiments (like e. g. the numerous

works of Christophe Ancey [Anc07; AC09; AEA12; AAE12]) to see if they perform better than their 1D counterparts and to study specificities of this 2D tensorial law for which little is known (iii) the extension to multilayer models where one takes into account viscoplastic and Newtonian material. This is typically the case for submarine avalanches.

A better understanding of the pseudo-plugs region as mentioned in Chapter 4 and in interaction with physical experiments is also planned. This is included in a project we proposed for 2017-2019 which was awarded a CNRS Grant in the "Défi Interdisciplinaire" InFIniti [Vig+18]. The team is composed of Arthur Marly (UMPA, ENS de Lyon), Guillaume Chambon (IRSTEA Grenoble), Li-Hua Luu, Pierre Philippe (IRSTEA Aix) and I am the principal investigator of this project.

Part II

PDE & STATISTICS FOR MEDICAL DATA

Inverse problems for PDEs. Bayesian methods (SAEM, adaptive SAEM). Metamodel. Kriging. 3D MRI: segmentation, medically controlled preprocessing. Application to Low Grade Glioma.

5

DATA DRIVEN PDE MODELLING IN MEDICINE

With four parameters I can fit an elephant,
and with five I can make him wiggle his trunk.

— John von Neumann [Dys04]

This part deals with the activity done in the **INRIA NUMED** team at UMPA, ENS de Lyon and headed by Emmanuel Grenier.

The **context** is the following: since more than a decade now Emmanuel Grenier has made a lot of connections with Medical Doctors and developed mathematical modelling for medicine in various fields, including stroke and oncology. This leads the NUMED team to be confronted to a lot of medical data. Their types can be very different from one field to another and we are more concerned here with 3D images like Magnetic resonance imaging (MRI) (with different sequences: T1, T2, Flair, etc).

One of the characteristics of such data is that one or several variables are repeatedly measured over long periods of time (so called *longitudinal data*) for a lot of individuals (several dozens or several hundreds, depending on the study). Of note, even if a lot of individuals are under observation, the number of samples per individual can be quite sparse (let say 3 to 5 sample times) – e. g. this can be (unfortunately) attributed to cost or availability of data acquisition.
Remark that there are other INRIA teams who work on data assimilation in medicine: REO, ASCLEPIOS, MONC to name a few. Many of them are composed of more than ten or 15 members and have a long expertise in developing very sophisticated mechanical / electrophysiological models (e. g. for cardiac modelling or oncology). Being a much smaller team of five members NUMED try to singularize from these other teams by focusing more on population approaches as described below.

From the general viewpoint, our objectives in NUMED are to:

- build PDE models (assuming that ODE are not sufficient) for the considered phenomena; we try to keep these models as parsimonious in parameters as possible;
- validate these models by studying their ability to fit the observed data and forecast the evolution in time of the phenomena.

This leads us to the well-known class of *inverse problems* to determine the "best parameters" of the PDE to fit the data. Roughly, methods for inverse problems can be divided in (i) "*individual*" (often deterministic) parameters estimation and (ii) "*population*" statistical inverse problem. In the former, each individual is considered independently from the others and a (deterministic) method is used to fit the parameters according to the data: one can use very simple methods like least squares or more sophisticated ones like the *adjoint state* method [Lio71; GP00]. There is a huge literature on individual inverse problem methods, see e. g. the books [BK89; Isa06; Tar05].
In the latter, data from all individuals are gathered and the method uses this whole "population" to determine the probability density function of the parameters, turning the problem into a statistical one, see e. g. [KS05; Stu10]. To do so, Bayesian methods are particularly suited and their use has exploded in recent years.

SAEM is heavily used in the pharmaceutical industry thanks to more than a decade of Lavielle's dissemination. Marc then launched a start-up of INRIA called Lixoft in 2011. It distributes the Monolix software which implements cutting edge SAEM algorithms.

Historically, NUMED has used and helped developing a specific kind of Bayesian method, namely the SAEM method of Marc Lavielle and coworkers [DLM99; KL05] to perform the parameters estimation of its models. Note that, as a population approach, SAEM is very adapted to our problems since:

- we have "a lot" of individuals in our data (so a deterministic inverse problem for each of them can become very costly)
- but some individuals have very sparse sampling in time (sometimes 1 or 2 time observations only), which can lead to poor (or impossible) estimation via an individual inverse problem.

The strength of the population approach is that using the global knowledge of all individuals, it can infer some information (of course in a probability sense) on a given individual which has possibly few samples.
Note also that all the previous studies in NUMED where done on ODEs or systems of ODEs. More generally, the literature on SAEM, before the early 2010's showed a lot of successful methodological developments and applications on

- ODEs or systems of ODEs [LM07; Sno+10],
- Stochastic DEs [DS08; DFS10]

but nothing was done with PDEs. Since my arrival in Lyon (Sept. 2008), one of my contributions in NUMED was the extension of SAEM to its use with PDEs. Our long term research program is to couple SAEM, PDEs and 3D images data.

As it is well known in the literature (and not only for the SAEM community but more generally for all Bayesian-like approaches), the bottleneck is the individual cost of one direct PDE problem resolution, which can be very expensive. As a matter of fact, Bayesian methods use a huge number (let us say 10^5 - 10^6) of evaluations of one direct problem leading to impossible overall computation times for PDEs.

Our contributions in the field of SAEM is twofold: *first*, we implemented for the first time SAEM estimation with PDE, thanks to the use of so called PDE metamodels which approximate the original model at a cheaper cost [GLV14]. This is based on the old and simple idea of building an *offline* "grid" of precomputed solutions of the original PDE model for certain values of the input parameters constituting this grid. This was modest but, still, it was a first step to *effective* use of SAEM with PDEs. We apply that to a typical reaction-diffusion equation, the Fisher-KPP model.
The approach was then taken with interest by Adeline Samson (another renown specialist of SAEM) and coworkers, who perform a theoretical study in [BBS16] to derive a rigorous error control of the computed parameters, as a function of the error induced by the metamodel (w.r.t. the original model). The grid metamodel was here taken as a kriging grid as suggested in [GLV14].

Actually, we also described in [GLV14] the road map subject of the next paragraph: [Gre+18].

A bit more subtle was *secondly* our implementation of a metamodel which is not built offline, but which is refined ***online*** during the SAEM algorithm itself. We implement and show the proof-of-concept in [Gre+18], where the so called KSAEM, a kriged evolutive metamodel version of SAEM was illustrated.

Before going into the details of these works, we can make a few preliminary remarks. Even if based on simple or usual ideas, the complete implementations of such algorithms were *original in this context* and require a significant amount of time in terms of development of all the codes. Especially when we manipulate 3D MRI data in which we need to make medically controlled analyses and treatments before plugging them in the parameters estimation procedure. I was instrumental in the core implementation of all these tools, their prototypes and the "production" versions. These were done mixing various computing languages depending on the necessities: Fortran, C/C++, Python, FreeFem++, Matlab and MPI for parallel tasks. Furthermore, these practical developments – driven by real applications with Med-

ical Doctors – leads to some theoretical original questions which are still open. For instance, can we prove rigorously the convergence of the coupling between SAEM and an evolving metamodel online ?

5.1 INTRODUCTION TO POPULATION APPROACH

Here "model" needs to be understood in the Statistical *sense.*

[1]We are concerned with the parametrization of models of the form

$$y = f(t, Z) + \varepsilon$$

While here another sense of "model" is used.

where y is the observable, t is the time of observation, Z the individual parameters and ε is a measurement error term. The model f is referred to as a "black box" model. It may be a system of ordinary differential equations, of partial differential equations, or a multi-agents system, or any combination of these model types. We will assume that it is costly, namely that its evaluation is very long. For instance one single evaluation of a reaction-diffusion equation in a complex geometry may last a few minutes or even a few hours if the coefficients are large or small, leading to a stiff behavior.

In these works, we focus on population parametrization from observations of f along time among N individuals. From these repeated longitudinal data, we search the distribution of the parameters Z in that given population of individuals. To take into account the various sources of variabilities (inter-individual and intra-individual variabilities), we use a non-linear mixed effect model.

The non-linear mixed effect model links the j-th measure, $j = 1, \dots, N_i$, y_{ij} at times t_{ij} for individual $i = 1, \dots, N$ with the black box model:

$$y_{ij} = f(t_{ij}, Z_i) + \varepsilon_{ij}, \tag{5.1}$$

where Z_i are p-vectors of the random individual parameters, ε_{ij} are random measurement errors, independent of the individual parameters Z_i. The errors ε_{ij} are assumed to be Gaussian

$$\varepsilon_{ij} \sim_{iid} \mathcal{N}(0, \sigma_\varepsilon^2). \tag{5.2}$$

The main difficulty is to identify the individual parameters Z_i, which are unknown and should be inferred from the observations. Identifying (or estimating) directly the Z_i from the data (y_{ij}) might be difficult when N_i is small, typically smaller or of the same order than p, the length of Z_i. To avoid this problem of dimension, we assume that the parameters Z_i are random and follow a given probability law determined by what we call later on population parameters. These population parameters are unknown and the objective is to identify

1 The presentation is adapted from but follows closely [Gre+18]; Section 5.3 is naturally inserted to sum up results linked to [GLV14].

them rather than all the Z_i. In the following, we assume that the parameters follow a Gaussian distribution

$$Z_i \sim_{iid} \mathcal{N}(\mu, \Omega), \tag{5.3}$$

where μ is a p-vector of expectation and Ω is a $p \times p$ matrix of covariance. The population parameters are $(\mu, \Omega, \sigma_\varepsilon^2)$.

We then look for parameter mean μ and variances Ω, σ_ε^2 which maximize the likelihood of the observations (y_{ij}). Once we have an estimation of μ and Ω from the observations (y_{ij}), we may want to estimate or approximate the individual variables Z_i which are more likely given the observations for individual i and the distribution of individual parameters in the population $\mathcal{N}(\mu, \Omega)$.

SAEM algorithm is a classical approach to evaluate and estimate numerically the population parameters μ, Ω and σ_ε^2 from a non-linear mixed effect model [KL05]. This algorithm requires a large number of evaluations of the model f, typically a few hundreds of thousands, or a few millions. If the model is costly, the total time of SAEM algorithm may be huge, of a few days or even months.

A natural way to make SAEM doable with costly f is to replace it by an "approximate" model which in turn is much faster to compute. Such approximation is called *metamodel* in the following, and we assume that under an appropriate asymptotic procedure it converges to the original model f. To build such a metamodel, there exist numerous methods: discretizing the parameters space and using classical interpolation, reduced basis methods, polynomial chaos, etc. [SVE08; HL11; PR06; MN09]
For instance, the first attempt of using such metamodel with SAEM to decrease its computation time was presented in [GLV14]: parameter space (Z) is discretized with an inhomogeneous grid adapted to the variations of f and the metamodel is given by a linear interpolation made on this fixed grid. This general method was illustrated on a reaction-diffusion partial differential equation showing that the SAEM computation time can be lowered from 23 days to 26 minutes. However, this method is still subject to the classical "curse of dimensionality": one can reasonably only operate with a maximum of 5 or 6 parameters for the black box model.

One way to improve this problem is to use a more parsimonious interpolation such as kriging. Indeed, the kriging approach (where f is thought as the realization of a Gaussian process [Sac+89; SWN03; FLS05]) is less sensitive to dimension. Interestingly, kriging to build a fixed grid used by SAEM was later studied in [BBS16]. They proved the convergence of the SAEM algorithm to the maximum likelihood of an approximate non-linear mixed effect model. It is also shown theoretically that the error produced by the kriging approximation can be controlled depending on the quality of the kriging grid. Therefore in practice, for a costly black box model f, we have to choose

a kriging approximation with sufficient accuracy (depending on the available computational power). However, it is more delicate to refine the mesh where the model really changes since it is not possible to rapidly identify where f has sharp transitions.

But we need to keep in mind that we deal here with a coupling between SAEM and the metamodel, i.e. that actually, this metamodel only needs to be precise in the regions of the parameters space which will be explored by the SAEM iterations. Based on this, [GLV14] already proposed the methodology of a metamodel which is refined during the SAEM algorithm itself, meaning that more points are added in the "grid" (or basis) of the metamodel dynamically.
The aim of [Gre+18] is thus to describe precisely and implement this idea of interactive coupling between the SAEM and the metamodel building based on the kriging approach. The expected gain of this new algorithm, called KSAEM for "Kriging SAEM", is the following:

- since the metamodel is dynamic, the offline step (i.e. building the metamodel before SAEM) does not need to be very precise: as a consequence the initial metamodel is obtained with only a few calls to the resolution of f;
- then during the SAEM (online step), the metamodel will be refined, only if one detects that the precision is not sufficient (in a sense defined later): as a consequence few other costly resolutions of f will be done, but most of the time only fast interpolations on the existing basis will be used;
- overall, the total number, say n_c, of costly evaluations of f for this SAEM run is lower than a precise offline building of a metamodel.

A remark must be given here: comparison of the global computation cost with a fixed grid approach like in [GLV14; BBS16], cannot be done directly on n_c since a fixed grid is done once for all SAEM runs, whereas a dynamic metamodel is built at each use of a KSAEM algorithm. For instance, if a metamodel is used many times on various data sets, it could be better to use a fixed grid approach than a dynamic grid approach.

In Section 5.2, we recall the problem of maximizing the likelihood of a non-linear mixed model and the classical SAEM algorithm. In Section 5.3, we give a synthesis of the fixed metamodel of [GLV14]. While in Section 5.4, we present the version where the metamodel is refined along the SAEM algorithm of [Gre+18] (we start by quickly describing the kriging and then introduce the new algorithm called KSAEM).

5.2 MAXIMIZATION OF THE LIKELIHOOD AND EXACT SAEM ALGORITHM

This section is devoted to a brief presentation of the likelihood in the case of non-linear mixed effects models and the standard SAEM algorithm that allows to compute the maximum of the likelihood, providing an evaluation of the population parameters.

5.2.1 *Non-linear mixed effects model*

Let us start with the ideal case when enough data are available for the i^{th} individual. Then the individual parameters Z_i can be estimated maximizing the Gaussian density of the observations $(y_{ij})_j$ given the (hidden) individual parameter Z_i (Gaussian error (5.2)):

$$p\Big((y_{ij})_j|Z_i;\sigma_\varepsilon^2\Big) = \frac{1}{\sigma_\varepsilon^{N_i}\sqrt{2\pi}^{N_i}}\exp\Big(-\frac{1}{2\sigma_\varepsilon^2}\sum_{j=1}^{N_i}(y_{ij}-f(t_{ij},Z_i))^2\Big).$$

This is equivalent to the classical least squares minimization procedure (nonlinear regression)

$$\hat{Z}_i = \operatorname{argmin}\sum_{j=1}^{N_i}(y_{ij}-f(t_{ij},Z_i))^2.$$

However, in many interesting cases, only few data are collected per individual, and the non-linear regression procedure is useless. An alternative is to pool all the data together, and to calibrate and estimate the distribution of individual parameters in the whole population, assuming they have a Gaussian distribution through the non-linear mixed effect model. Individual parameters are recovered in a second part.

Let us denote $\theta = (\mu, \Omega, \sigma_\varepsilon^2)$ the population parameters. The density of the individual parameters Z_i is simply

$$p\Big(Z_i;\theta\Big) = \frac{1}{\sqrt{(2\pi)^p\det(\Omega)}}\exp\Big(-\frac{1}{2}(Z_i-\mu)^t\Omega^{-1}(Z_i-\mu)\Big)$$

Hence for individual i, the joint density of observations $(y_{ij})_j$ and individual parameters Z_i is

$$p\Big((y_{ij})_j,Z_i;\theta\Big) = \frac{1}{\sqrt{(2\pi)^p\det(\Omega)}}e^{-\frac{1}{2}(Z_i-\mu)^t\Omega^{-1}(Z_i-\mu)}\frac{1}{\sigma_\varepsilon^{N_i}\sqrt{2\pi}^{N_i}}e^{-\frac{1}{2\sigma_\varepsilon^2}\sum_{j=1}^{N_i}(y_{ij}-f(t_{ij},Z_i))^2}$$

Assuming the N individuals to be independent, the density of the complete population variables $(y_{ij},Z_i)_{ij}$ is

$$p\Big((y_{ij})_{ij},(Z_i)_i;\theta\Big) = \Pi_{i=1}^N p\Big((y_{ij})_j,Z_i;\theta\Big)$$

As $(Z_i)_i$ are hidden variables, the density of the observations $(y_{ij})_{ij}$ given the parameters θ is the integral of $p\Big((y_{ij})_{ij},(Z_i)_i;\theta\Big)$ with respect to Z_i:

$$g\Big((y_{ij})_{ij};\theta\Big) = \int p\Big((y_{ij})_{ij},(Z_i)_i;\theta\Big)\,dZ_1...dZ_N. \tag{5.4}$$

With this expression we can define the log likelihood of θ to be

$$l(\theta) = \log g\Big((y_{ij})_{ij};\theta\Big).$$

The main problem is now to maximize this likelihood and to compute

$$\theta_\star = \text{argmax}_\theta\ l(\theta). \tag{5.5}$$

This problem is very delicate since the evaluation of a single value of l requires the evaluation of a multidimensional integral, which in turn requires numerous evaluations of our costly black box model. As stated, this is out of reach even for simple models. Several methods and algorithms have been proposed to solve this optimization problem. We focus in this paper on a stochastic version of the well-known EM algorithm [DLR77], namely the SAEM algorithm [KL05].

5.2.2 *SAEM algorithm*

The EM algorithm relies on a series of acute ideas and on two main iterative steps: the expectation step (E) which computes a conditional expectation and the maximization step (M) which maximizes the conditional expectation with respect to the parameters.

At iteration k of the EM algorithm, given the current value of the parameter θ_k, we proceed in two steps:

1. an expectation step computes, by "doubling" the parameter θ, the quantity

$$\begin{aligned} Q(\theta|\theta_k) &= \int \log p\Big((y_{ij})_{ij},(Z_i)_i;\theta\Big)\,p\Big((Z_i)_i|(y_{ij})_j;\theta_k\Big)\,dZ_1...dZ_N \\ &= \mathbb{E}\Big(\log p\Big((y_{ij})_{ij},(Z_i)_i;\theta\Big)|(y_{ij})_{ij};\theta_k\Big), \end{aligned} \tag{5.6}$$

   where $p\Big((Z_i)_i|(y_{ij})_{ij};\theta_k\Big)$ is the conditional density of the hidden variables Z_i given the observations $(y_{ij})_{ij}$;

$$p\Big((Z_i)_i|(y_{ij})_{ij};\theta_k\Big) = \frac{p\Big((y_{ij})_{ij},Z_i;\theta_k\Big)}{g((y_{ij})_{ij};\theta_k)} \tag{5.7}$$

   and g is the renormalization factor (the likelihood) defined by (5.4).

2. a maximization step updates the current value of the parameter

$$\theta_{k+1} = \text{argmax}_\theta \; Q(\theta|\theta_k). \tag{5.8}$$

It turns out that this maximization problem is much easier to compute since the integral in (5.6) is taken with respect to a fixed density (dependent of θ_k) which can be approximated through Monte Carlo procedure. Moreover, thanks to the log in the integrand, there is no exponential in function Q, which is simply bilinear in θ. The maximization procedure is, therefore, completely explicit provided we know how to compute the integral with respect to $dz_1 ... dz_N$.

To approximate this integral the EM algorithm is coupled to a Monte Carlo Markov Chain method [KL05]. A Metropolis-Hastings algorithm provides a sequence of Markov chains $(z_i^{kl})_l$ with stationary distribution $p((z_i)_i|(y_{ij})_{ij};\theta_k)$. This is easily done using (5.7). Then $Q(\theta|\theta_k)$ could be approximated by a Monte Carlo empirical mean using a large sample $((z_i^{krl})_i)_{r=1,\dots,R_l}$ for L independent chains $l = 1, \dots L$. This leads to the Monte Carlo EM [WT90].

$$\begin{aligned}
\tilde{Q}(\theta|\theta_k) \;=\; & \frac{1}{L}\sum_l \frac{1}{R_l}\sum_r \log p\Big((y_{ij})_{ij},(z_i^{krl})_i;\theta\Big) = -\frac{N}{2}\log((2\pi)^p \det(\Omega)) \\
& -\frac{1}{2}\sum_{i=1}^N N_i \log(2\pi\sigma_\varepsilon) - \frac{1}{L}\sum_l \frac{1}{R_l}\sum_i \frac{1}{2}(z_i^{kl}-\mu)^t\Omega^{-1}(z_i^{krl}-\mu) \\
& -\frac{1}{L}\sum_l \frac{1}{R_l}\sum_i\sum_j \frac{(y_{ij}-f(t_{ij},z_i^{krl}))^2}{2\sigma_\varepsilon^2}.
\end{aligned}$$

Note that, as stated previously, the maximization step (5.8) is completely explicit.

Note that the Monte Carlo approximation $\tilde{Q}(\theta|\theta_k)$ is somehow not adequate since we need to simulate a large number of z_i^{kl} to get an accurate evaluation of $\tilde{Q}$. However as the EM algorithm goes on, θ_k converges, hence $\tilde{Q}(\theta|\theta_k)$ will be close to $\tilde{Q}(\theta|\theta_{k-1})$. To take advantage of this convergence, the idea of SAEM [DLM99] is to introduce Q_k defined iteratively, using only one realization z_i^{kl} per chain by

$$Q_k = (1-\gamma_k)Q_{k-1} + \frac{1}{L}\sum_l \gamma_k \log p\Big((y_{ij})_{ij},(z_i^{kl})_i;\theta\Big)$$

where γ_k goes slowly to 0, and where z_i^{kl} is one realization of z_i under the conditional distribution $p((z_i)_i|(y_{ij})_{ij};\theta_k)$ for chain $l = 1, \dots, L$. Condition on γ_k are the following: $\sum_k \gamma_k^2 < \infty$ and $\sum_k \gamma_k = \infty$. A usual choice is thus $\gamma_k = \frac{1}{k^c}$ with $c \in]1/2, 1[$.

[DLM99] and [KL05] prove the convergence of the sequence θ_k towards the maximum of the likelihood g, under smoothness assumptions on the likelihood function.

5.3 SAEM WITH A PREDEFINED METAMODEL (SIMPLE GRID)

In this section, we deal with a speed-up of SAEM by changing the black-box model f by a predefined one f^{app}, which is an approximation of f but much faster to compute. This was the object of [GLV14] which is here summarized.

The idea is just to discretize the parameters space of which f is dependent and for each set of discrete parameters θ, computing and storing the associated solution $f(.;\theta)$ in a database (called a "grid" which is thus built offline). Then, when one needs to evaluate $f(.;\theta_k)$ for a certain θ_k in the SAEM (i.e. online), we just make an interpolation in the grid to obtain $f^{app}(.;\theta_k)$. Of course there exist a lot of sophisticated methods to build such a f^{app}: reduced basis, POD, etc. Since we wanted to make a proof of concept in the context of SAEM and taking into account the workforce, we remain very basic by implementing only an interpolation strategy.

However, we try to revisit the interpolation procedure by considering several optimizations:

- we keep a structured grid to have fast interpolation procedure;
- we use not only homogeneous grids but implement adaptive structured refinement of the parameters space (using quadtree, octree, etc like structures) based on the study of high variations of f;
- the building of this database is implemented in a parallel way and the tasks being essentially independent, we obtain a high parallel efficiency.

The procedure is very general and any kind of model can be easily plugged in these codes.

In [GLV14] we also discuss various ways to make the adaptive refinement depending on the regularity of f. In brief, due to the classical "curse of dimensionality", this kind of approach is limited to 5 or 6 parameters for the model f, in the general case. This is a few number of parameters, but this is totally in line with the NUMED motto: "Keep as few parameters as possible in your model".

We applied these tools on the estimation of the 1D KPP reaction diffusion equation:

$$\partial_t u - \nabla.(D\nabla u) = Ru(1-u), \tag{5.9}$$

where $u(x)$ is the unknown concentration (assumed to be initially a compact support function, for instance), D the diffusion coefficient

and R the reaction rate. These equations are posed in a domain Δ with Neumann boundary conditions. Note that the geometry of the domain Δ can be rather complex (e.g. when u is the density of tumor cells in the brain). Initially the support of u is very small and located at some point $x_0 \in \Delta$. Therefore we may assume that

$$u(T_0, x) = \alpha 1_{|x-x_0|\leqslant\varepsilon}, \tag{5.10}$$

for some time T_0 (in the past). It is well known that for (5.9)-(5.10), there exists a propagation front (separating zones where $u \equiv 1$ and zones where $u \ll 1$). The size of the invaded zone (= the zone where u is close to 1) is defined as

$$S(t) = \int_\Delta u(t,x)dx.$$

We assume that we have data from a population of individuals at various times $t_1, ..., t_N$. For an individual, let S_1, ..., S_N be these data. If we want to compare aforementioned KPP model with data, we have to look for solutions of (5.9) with initial data (5.10) such that $S(t_i)$ is close to S_i for $1 \leqslant i \leqslant N$. As a first approximation, α and ε may be fixed to given values (e.g. $\alpha \leqslant 1$, $\varepsilon \ll 1$). It remains to find x_0, D and R : this done with the SAEM algorithm of MONOLIX (MLX).

Note that due to the PDE character of the problem, one can not plug it directly in MLX so we implemented extended Matlab codes that allowed this plugging in the Matlab version of MLX. Along the way, we suggested some improvements which were then included in next versions of MLX by the Lixoft team.

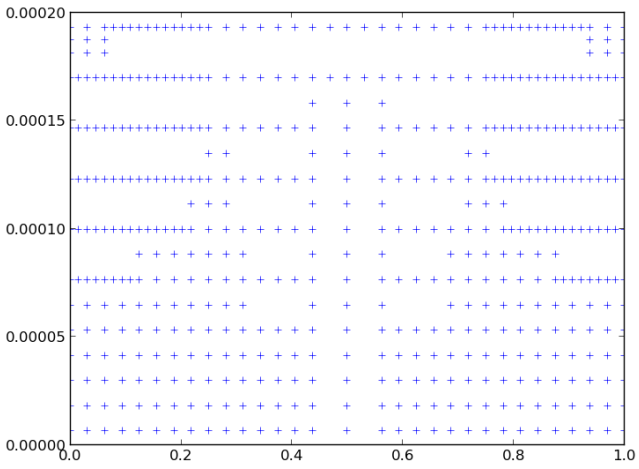

Figure 5.1: An example of an inhomogeneous mesh of the space of parameters (with 500 points). The two parameters are $w = D/R$ and x_0. The mesh is here more refined in zones where the model has strong variations and coarsened in zones where the variations are small.

Note again that even if SAEM works here on times series of the volume $(S(t_i))$, the model f used is not an ODE but a PDE where we keep trace of "spatial" feature via the x_0 parameter. Of course, we use

all the (rigorous) tricks we know on PDE, like qualitative properties, self-similarity, etc to simplify all the computation of f but we keep all the PDE properties of KPP in the parameter estimation. Doing so, we only need to build a "grid" in 2 dimensions (one for x_0 and one for $w = D/R$, see [GLV14] for details) which is given just as an illustrative example in Figure 5.1.

Very briefly, we show in [GLV14] that for this KPP application:

- the total cost of SAEM with an "exact" solving of f is 23 days;
- the total cost of SAEM with f^{app} (on homogeneous grid) is 46 minutes;
- the total cost of SAEM with f^{app} (on inhomogeneous grid of Figure 5.1) is 26 minutes;

with an error of the estimated parameters in the case of f^{app} which is totally acceptable in practice. Given the drastic decrease of the computation time from 23 days to 26 minutes, this validates the interest of the approach. We refer to [GLV14] for the detailed results and discussion.
Note that in an unpublished work (to date, due to lack of "real" experimental data) in collaboration with Pierre Gabriel (Univ. de Versailles), we obtained also good results of present "grid approach" on an age-structured model (of [Gab+12]) for which we also build "synthetic" population.

In the next section, we go back to the complimentary approach where f^{app} is not done once for all and used by SAEM but where f^{app} is changing in the SAEM, according to the explored regions of the parameters space.

5.4 COUPLING KRIGED EVOLUTIVE METAMODEL INSIDE SAEM: KSAEM

As presented before, in the SAEM algorithm, we need to evaluate f only in the Metropolis procedure to find out new sampling points Z_i^{kl}. The same evaluations of the model are then used in the computation of Q_k. This is a costly step since it cannot be parallelized for a given individual Z_i (though all individuals are independent and can be treated in parallel).

A natural idea is thus to replace f by a metamodel f^{app} which is autorefining along the SAEM iterations, this approximation of f being easier and faster to compute. One of the most popular metamodel is Kriging ([Sac+89] and [SWN03]). It is largely used because of its flexibility and because at each point of the domain, it gives a variance of prediction that depends on the distance between the point and

the observations. This approach is detailed in Section 5.4.1. Then we explain how we couple kriging with the SAEM algorithm in Section 5.4.2.

5.4.1 *Kriging in a few words*

Let us recall basic kriging for the function f. We work here at a fixed time t. For simplicity of notations, we will not write the dependence in t in this Section. Assume that in a preliminary step, we have evaluated the function f exactly at several points z_j ($1 \leqslant j \leqslant n$). Let us denote $D = \{z_1, \dots, z_n\}$ this set of points, also called *kriging basis*. Note that the z_j are different from the observations (y_{ij}) and also from the (unknown) random individual parameters Z_j. We want to use the exact values of f at D to approximate f at another point z.
The idea is to suppose that the function f is the realization of a Gaussian process $(\Phi(z))_{z\in S}$, where $S \subset \mathbb{R}^p$, entirely defined by a mean function $m(.)$ and a covariance function $C(.,.)$. In the simplest case, m is assumed to be constant and the covariance function is assumed to be stationary with the form:

$$\forall z, z' \in S, C(\Phi(z), \Phi(z')) = \sigma^2 \prod_{\ell=1}^{p} k(|z_\ell - z'_\ell|; \beta_\ell)$$

where the parameter σ^2 corresponds to the overall variance on the domain S, β_ℓ to the correlation parameter in the ℓth direction and $k(.;.)$ is the correlation function. Different choices can be made for the correlation function depending on the expected regularity of f. For example, if f is highly regular, the Gaussian kernel $k(z, z'; \beta) = \exp(-\frac{|z-z'|^2}{\beta^2})$ is considered.
Given that probabilistic context, the kriging predictor f^{app} and the kriging variance Var^{app} are the expectation and variance of the process $\Phi(z)$ conditional to the exact values of f at points $D = \{z_1, \dots, z_n\}$, i.e.,

$$f^{app}(z) = m + c(z)C^{-1}(f_{1:n} - m\mathbf{1}_n) \quad (5.11)$$

$$Var^{app}(z) = \sigma^2 - c(z)C^{-1}c(z)^t \quad (5.12)$$

where $f_{1:n} = (f(z_j))_{j=1:n}$, $\mathbf{1}_n$ is a vector of ones, $C = (C(z_{j'}, z_j))_{j=1:n;j'=1:n}$ and $c(z) = (C(z, z_j))_{j=1:n}$.
The function $f^{app}(\cdot)$ is then the best approximation of f in the sense that it minimizes the mean quadratic error. The variance may be used as a quality indicator of the approximation of f by f^{app}. Looking carefully at the preceding formulas, it can be observed that the kriging predictor f^{app} is a linear combination of the exact values $(f(z_j))_{j=1:n}$. The weight of each exact value $f(z_j)$ in the prediction at point z strongly depends on $C(z, z_j)$, that is to say on the distance between the two points. The more z_j is close to z, the more influential

is the corresponding observation in the prediction. Moreover, the predictor is strictly interpolating the observations, the variance is null at each observation point and increases with the distance to observation points.

In the following of the manuscript, the parameters m, σ^2 are considered known (respectively equal to 0 and 1) and all the correlation parameters $(\beta_\ell)_{\ell=1:p}$ are considered equal (case of geometric isotropy). Of note, the parameters could be estimated from the observations. Mean m and variance σ^2 are obtained by maximizing the likelihood function. The correlation parameters $(\beta_\ell)_{\ell=1:p}$ are also obtained by maximizing the likelihood function or by minimizing a cross validation criterion. Further, when trend parameters m are estimated, an additional variance is added to Var^{app} that takes into account the additional source of uncertainty coming from estimation procedure. The choice of the correlation function can also be discussed. Here the following Matern kernel has been used for its intermediate regularity ([SWN03]):

$$k(h;\beta) = \left(1 + \sqrt{5}\frac{h}{\beta} + \frac{5}{3}\left(\frac{h}{\beta}\right)^2\right) e^{-\sqrt{5}\frac{h}{\beta}}.$$

5.4.2 *Iterations between SAEM and kriging*

Now that the kriging approximation of f has been recalled, we present the idea of coupling SAEM and the kriging, to obtain a new algorithm called KSAEM.

5.4.2.1 *Iterative kriging*

In some cases, the individual parameters z_i will be concentrated on small areas of parameter space. In these cases we need to have a precise metamodel in these areas, and do not need precise approximations of f away from these areas of interest. Of course if the individual parameters fill the whole parameter space, this observation is useless and what we propose will not improve very much the computation cost.

The main idea is to iteratively improve the metamodel during the iterations of the SAEM algorithm. Each time we need to evaluate our model f at some new candidate point $\tilde{z}$, we approximate this value by our metamodel. Kriging gives an estimation $f^{app,k}(\tilde{z})$ (5.11) based on the current kriging basis $D^k = \{z_1, \dots, z_{n_k}\}$ that contains n_k points and their corresponding exact evaluations $(f(z_j))_{j=1:n_k}$. We also obtain an estimate on the kriging error $Var^k(\tilde{z})$ (5.12).

If the kriging error is small enough, we use $f^{app}(\tilde{z})$ as a good approximation of f. If the kriging error is too large, we directly compute

$f(\tilde{Z})$. This is a long step, but it increases the precision of our evaluation of f not only at $\tilde{Z}$, but also in the neighborhood of $\tilde{Z}$. As we assume that individual parameters Z_i are localized, we hope that this refinement will be used in future steps of SAEM, for larger k. We thus expect that this costly improvement will be used in the forthcoming steps of the algorithm.

As θ_k converges, we have a more and more precise idea of the areas of interest, and we can gradually improve our metamodel in these areas, to decrease the approximation error $f - f^{app}$ in these areas. To decrease this error everywhere is useless since few individual parameters will be outside the areas of interest. To improve the approximation is costly, but hopefully will be focused on small areas, and of limited extent.

5.4.2.2 *KSAEM algorithm*

Let us now describe our algorithm called KSAEM. We choose a precision δ_k which slowly goes to 0. For notation's simplicity, we present the algorithm with one chain $L = 1$.

At iteration k of the SAEM algorithm, given the current value of the parameter θ_k, of the individual parameters $Z_i^{(k-1)}$ and the current kriging basis D^k, we proceed as follows:

- Simulation step: For each individual i, $i = 1, \dots, N$, (this step can be parallelized), we construct a sequence $Z_i^{k(m)}$ for $1 \leqslant m \leqslant M$, for some fixed M, starting from $Z_i^{(k-1)}$ and targeting the distribution $p(Z_i|(y_{ij})_j; \theta_k)$ (5.7), using a Metropolis-Hastings algorithm:
  - We simulate some new parameter $\tilde{Z}$ with a proposal law $q(\tilde{Z}, Z_i^{k(m-1)})$. We will not detail the proposals q here since they are exactly the same as in the classical SAEM algorithm.
  - We approximate $f(t_{ij}, \tilde{Z})$: two cases appear
    - Either $Var^k(\tilde{Z}) < \delta_k$. In this case we approximate $f(t_{ij}, \tilde{Z})$ by $f^{app,k}(t_{ij}, \tilde{Z})$.
    - Or $Var^k(\tilde{Z}) \geqslant \delta_k$. In this case we do compute $f(t_{ij}, \tilde{Z})$ exactly. We add $\tilde{Z}$ and $f(t_{ij}, \tilde{Z})$ to our kriging basis: $D^{k+1} = D^k \cup \{\tilde{Z}\}$ and include them for any further computation. This updates $f^{app,k}$, by progressive inclusion of new points.
  - Using this evaluation of $f(t_{ij}, \tilde{Z})$, we compute the acceptance probability:

$$\alpha(\tilde{Z}, Z_i^{k(m-1)}) = \min\left\{1, \frac{p(\tilde{Z}, (y_{ij})_j|\theta_k)}{p(Z_i^{k(m-1)}, (y_{ij})_j|\theta_k)} \frac{q(Z_i^{k(m-1)}, \tilde{Z})}{q(\tilde{Z}, Z_i^{k(m-1)})}\right\},$$

(5.13)

  - We define $Z_j^{k(m)} = \tilde{Z}$ with probability $\alpha(\tilde{Z}, Z_i^{k(m-1)})$ and else $Z_j^{k(m)} = Z_i^{k(m-1)}$. After M iterations, we set $Z_j^k = Z_i^{k(M)}$.

- Stochastic Approximation step: We update Q_k (5.6)

$$Q_k = (1-\gamma_k)Q_{k-1} + \gamma_k \log p\Big((y_{ij})_{ij}, (Z_i^k)_i; \theta\Big)$$

- Maximization step: Computation of θ_{k+1} as for the usual SAEM algorithm.

In the applications of [Gre+18], we choose a piecewise decreasing profile for δ_k but this choice can be discussed. And its influence can be of importance for the sequential process.

To our knowledge, the complete study of the convergence of KSAEM is still an open problem.

Two applications are done in [Gre+18]: the so called "Theophylline degradation" model which is a classic ODE model benchmark in the SAEM community. And the KPP example described in the previous section (5.3). Again, we show that KSAEM can give good results at a dramatically decreased cost. Note however that the δ_k choice is still a tricky question (see below).

To sum up the two approaches:

The use of genuine SAEM algorithm on complex models leads to very long computation time. A first idea is to replace the evaluation of the complete model by a simple interpolation on a precomputed grid. This approach requires a long offline step, but SAEM is then very fast. This approach will be interesting if the same model must be applied on many different data sets, and if the offline step can take place before the first analysis is necessary.

The other idea is to start from a few precomputed values of the complex model and to complete this basis upon request. In the current approach, the offline step is much faster, and the online step is parsimonious. This approach can be useful if there are only a few different data sets to analyze.
A drawback of the current algorithm is the necessity to choose the various δ_k. If δ_k decreases too fast, useless evaluations of the complete model will lengthen the computation. On the contrary, if δ_k remains too large, the precision of the result of KSAEM will be impaired. To choose optimally δ_k implies to understand the link between the convergence speed of the metamodel and the convergence speed of

SAEM, a question which is widely open. In our two examples, the choice of δ_k has been done after a few trial and error. Note that this question is general to all adaptive Bayesian methods as this was given as an open problem in [LK10, Chap. 10].

Theophylline & KPP

5.5 OTHER ACHIEVEMENTS AND PERSPECTIVES

Recall that in parallel to the previous SAEM studies, we work hard on the 3D MRI management and modelling. As a matter of fact, on the long term we want to use SAEM methodology on complete images. It should be noted that the "treatment" of real clinical images is absolutely not trivial for a number of reasons:

- The machines producing MRI are not standardized so the images are stored in various formats. There exist the supposed DICOM standard but in practice, different brands do not store the data in the same manner, leading to tedious harmonization of the data to be able to read[2] and format time series of the patients; this a well-known but uncured problem when dealing with medical images.
- The volume of data generated for each patient is huge since we deal with 128^3, 256^3 or 512^3 resolution images (in the (x, y, z) directions), leading quickly to TeraBytes of data in 2010-2017.
- For a given patient : at different dates, the data can not be used in a raw form since the position of the patient in the machine is not constant. In other words, one can not compare two different dates directly. One needs to perform the so called "registration" process which recast one date "into the other" to be rigorously compared. Again, this is well-known and there are a lot of methods to do so, but the registration is still a tricky operation due to the fact that sometimes the resolution in z is less than in (x, y) for instance $256^2 \times 30$. This leads to some significant errors when comparing different dates, which obviously propagates in the whole chain of parameters' estimation.
- Inside these images, we need to make the "segmentation" of structures from the disease (e. g. a tumour): this task even in 2017 and for a long time in the general case **can not be performed automatically** by an algorithm due to the intricacies of the structure with ambient media, the measure errors of the machine leading to poor contrast, etc. Of course some medical structures are easy to segment automatically (brain extraction is one of them) but many tumours need to be segmented manually or semi-manually by/with a Medical Doctor.

Note that even MD segmentation is roughly subject to a 10 - 15 % error.

Consequently, since 2010, I spent a significant amount of time learning existing mathematical methods, algorithms and open source libraries (like VTK, ITK (Insight Segmentation and Registration Toolkit)) to perform all these tasks.

2 (yes! even reading the raw data can be cumbersome since they are not stored in the "usual" field)

One of the concrete realizations of such work is the construction of a software called SETIS (for Surface Estimation Tool with Image Segmentation) developed jointly with Ehouarn Maguet in 2013. Ehouarn was recruited in NUMED on a position of INRIA-"Ingénieur Jeune Diplômé" for 12 months and I was the main supervisor of his works. The SETIS software was deposited at the APP (Agence de Protection des Programmes; the European body for protecting authors' and publishers' digital works) under deposit number:

Ehouarn was then straightly recruited by a Grenoble Univ. start-up in Medical Imagery and still works for them to date.

IDDN.FR.001.150013.000.S.A.2014.000.21000

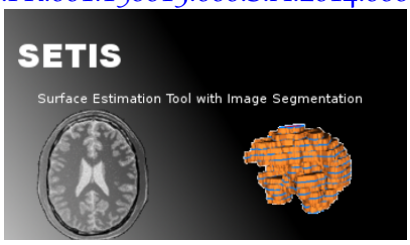

by ENS Lyon and INRIA in the names of E. Maguet and P. Vigneaux in 2014. It is based on the following softwares: PyQT, SimpleITK, GDCM and VTK. It handles MRI, CT scans or other modalities.

In brief, SETIS is used in house but also in collaboration with col-

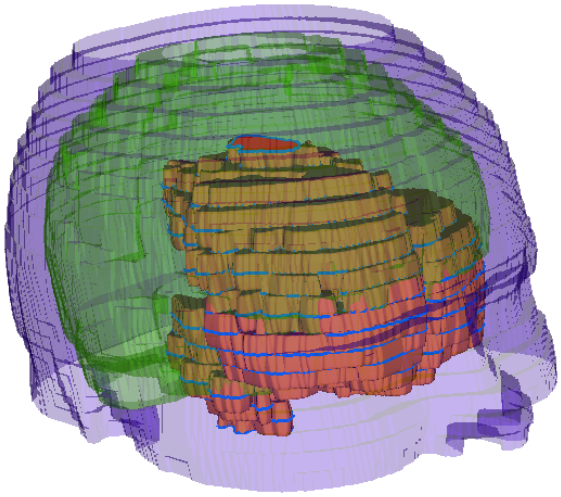

Figure 5.2: Segmentation of a 3D MRI of a brain. Purple: Head of a patient. Green: Brain. Red/Orange: Segmented tumour (LGG) which can touch the brain boundary.

leagues from Oncology. In particular, François Ducray, who is MD & Neuro-Oncologist, is working with NUMED since nearly a decade on the modelling of Low Grade Glioma (LGG). LGG are brain tumours which grow slowly and can be present for decades without being detected. They can sometimes become more aggressive with

a fast growth, in which case they switch to the High Grade Glioma category. Most of present works on 3D MRI are done on LGG and we design SETIS in such a way we can semi-automatically perform the segmentation of LGGs. A typical segmentation task is illustrated in Figure 5.2. To be as ergonomic as possible, SETIS blends various ways to perform the segmentation of the tumour (see Figure 5.3):

1. Algorithmic segmentation of a 2D slice (e. g. via Connected threshold method which starts from a seed and propagates towards pixels of "same color". The seed is placed manually by the user who also can give the color threshold (see the "Seeds" and "Thresholds" boxes on the right of Fig. 5.3). With a few experience, a user can easily give good color thresholds (depending on the image) which lead the algorithm to give a good first guess of the tumour;

2. MD have always a better medical interpretation than an automatic algorithm, so this first contour can be modified manually with a "paint brush" like feature allowing to add or remove parts of the image in the tumour contour (see the "Edit" box on the right of Fig. 5.3);

People knowing the field could argue that this workflow is already done by other softs like e. g. Osirix. However 4. & 5. do not feed our specific needs in terms of volume computing and export of data. So that we needed a tool like SETIS.

3. Easy scrolling between the available slices (in the z direction) can be done to reiterate the tumour segmentation on the other slices.

4. When (or during this process) all the slices are segmented, automatic tools can compute the surface of the tumour in a slice, the volume of the 3D tumour obtained by aggregating all the segmented slices, make a 3D volume visualization of this 3D tumour for visual checking (see the "Export" box on the right of Fig. 5.3 and the two inserts with white background).

5. We have various export procedures of the results to pipe them in the subsequent parameters estimation algorithms (e. g. Monolix Software or our in house implementation of SAEM).

This can sound quite technical but this is the most versatile and ergonomic way we found to effectively treat the raw data on a daily basis, in interaction with Oncologists. We need this step to obtain data we can rely on for the parameter estimation procedure. Note that all the data are always checked by a MD in this study on LGG, namely François Ducray.
To date, we have around 60 patients segmented through the above workflow. This process is continuous due to progressive arrival of new patients. At the end of the segmentation process, we thus have two types of data (time series): (i) original MRI with all grey levels; (ii) corresponding masks of the tumor with 0 or 1 values (say black and white, by opposition to the whole spectra of grey levels) depending on the presence or not of the tumour on a given pixel.

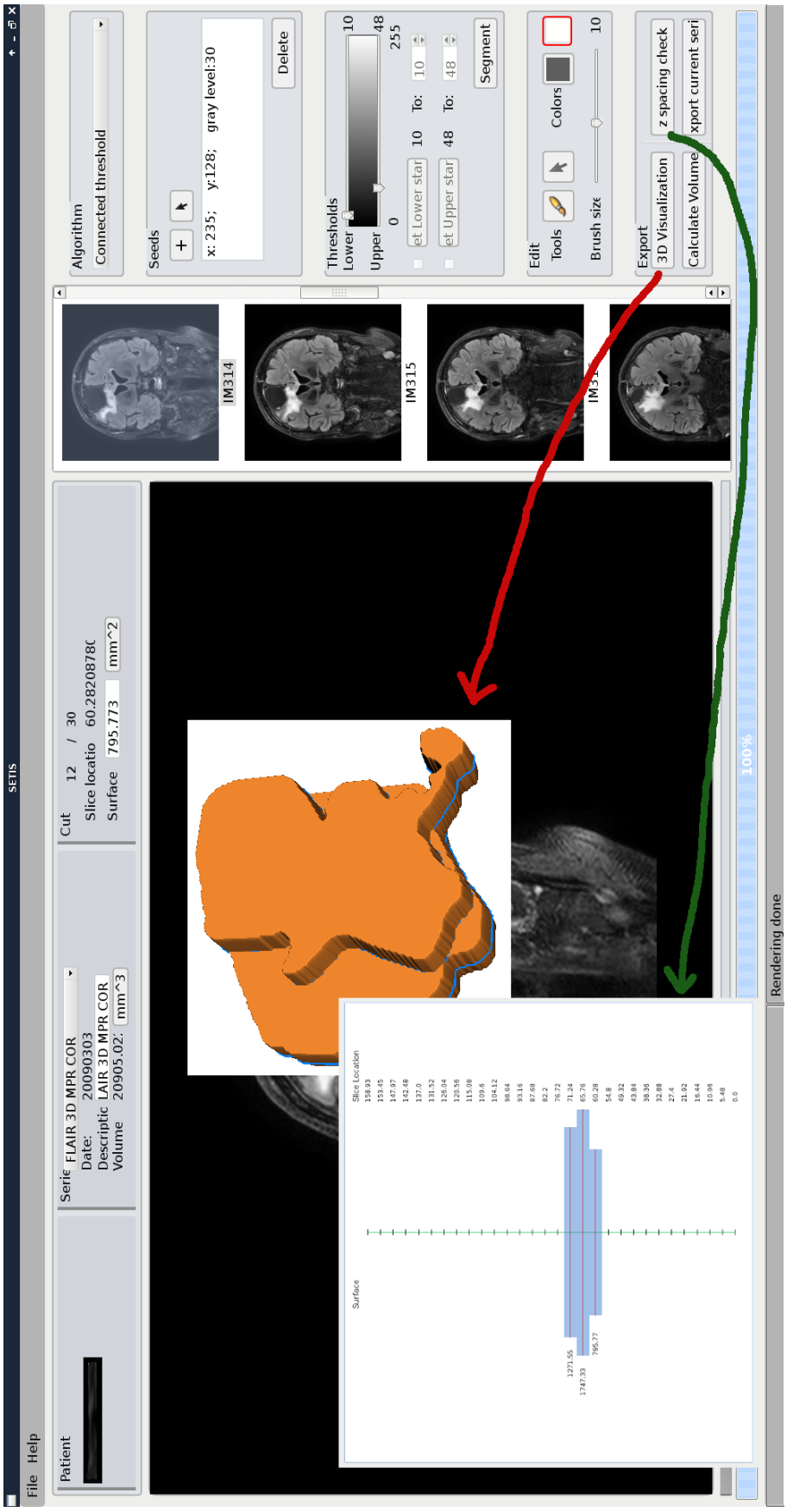

Figure 5.3: Setis Interface. Red arrow shows the output of the 3D rendering of the volume of the segmented tumour. Green arrow shows the visual "z-spacing" of the slices; this is needed due to versatility of the raw data format which can lead to wrong values for the z location of various slices.

Another aspect which needs to be treated in this kind of study is heterogeneity of the brain, for instance due to grey and white matter. Typically, when dealing with brain tumour evolution, the speed of propagation depends on the localization in the brain. A very common model in the literature of LGG is the aforementioned KPP model. This was pioneered by J.D. Murray and various collaborators through the groups of K.R. Swanson and P. Tracqui among others (see e.g. [Tra+95; Tra95], [SAMoo; Swa+03]). The brain heterogeneity leads to a dependence of the diffusion (D) and reaction (R) coefficients on the space variable. As a consequence, one needs to also treat the patient raw data to segment and mesh grey and white (G/W) matter. We also study the implementation of this point mixing various tools: ITK is used to segment G/W matter and we use e. g. FreeFem++ capabilities to mesh and solve resulting PDEs like KPP with space dependent coefficients (see Figure 5.4 for an illustration).

Figure 5.4: Grey and white matter segmentation and corresponding meshing (via FreeFem++), in view of a PDE resolution.

In works not yet published (but on which a significant amount of time was spent), in collaboration with the NUMED team members, we developed various models and methodologies to plug all these tools in a global chain of modelling and parameters estimation driven by medical imagery (one time series of a patient coming from the aforementioned population of ~60 LGG patients is shown on Figure 5.5). For instance, we aim at giving simple models which are able to describe spatially and temporally the growth of the tumour and then its decrease after treatment. The first phase is currently quite

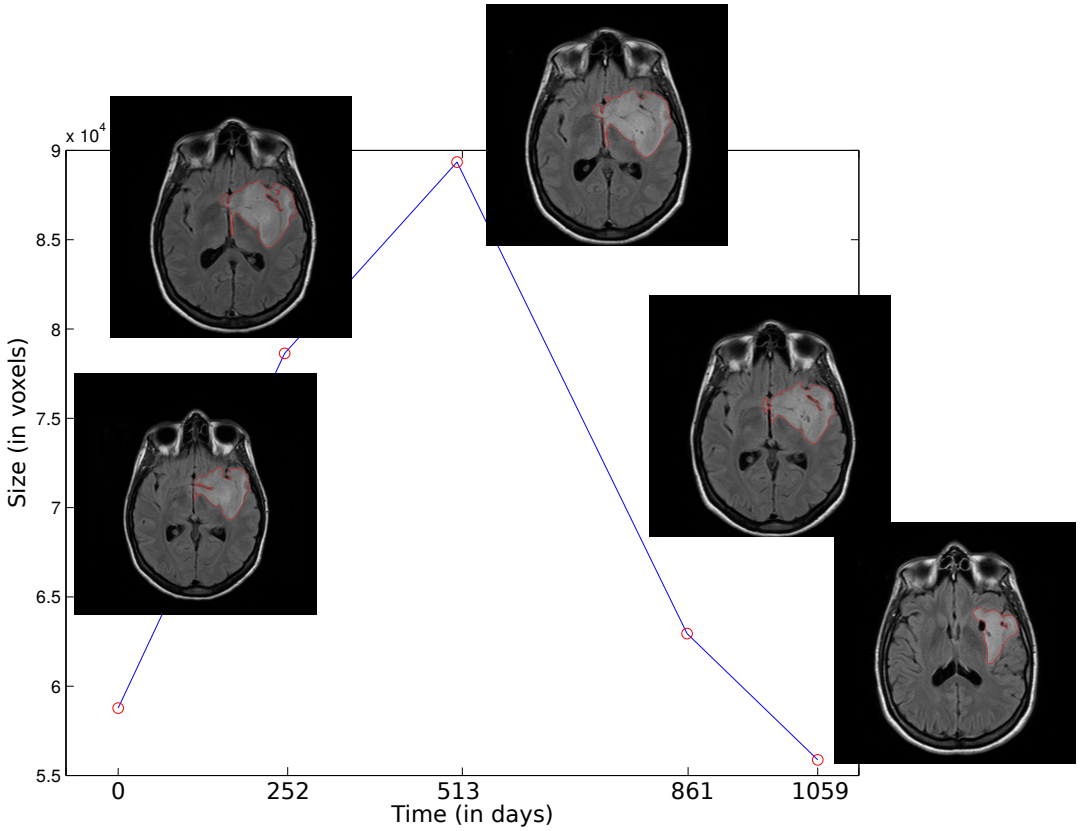

Figure 5.5: Tumor size (in voxels) along time of a Low Grade Glioma. The red contour in slices are the medically controlled segmented tumour. The decrease is due to a clinical treatment.

well handled while the decrease phase is (naturally) more involved. Note that among various tools, as a node in the direction of the PhD period, we are since recently using heavily Level Set approaches to tackle these problems.

Our mid and long terms goals are to perform progressively such tasks with SAEM and full 3D images. There are obviously several bottlenecks on this route, like the size of the raw data, the size of the mathematical inverse problem (done in high dimensional spaces and methods are thus needed to circumvent this difficulty). One of the interesting feature of such research program is that it does not apply only to tumor growth but also to many other fields where one uses PDE models driven by imagery.

BIBLIOGRAPHY

[Aca+12] C. Acary-Robert, E.D. Fernández-Nieto, G. Narbona-Reina, and P. Vigneaux. "A Well-balanced Finite Volume-Augmented Lagrangian Method for an Integrated Herschel-Bulkley Model." In: *Journal of Scientific Computing* 53.3 (2012), pp. 608–641 (cit. on pp. 4, 14, 21, 22, 25).

[Ame+01] P. Amestoy, I. Duff, J. L'Excellent, and J. Koster. "A Fully Asynchronous Multifrontal Solver Using Distributed Dynamic Scheduling." In: *SIAM Journal on Matrix Analysis and Applications* 23.1 (Jan. 2001), pp. 15–41 (cit. on p. 86).

[Ame+06] Patrick R. Amestoy, Abdou Guermouche, Jean-Yves L'Excellent, and Stéphane Pralet. "Hybrid scheduling for the parallel solution of linear systems." In: *Parallel Computing*. Parallel Matrix Algorithms and Applications (PMAA'04) 32.2 (Feb. 2006), pp. 136–156 (cit. on p. 86).

[Anc07] C. Ancey. "Plasticity and geophysical flows: A review." In: *Journal of Non-Newtonian Fluid Mechanics* 142 (2007), pp. 4–35 (cit. on pp. 14, 31, 93).

[AAE12] C. Ancey, N. Andreini, and G. Epely-Chauvin. "Viscoplastic dambreak waves: Review of simple computational approaches and comparison with experiments." In: *Advances in Water Resources* 48 (Nov. 2012), pp. 79–91 (cit. on p. 93).

[AC09] C. Ancey and S. Cochard. "The dam-break problem for Herschel-Bulkley viscoplastic fluids down steep flumes." In: *J. Non-Newtonian Fluid Mech.* 158.1-3 (2009), pp. 18–35 (cit. on p. 93).

[AB15] Christophe Ancey and Vincent Bain. "Dynamics of glide avalanches and snow gliding." In: *Reviews of Geophysics* 53.3 (Sept. 2015), pp. 745–784 (cit. on p. 31).

[AEA12] Nicolas Andreini, Gaël Epely-Chauvin, and Christophe Ancey. "Internal dynamics of Newtonian and viscoplastic fluid avalanches down a sloping bed." In: *Physics of Fluids (1994-present)* 24.5 (May 2012), p. 053101 (cit. on p. 93).

[AST09] Global Digital Elevation Model v2 ASTER. Tile N45E006 is used. ASTER GDEM is a product of METI and NASA. doi: 10.5067/ASTER/ASTGTM.002. 2009. DOI: 10.5067/ASTER/ASTGTM.002 (cit. on p. 74).

[Bal+00] N. J. Balmforth, A. S. Burbidge, R. V. Craster, J. Salzig, and A. Shen. "Visco-plastic models of isothermal lava domes." In: *Journal of Fluid Mechanics* 403 (2000), pp. 37–65 (cit. on p. 16).

[Bal+06] Neil J. Balmforth, Richard V. Craster, Alison C. Rust, and Roberto Sassi. "Viscoplastic flow over an inclined surface." In: *Journal of Non-Newtonian Fluid Mechanics* 139.1–2 (Nov. 2006), pp. 103–127 (cit. on p. 14).

[BK89] H. T. Banks and K. Kunisch. *Estimation techniques for distributed parameter systems*. Vol. 1. Systems & Control: Foundations & Applications. Boston, MA: Birkhäuser Boston Inc., 1989, pp. xiv+315 (cit. on p. 98).

[BBS16] Pierre Barbillon, Célia Barthélémy, and Adeline Samson. "Parameter estimation of complex mixed models based on meta-model approach." In: *Statistics and Computing* (June 2016), pp. 1–18 (cit. on pp. 99, 101, 102).

[BM81] A. Bermúdez and C. Moreno. "Duality methods for solving variational inequalities." In: *Computers & Mathematics with Applications* 7.1 (Jan. 1981), pp. 43–58 (cit. on pp. 13, 22).

[BV94] A. Bermúdez and M. E. Vázquez Cendón. "Upwind methods for hyperbolic conservation laws with source terms." In: *Comput. Fluids* 23.8 (1994), pp. 1049–1071 (cit. on p. 20).

[Bin16] E. C. Bingham. "An investigation of the laws of plastic flow." In: *Bulletin of the Bureau of Standards* 13 (1916), pp. 309–353 (cit. on pp. 9, 10).

[Bin22] E. C. Bingham. *Fluidity and plasticity*. Mc Graw-Hill, 1922 (cit. on p. 10).

[BDY83] R Byron Bird, GC Dai, and Barbara J Yarusso. "The rheology and flow of viscoplastic materials." In: *Reviews in Chemical Engineering* 1.1 (1983), pp. 1–70 (cit. on p. 10).

[Bou04] François Bouchut. *Nonlinear Stability of Finite Volume Methods for Hyperbolic Conservation Laws*. Springer, 2004. ISBN: 978-3-7643-6665-0 (cit. on p. 20).

[BB16] François Bouchut and Sébastien Boyaval. "Unified derivation of thin-layer reduced models for shallow free-surface gravity flows of viscous fluids." In: *European Journal of Mechanics - B/Fluids* 55, Part 1 (Jan. 2016), pp. 116–131 (cit. on p. 14).

[BW04] Francois Bouchut and Michael Westdickenberg. "Gravity driven shallow water models for arbitrary topography." In: *Communications in Mathematical Sciences* 2.3 (Sept. 2004), pp. 359–389 (cit. on p. 14).

[BMV16] M. Boutounet, J. Monnier, and J. -P. Vila. "Multi-regime shallow free surface laminar flow models for quasi-Newtonian fluids." In: *European Journal of Mechanics - B/Fluids* 55, Part 1 (Jan. 2016), pp. 182–206 (cit. on p. 14).

[Bre+10] D. Bresch, E. D. Fernandez-Nieto, I. R. Ionescu, and P. Vigneaux. "Augmented Lagrangian Method and Compressible Visco-plastic Flows: Applications to Shallow Dense Avalanches." In: *New Directions in Mathematical Fluid Mechanics*. Ed. by G. P. Galdi et al. Advances in Mathematical Fluid Mechanics. Birkhauser Basel, 2010, pp. 57–89. ISBN: 978-3-0346-0152-8 (cit. on pp. 4, 11, 14, 15, 20, 21, 32).

[BAE99] Gilmer R. Burgos, Andreas N. Alexandrou, and Vladimir Entov. "On the determination of yield surfaces in Herschel–Bulkley fluids." In: *Journal of Rheology (1978-present)* 43.3 (May 1999), pp. 463–483 (cit. on p. 12).

[CGP06] M. J. Castro, J. M. Gonzáles-Vida, and C. Parés. "Numerical treatment of wet/dry fronts in shallow flows with a modified Roe scheme." In: *Math. Mod. Meth. App. Sci.* 16.6 (2006), pp. 897–931 (cit. on p. 28).

[CG72] J. Cea and R. Glowinski. "Méthodes numériques pour l'écoulement laminaire d'un fluide rigide visco-plastique incompressible." In: *Int. J. Comput. Math., Sect. B* 3 (1972), pp. 225–255 (cit. on p. 40).

[Cha+07] T. Chacón, M. J. Castro, E. D. Fernández-Nieto, and C. Parés. "On well-balanced finite volume methods for non-conservative non-homogeneous hyperbolic systems." In: *SIAM J. Sci. Comput.* 29(3) (2007), pp. 1093–1126 (cit. on p. 24).

[Che+13] T. Chevalier, S. Rodts, X. Chateau, J. Boujlel, M. Maillard, and P. Coussot. "Boundary layer (shear-band) in frustrated viscoplastic flows." In: *EPL (Europhysics Letters)* 102.4 (2013), p. 48002 (cit. on pp. 83, 84, 86).

[CG16] A. Chiche and J.Ch. Gilbert. "How the augmented Lagrangian algorithm can deal with an infeasible convex quadratic optimization problem." In: *Journal of Convex Analysis* 23.2 (2016), pp. 425–459 (cit. on p. 22).

[Loc14] CLPA: Carte de Localisation des Phenomenes d'Avalanche. Tiles number AK68 and AJ67 are used. CLPA is a product of MEDAD, ONF and Cemagref (now IRSTEA). Publicly available at http://www.avalanches.fr/. 2007 - 2014 (cit. on pp. 74, 75).

[Cou16] P. Coussot. "Bingham's heritage." In: *Rheologica Acta* (Dec. 2016), pp. 1–14 (cit. on pp. 9, 10, 12).

[DGG07] E. J. Dean, R. Glowinski, and G. Guidoboni. "On the numerical simulation of Bingham visco-plastic flow: old and new results." In: *Journal of Non Newtonian Fluid Mechanics* 142 (2007), pp. 36–62 (cit. on p. 40).

[Del+06] F. Delbos, J. Ch. Gilbert, R. Glowinski, and D. Sinoquet. "Constrained optimization in seismic reflection tomography: a Gauss-Newton augmented Lagrangian approach." In: *Geophysical Journal International* 164.3 (2006), pp. 670–684 (cit. on p. 22).

[DLM99] B. Delyon, M. Lavielle, and E. Moulines. "Convergence of a stochastic approximation version of the EM algorithm." In: *Ann. Statist.* 27 (1999), pp. 94–128 (cit. on pp. 98, 105).

[DLR77] A. P. Dempster, N. M. Laird, and D. B. Rubin. "Maximum Likelihood from Incomplete Data via the EM Algorithm." In: *Journal of the Royal Statistical Society. Series B (Methodological)* 39.1 (1977), pp. 1–38 (cit. on p. 104).

[DFS10] Sophie Donnet, Jean-Louis Foulley, and Adeline Samson. "Bayesian Analysis of Growth Curves Using Mixed Models Defined by Stochastic Differential Equations." In: *Biometrics* 66.3 (Sep 2010), 733–741 (cit. on p. 98).

[DS08] Sophie Donnet and Adeline Samson. "Parametric inference for mixed models defined by stochastic differential equations." In: *ESAIM: Probability and Statistics* 12 (Jan. 2008), pp. 196–218 (cit. on p. 98).

[DAB11] Denys Dutykh, Céline Acary-Robert, and Didier Bresch. "Mathematical Modeling of Powder-Snow Avalanche Flows." In: *Studies in Applied Mathematics* 127.1 (2011), pp. 38–66 (cit. on p. 3).

[DL76] G. Duvaut and J.-L. Lions. *Inequalities in mechanics and physics*. Springer-Verlag, 1976, xvi, 397 p. : ISBN: 3540073272 (cit. on pp. 13, 33).

[Dys04] Freeman Dyson. "Turning points. A meeting with Enrico Fermi (quoting John von Neumann)." In: *Nature* 427 (Jan. 2004), p. 297 (cit. on p. 97).

[ET99] Ivar Ekeland and Roger Témam. *Convex analysis and variational problems*. Vol. 28. Classics in Applied Mathematics. Society for Industrial and Applied Mathematics (SIAM), 1999, pp. xiv+402 (cit. on p. 40).

[EHS05] Jocelyn Etienne, Emil J Hopfinger, and Pierre Saramito. "Numerical simulations of high density ratio lock-exchange flows." In: *Physics of Fluids* 17.3 (2005), p. 036601 (cit. on p. 3).

[FLS05] K.T. Fang, R. Li, and A; Sudjianto. *Design and Modeling for Computer Experiments (Computer Science & Data Analysis)*. Chapman & Hall/CRC, 2005 (cit. on p. 101).

[FGV14] Enrique D. Fernández-Nieto, José M. Gallardo, and Paul Vigneaux. "Efficient numerical schemes for viscoplastic avalanches. Part 1: The 1D case." In: *Journal of Computational Physics* 264 (May 2014), pp. 55–90 (cit. on pp. 4, 21–23, 29, 31, 32, 36, 38, 39, 41–43, 48–50, 66).

[FGV18] Enrique D. Fernández-Nieto, José M. Gallardo, and Paul Vigneaux. "Efficient numerical schemes for viscoplastic avalanches. Part 2: The 2D case." In: *Journal of Computational Physics* 353 (Jan. 2018). https://hal.archives-ouvertes.fr/hal-01593148, pp. 460–490. DOI: 10.1016/j.jcp.2017.09.054 (cit. on p. 31).

[FNV10] Enrique D. Fernández-Nieto, Pascal Noble, and Jean-Paul Vila. "Shallow Water equations for Non-Newtonian fluids." In: *Journal of Non-Newtonian Fluid Mechanics* 165.13–14 (July 2010), pp. 712–732 (cit. on pp. 14, 16).

[FV14] Enrique D. Fernandez-Nieto and Paul Vigneaux. "Some Remarks on Avalanches Modelling: An Introduction to Shallow Flows Models." In: *Advances in Numerical Simulation in Physics and Engineering - Lecture Notes of the XV 'Jacques-Louis Lions' Spanish-French School*. Ed. by Carlos Parés, Carlos Vazquez Cendon, and Frederic Coquel. SEMA SIMAI Springer Series. June 2014, pp. 51–106 (cit. on p. 4).

[FG83] M. Fortin and R. Glowinski. *Augmented Lagrangian methods: applications to the numerical solution of boundary-value problems*. North-Holland, 1983 (cit. on pp. 18–20, 37, 38, 86).

[FN05] I. A. Frigaard and C. Nouar. "On the usage of viscosity regularisation methods for visco-plastic fluid flow computation." In: *Journal of Non-Newtonian Fluid Mechanics* 127.1 (Apr. 2005), pp. 1–26 (cit. on p. 12).

[Gab+12] Pierre Gabriel, Shawn P. Garbett, Vito Quaranta, Darren R. Tyson, and Glenn F. Webb. "The contribution of age structure to cell population responses to targeted therapeutics." In: *Journal of Theoretical Biology* 311 (Oct. 2012), pp. 19–27 (cit. on p. 108).

[GPC05] José M. Gallardo, Carlos Parés, and Manuel Castro. "A generalized duality method for solving variational inequalities. Applications to some nonlinear Dirichlet problems." In: *Numer. Math.* 100.2 (2005), pp. 259–291 (cit. on p. 22).

[GP01] J.-F. Gerbeau and B. Perthame. "Derivation of viscous Saint-Venant system for laminar shallow water; numerical validation." In: *Discrete Contin. Dyn. Syst., Ser. B* 1.1 (2001), pp. 89–102 (cit. on p. 16).

[GP00] Michael B. Giles and Niles A. Pierce. "An Introduction to the Adjoint Approach to Design." In: *Flow, Turbulence and Combustion* 65.3-4 (2000), pp. 393–415 (cit. on p. 98).

[GLT76] R. Glowinski, J. L. Lions, and R. Trémolieres. *Analyse numérique des inéquations variationelles*. Dunod, Paris, 1976 (cit. on pp. 13, 18).

[GW11] R. Glowinski and A. Wachs. "On the Numerical Simulation of Viscoplastic Fluid Flow." In: *Numerical Methods for Non-Newtonian Fluids*. Ed. by R. Glowinski and J. Xu. Vol. 16. Handbook of Numerical Analysis. Elsevier, 2011, pp. 483–717 (cit. on pp. 13, 18, 84, 86).

[Gre+18] E. Grenier, C. Helbert, V. Louvet, A. Samson, and P. Vigneaux. "Population parametrization of costly black box models using iterations between SAEM algorithm and kriging." In: *Computational and Applied Mathematics* 37.1 (2018). Accepted March, 24, 2016, pp. 161–173. DOI: 10.1007/s40314-016-0337-5 (cit. on pp. 4, 99, 100, 102, 112).

[GLV14] Emmanuel Grenier, Violaine Louvet, and Paul Vigneaux. "Parameter estimation in non-linear mixed effects models with SAEM algorithm: extension from ODE to PDE." In: *ESAIM: Mathematical Modelling and Numerical Analysis* 48.5 (July 2014), pp. 1303–1329 (cit. on pp. 4, 99–102, 106, 108).

[HL11] Bernard Haasdonk and Boris Lohmann. "Special Issue on "Model Order Reduction of Parameterized Problems"." In: *Mathematical and Computer Modelling of Dynamical Systems* 17.4 (2011), pp. 295–296 (cit. on p. 101).

[HP32] K. Hohenemser and W. Prager. "Über die Ansätze der Mechanik isotroper Kontinua." In: *ZAMM - Journal of Applied Mathematics and Mechanics / Zeitschrift für Angewandte Mathematik und Mechanik* 12.4 (Jan. 1932), pp. 216–226 (cit. on p. 10).

[Ili40] A. A. Il'iushin. *Deformation of a viscous-plastic plastic body (in Russian)*. Uch. zap. MGU, Mekhanika, 1940, Vyp. 39 (cit. on p. 13).

[Ion13] Ioan R. Ionescu. "Viscoplastic shallow flow equations with topography." In: *Journal of Non-Newtonian Fluid Mechanics*. Viscoplastic Fluids: From Theory to Application 193 (Mar. 2013), pp. 116–128 (cit. on p. 14).

[IL16] Ioan R. Ionescu and Oana Lupaşcu. "Modeling shallow avalanche onset over complex basal topography." In: *Advances in Computational Mathematics* 42.1 (Feb. 2016), pp. 5–26 (cit. on p. 14).

[Isa06] Victor Isakov. *Inverse problems for partial differential equations*. Second. Vol. 127. Applied Mathematical Sciences. New York: Springer, 2006, pp. xiv+344 (cit. on p. 98).

[JFP06] Pierre Jop, Yoël Forterre, and Olivier Pouliquen. "A constitutive law for dense granular flows." In: *Nature* 441.7094 (June 2006), pp. 727–730 (cit. on p. 92).

[KS05] Jari Kaipio and Erkki Somersalo. *Statistical and computational inverse problems*. Vol. 160. Applied Mathematical Sciences. New York: Springer-Verlag, 2005, pp. xvi+339. ISBN: 0-387-22073-9 (cit. on p. 98).

[KS77] A. V. Kazhikhov and S. Smagulov. "The correctness of boundary value problems in a diffusion model in an inhomogeneous fluid." In: *Sov. Phys. Dokl* 22 (1977), pp. 249–250 (cit. on p. 3).

[Kho+13] Roman H. Khonsari et al. "A mathematical model for mechanotransduction at the early steps of suture formation." In: *Proceedings of the Royal Society of London. Series B* 280.1759 (May 2013), p. 20122670 (cit. on p. 4).

[KO88] N. Kikuchi and J. T. Oden. *Contact problems in elasticity: a study of variational inequalities and finite element methods*. Vol. 8. SIAM Studies in Applied Mathematics. Philadelphia, PA: Society for Industrial and Applied Mathematics (SIAM), 1988 (cit. on p. 42).

[KL05] E. Kuhn and M. Lavielle. "Maximum likelihood estimation in nonlinear mixed effects models." In: *Computational Statistics and Data Analysis* 49.4 (2005), pp. 1020–1038 (cit. on pp. 98, 101, 104, 105).

[LFM06] M. P. Landry, I. A. Frigaard, and D. M. Martinez. "Stability and instability of Taylor-Couette flows of a Bingham fluid." In: *Journal of Fluid Mechanics* 560 (July 2006), pp. 321–353. ISSN: 1469-7645 (cit. on p. 55).

[LV04] Jean-Claude Latché and D. Vola. "Analysis of the Brezzi-Pitkäranta Stabilized Galerkin Scheme for Creeping Flows of Bingham Fluids." In: *SIAM J. Numerical Analysis* 42.3 (2004), pp. 1208–1225 (cit. on pp. 55, 57).

[LM07] Marc Lavielle and France Mentré. "Estimation of Population Pharmacokinetic Parameters of Saquinavir in HIV Patients with the MONOLIX Software." In: *Journal of Pharmacokinetics and Pharmacodynamics* 34.2 (2007), pp. 229–249 (cit. on p. 98).

[LK10] O. Le Maitre and O. M. Knio. *Spectral Methods for Uncertainty Quantification With Applications to Computational Fluid Dynamics*. Springer, 2010. ISBN: 978-90-481-3519-6 (cit. on p. 113).

[Lio71] J.-L. Lions. *Optimal control of systems governed by partial differential equations.* Translated from the French by S. K. Mitter. New York: Springer-Verlag, 1971, pp. xi+396 (cit. on p. 98).

[Luc+09] I. Luca, K. Hutter, Y. C. Tai, and C. Y. Kuo. "A hierarchy of avalanche models on arbitrary topography." In: *Acta Mechanica* 205.1-4 (Apr. 2009), pp. 121–149 (cit. on p. 14).

[LPC15] Li-Hua Luu, Pierre Philippe, and Guillaume Chambon. "Experimental study of the solid-liquid interface in a yield-stress fluid flow upstream of a step." In: *Physical Review E* 91.1 (Jan. 2015), p. 013013 (cit. on pp. 83, 84, 86, 89, 90).

[MV17] Arthur Marly and Paul Vigneaux. "Augmented Lagrangian simulations study of yield-stress fluid flows in expansion-contraction and comparisons with physical experiments." In: *Journal of Non-Newtonian Fluid Mechanics* 239 (Jan. 2017), pp. 35–52 (cit. on pp. 4, 83, 84, 88, 89).

[MN09] Youssef M. Marzouk and Habib N. Najm. "Dimensionality reduction and polynomial chaos acceleration of Bayesian inference in inverse problems." In: *Journal of Computational Physics* 228.6 (Apr. 2009), pp. 1862–1902 (cit. on p. 101).

[MM65] P.P. Mosolov and V.P. Miasnikov. "Variational methods in the theory of the fluidity of a viscous-plastic medium (translated from PMM, Prikladnaya Matematika i Mekhanika)." In: *Journal of Applied Mathematics and Mechanics* 29.3 (1965), pp. 545–577 (cit. on p. 13).

[MO08] E. A. Muravleva and M. A. Olshanskii. "Two finite-difference schemes for calculation of Bingham fluid flows in a cavity." In: *Russian Journal of Numerical Analysis and Mathematical Modelling* 23.6 (2008), pp. 615–634 (cit. on p. 84).

[Mur15] Larisa Muravleva. "Uzawa-like methods for numerical modeling of unsteady viscoplastic Bingham medium flows." In: *Applied Numerical Mathematics*. International Conference Difference Schemes and Applications in Honor of the 90-th Birthday of Professor V. S. Ryaben'kii 93 (July 2015), pp. 140–149 (cit. on p. 84).

[Naa+10] Mohamed Naaim, Thierry Faug, Florence Naaim, and Nicolas Eckert. "Return period calculation and passive structure design at the Taconnaz avalanche path, France."

In: *Annals of Glaciology* 51.54 (May 2010), pp. 89–97 (cit. on p. 74).

[Nik+11] Kirill D. Nikitin, Maxim A. Olshanskii, Kirill M. Terekhov, and Yuri V. Vassilevski. "A numerical method for the simulation of free surface flows of viscoplastic fluid in 3D." In: *Journal of Computational Mathematics* 29.6 (2011), pp. 605–622 (cit. on p. 13).

[NV13] Pascal Noble and Jean-Paul Vila. "Thin power-law film flow down an inclined plane: consistent shallow-water models and stability under large-scale perturbations." In: *Journal of Fluid Mechanics* 735 (Nov. 2013), pp. 29–60 (cit. on p. 14).

[Old47] J. G. Oldroyd. "A rational formulation of the equations of plastic flow for a Bingham solid." In: *Mathematical Proceedings of the Cambridge Philosophical Society* 43.1 (1947), pp. 100–105 (cit. on p. 10).

[Osw09] P. Oswald. *Rheophysics. The deformation and flow of matter*. Cambridge University Press, 2009 (cit. on p. 2).

[PCM02] Carlos Parés, Manuel Castro, and Jorge Macías. "On the convergence of the Bermúdez-Moreno algorithm with constant parameters." In: *Numer. Math.* 92.1 (2002), pp. 113–128 (cit. on pp. 22, 60).

[PMC01] Carlos Parés, Jorge Macías, and Manuel Castro. "Duality methods with an automatic choice of parameters. Application to shallow water equations in conservative form." In: *Numer. Math.* 89.1 (2001), pp. 161–189 (cit. on p. 22).

[PR06] A.T. Patera and G. Rozza. *Reduced Basis Approximation and A Posteriori Error Estimation for Parametrized Partial Differential Equations*. MIT Monographs (also available online), 2006 (cit. on p. 101).

[PW60] L.E. Payne and H.F. Weinberger. "An optimal Poincaré inequality for convex domains." In: *Arch. Rat. Mech. Anal.* 5 (1960), pp. 286–292 (cit. on p. 42).

[Chr09] Photo of Christian from camp2camp.org. Ref: 1310221031-1513903585.jpg, license Creative Commons CC-by-sa. 2009 (cit. on p. 73).

[Pia79] Jean-Michel Piau. "Fluides non-newtoniens." In: *Editions Techniques de l'Ingenieur* [ref. article : A 710] (1979) (cit. on p. 55).

[Pra52] William Prager. *On slow visco-plastic flow*. Technical report 84. Providence, R.I.: Graduate Division of Applied Mathematics. Brown University., Dec. 1952 (cit. on p. 13).

[PFM09] A. Putz, I. A. Frigaard, and D. M. Martinez. "On the lubrication paradox and the use of regularisation methods for lubrication flows." In: *Journal of Non-Newtonian Fluid Mechanics* 163.1–3 (Nov. 2009), pp. 62–77 (cit. on pp. 13, 86, 87).

[RR27] Markus Reiner and Rassa Riwlin. "Die Theorie der Stroemung einer elastischen Fluessigkeit im Couette-Apparat." In: *Kolloid-Zeitschrift* 43 (Sept. 1927), pp. 1–5 (cit. on p. 55).

[RS03] Nicolas Roquet and Pierre Saramito. "An adaptive finite element method for Bingham fluid flows around a cylinder." In: *Computer Methods in Applied Mechanics and Engineering* 192.31–32 (Aug. 2003), pp. 3317–3341 (cit. on p. 84).

[Rou16] A. Roustaei. "Yield stress fluid flows in uneven geometries: applications to the oil and gas industry." PhD thesis. University of British Columbia (Vancouver), May 2016 (cit. on p. 87).

[RF13] A. Roustaei and I. A. Frigaard. "The occurrence of fouling layers in the flow of a yield stress fluid along a wavy-walled channel." In: *Journal of Non-Newtonian Fluid Mechanics* 198 (Aug. 2013), pp. 109–124 (cit. on pp. 84, 86).

[RGF15] A. Roustaei, A. Gosselin, and I. A. Frigaard. "Residual drilling mud during conditioning of uneven boreholes in primary cementing. Part 1: Rheology and geometry effects in non-inertial flows." In: *Journal of Non-Newtonian Fluid Mechanics*. Viscoplastic fluids: From theory to application 2013 220 (June 2015), pp. 87–98 (cit. on pp. 84, 86, 87).

[Sac+89] J. Sacks, S. B. Schiller, T. J. Mitchell, and H. P. Wynn. "Design and analysis of computer experiments." In: *Statistical Science* 4 (1989), pp. 409–435 (cit. on pp. 101, 108).

[SWN03] T. J. Santner, B. Williams, and W. Notz. *The Design and Analysis of Computer Experiments*. Springer-Verlag, 2003, p. 283 (cit. on pp. 101, 108, 110).

[Sar15] Pierre Saramito. *Efficient C++ finite element computing with Rheolef*. http://cel.archives-ouvertes.fr/cel-00573970. CNRS-CCSD ed., 2015 (cit. on p. 84).

[Sar16] Pierre Saramito. "A damped Newton algorithm for computing viscoplastic fluid flows." In: *Journal of Non-Newtonian Fluid Mechanics* 238 (Dec. 2016), pp. 6–15 (cit. on p. 92).

[SW17] Pierre Saramito and Anthony Wachs. "Progress in numerical simulation of yield stress fluid flows." In: *Rheologica Acta* (Jan. 2017), pp. 1–20 (cit. on pp. 13, 31, 42, 92).

[SVE08] W. H. A. Schilders, H. A. van der Vorst, and J. Rommes (Eds.) *Model Order Reduction: Theory, Research Aspects and Applications*. Springer Berlin Heidelberg, 2008 (cit. on p. 101).

[Sch89] Theodore Schwedoff. "Recherches expérimentales sur la cohésion des liquides. I. Rigidité des liquides." In: *J. Phys. Theor. Appl.* 8.1 (1889), pp. 341–359. DOI: 10.1051/jphystap:018890080034100 (cit. on p. 10).

[Sch90] Theodore Schwedoff. "Recherches expérimentales sur la cohésion des liquides. II. Viscosité des liquides." In: *J. Phys. Theor. Appl.* 9.1 (1890), pp. 34–46. DOI: 10.1051/jphystap:01890009003401 (cit. on p. 10).

[Sch00] Theodore Schwedoff. "La rigidité des liquides." In: *Rapports du Congrès International de Physique. Tome 1.* (1900), pp. 478–486 (cit. on p. 10).

[SW38] G.H. Shortley and R. Weller. "Numerical solution of Laplace's equation." In: *J. Appl. Phys.* 9 (1938), pp. 334–348 (cit. on p. 57).

[Sno+10] E. Snoeck, P. Chanu, M. Lavielle, P. Jacqmin, E. N. Jonsson, K. Jorga, T. Goggin, J. Grippo, N. L. Jumbe, and N. Frey. "A Comprehensive Hepatitis C Viral Kinetic Model Explaining Cure." In: *Clinical Pharmacology & Therapeutics* 87.6 (JUN 2010), 706–713 (cit. on p. 98).

[Sou+07] Paulo R. de Souza Mendes, Monica F. Naccache, Priscilla R. Varges, and Flavio H. Marchesini. "Flow of viscoplastic liquids through axisymmetric expansions–contractions." In: *Journal of Non-Newtonian Fluid Mechanics*. Viscoplastic fluids: From theory to application 142.1–3 (Mar. 2007), pp. 207–217 (cit. on p. 84).

[Stu10] A. M. Stuart. "Inverse problems: A Bayesian perspective." In: *Acta Numerica* 19 (May 2010), pp. 451–559 (cit. on p. 98).

[SAM00] K. R. Swanson, E. C. Alvord, and J. D. Murray. "A quantitative model for differential motility of gliomas in grey and white matter." In: *Cell Proliferation* 33.5 (2000), pp. 317–329 (cit. on p. 118).

[Swa+03] Kristin R. Swanson, Carly Bridge, J.D. Murray, and Ellsworth C. Jr Alvord. "Virtual and real brain tumors: using mathematical modeling to quantify glioma growth and invasion." In: *Journal of the Neurological Sciences* 216.1 (2003), pp. 1–10 (cit. on p. 118).

[Tar05] Albert Tarantola. *Inverse problem theory and methods for model parameter estimation*. Philadelphia, PA: Society for Industrial and Applied Mathematics (SIAM), 2005, pp. xii+342 (cit. on p. 98).

[Tra95] P. Tracqui. "From passive diffusion to active cellular migration in mathematical models of tumour invasion." In: *Acta Biotheoretica* 43.4 (1995), pp. 443–464 (cit. on p. 118).

[Tra+95] P. Tracqui, G. Cruywagen, D. Woodward, G. Bartoo, J. Murray, and E. Alvord. "A mathematical model of glioma growth: the effect of chemotherapy on spatio-temporal growth." In: *Cell Proliferation* 28.1 (1995), pp. 17–31 (cit. on p. 118).

[TMP16] Timm Treskatis, Miguel A. Moyers-González, and Chris J. Price. "An accelerated dual proximal gradient method for applications in viscoplasticity." In: *Journal of Non-Newtonian Fluid Mechanics* 238 (Dec. 2016), pp. 115–130 (cit. on pp. 42, 92).

[Vig+18] Paul Vigneaux, Guillaume Chambon, Arthur Marly, Li-Hua Luu, and Pierre Philippe. "Flow of a yield-stress fluid over a cavity: experimental and numerical investigation of a viscoplastic boundary layer." In: *Journal of Non-Newtonian Fluid Mechanics* 261 (Nov. 2018). https://hal.archives-ouvertes.fr/hal-01857303/, pp. 38–49. DOI: 10.1016/j.jnnfm.2018.08.005 (cit. on p. 93).

[VWA05] Guillaume Vinay, Anthony Wachs, and Jean-François Agassant. "Numerical simulation of non-isothermal viscoplastic waxy crude oil flows." In: *Journal of Non-Newtonian Fluid Mechanics* 128.2–3 (July 2005), pp. 144–162 (cit. on p. 84).

[VBL04] D. Vola, F. Babik, and J.-C. Latché. "On a numerical strategy to compute gravity currents of non-Newtonian fluids." In: *J. Comput. Phys.* 201.2 (2004), pp. 397–420. ISSN: 0021-9991 (cit. on p. 57).

[WT90] G. Wei and MA Tanner. "A Monte Carlo implementation of the EM algorithm and the poor man's data augmentation algorithms." In: *Journal of the American Statistical Association* 85 (1990), pp. 699–704 (cit. on p. 105).

[YA16] S. Yavari-Ramshe and B. Ataie-Ashtiani. "Numerical modeling of subaerial and submarine landslide-generated tsunami waves—recent advances and future challenges." In: *Landslides* 13.6 (Dec. 2016), pp. 1325–1368 (cit. on p. 31).

[YM15] Gangjoon Yoon and Chohong Min. "Analyses on the finite difference method by Gibou et al. for Poisson equation." In: *Journal of Computational Physics* 280 (2015), pp. 184–194 (cit. on p. 57).

ABSTRACT

This memoire, based on the works done at the ENS de Lyon (2008-2017), is made of two parts.

The first one is concerned by several aspects of the numerical simulation of viscoplastic fluids, thanks to duality methods (augmented Lagrangian and Bermúdez-Moreno). On the one hand, works on the design of well - balanced finite volume numerical schemes for prototypes of Shallow Water Bingham models (i.e. integrated in the vertical direction) are described. The 1D case is summarized while the 2D framework, which constitutes an original contribution of this document, is given in more details. In particular, we finish by an illustration of a viscoplastic avalanche in the Taconnaz avalanche path (Chamonix, Mont-Blanc). On the other hand, we give a synthesis on the work on the full 2D incompressible Bingham equations (i.e. not integrated like in the previous case) and its comparison with physical experiments in an expansion-contraction geometry.

In the second part, we give an overview of the work done within the INRIA Numed Team, concerning the development of Bayesian methods for the parameters estimation of PDEs based models. More precisely, this work is based on SAEM methods which are intensively used in Medicine and Biology. The computational cost, associated to the numerous evaluations of the PDE model, being prohibitive, we proposed: (i) the implementation of a fixed metamodel (computed offline), based on an autorefined (structured tree) interpolation grid. And (ii) a kriged metamodel which is refined online during the SAEM iterations.

RÉSUMÉ

Ce mémoire, basé sur l'activité réalisée à l'ENS de Lyon, est structuré en deux parties.

Dans la première, nous traitons de divers aspects de la simulation numérique de fluides viscoplastiques, grâce à des méthodes de dualité (Lagrangien Augmenté et Bermúdez-Moreno). D'une part, les travaux sur le développement de schémas numériques volumes-finis "bien équilibrés" pour des équations de type Saint-Venant Bingham (intégration sur la verticale) sont décrits. Le cas 1D est synthétisé alors que le cadre bidimensionnel, qui constitue une contribution originale de ce document, est présenté plus en détails. En particulier, nous finissons par une illustration d'avalanche viscoplastique dans le couloir de Taconnaz (Massif du Mont-Blanc). D'autre part, nous donnons un résumé du travail de simulation sur les équations de Bingham incompressible 2D complètes (i.e. non intégrées, par opposition au cas précédent) et la comparaison avec des expériences physiques dans une géométrie de type expansion-contraction.

Dans la seconde partie, nous donnons un survol des activités réalisées au sein de l'équipe INRIA Numed, concernant le développement de méthodes bayesiennes pour l'estimation de paramètres de modèles à base d'EDP. Plus précisément, ce travail concerne les méthodes SAEM qui sont très utilisées dans le domaine biomédical. Etant donné le coût prohibitif associé aux nombreuses évaluations du modèle EDP, nous avons proposé, d'une part, une implémentation de métamodèle fixe à base de grille d'interpolation autoraffinée (de type structuré arborescent) et, d'autre part, une méthode de métamodèle évolutif (construit par krigeage) se raffinant au cours des itérations du SAEM, elles mêmes.